A superfluid liquid helium target for electron scattering experiments at the S-DALINAC

Hilcker, Michaela

(2020)

TECHNISCHE UNIVERSITÄT DARMSTADT

A superfluid liquid helium target for electron scattering experiments at the S-DALINAC

vom Fachbereich Physik
der Technischen Universität Darmstadt

zur Erlangung des Grades
eines Doktors der Naturwissenschaften (Dr. rer. nat.)

Dissertation
von Michaela Hilcker, M.Sc.

Erstgutachter: Prof. Dr.Dr.h.c.mult. Norbert Pietralla
Zweitgutachter: Prof. Dr. Joachim Enders

Darmstadt 2020
D17

Hilcker, Michaela:
A superfluid liquid helium target for electron scattering experiments at the S-DALINAC
Darmstadt, Technische Universität Darmstadt
Jahr der Veröffentlichung der Dissertation auf TUprints: 2020
Tag der mündlichen Prüfung: 24.06.2020

Erklärung gemäß §9 Promotionsordnung

Hiermit versichere ich, dass ich die vorliegende Dissertation selbstständig angefertigt und keine anderen als die angegebenen Quellen und Hilfsmittel verwendet habe. Alle wörtlichen und paraphrasierten Zitate wurden angemessen kenntlich gemacht. Die Arbeit hat bisher noch nicht zu Prüfungszwecken gedient.

_____

Datum und Unterschrift

Abstract

The aim of this work was to develop a superfluid helium target for electron scattering experiments at the S-DALINAC. The target consists of a multistage helium cryostat including target cell and corresponding scattering chamber. It is initially filled with liquid helium at boiling temperature and then cooled down to 1.8 K via vapor pressure reduction. The infrastructure of the QCLAM spectrometer provides a set of basic conditions for the design. Difficulties in handling liquid helium provide further challenges.

After the delivery of the required components, the cryostat had to be assembled and tested. The development of a suitable cooling procedure was a particularly critical point. The functionality of the cryostat was demonstrated in a following experiment. The assumed advantages of superfluid helium instead of liquid helium at boiling temperature as target material were confirmed. A commissioning experiment at the QCLAM spectrometer was performed. By evaluating the spectrum of elastically scattered electrons, the target thickness could be measured experimentally. It agrees with the geometric manufacturer's specifications.

During the experiment, the focusing of the electron beam on the target was difficult. Therefore, simulations on a modified target cell geometry with an increased target area were performed.

Zusammenfassung

Ziel dieser Arbeit war die Entwicklung eines suprafluiden Heliumtargets für Elektronenstreuexperimente am S-DALINAC. Das Target besteht aus einem Heliumkryostat mit Targetkapsel und passender Streukammer. Es wird mit flüssigem Helium bei Siedetemperatur gefüllt und anschließend durch Dampfdruckreduzierung auf 1.8 K heruntergekühlt. Die Infrastruktur des verwendeten QCLAM Spektrometers liefert Rahmenbedingungen für das Design. Schwierigkeiten im Umgang mit flüssigem Helium bilden eine weitere Herausforderung.

Nach der Lieferung der Bauteile musste der Kryostat zusammengebaut und getestet werden. Die Entwicklung einer geeigneten Abkühlprozedur hat sich dabei als besonders kritischer Punkt herausgestellt. In einem anschließenden Experiment konnte die Funktionalität des Kryostaten gezeigt werden. Außerdem wurden vermutete Vorteile von suprafluidem Helium anstelle von flüssigem Helium bei Siedetemperatur als Targetmaterial bestätigt. Dazu wurde ein Kommissionierungsexperiment am QCLAM Spektrometer durchgeführt. Aus der Auswertung des Spektrums der elastisch am Helium gestreuten Elektronen konnte die Targetdicke experimentell gemessen werden. Sie stimmt mit den geometrischen Herstellerangaben überein.

Während des Experiments erwies sich die Fokussierung des Elektronenstrahls auf dem Target als problematisch. Daher wurden Simulationen zu einer veränderten Targetzellengeometrie mit vergrößerter Trefferfläche durchgeführt.

Content

1. Motivation

Because the electromagnetic interaction is very well understood, electromagnetic observables of atomic nuclei such as electron scattering form factors are of special interest to test the predictive power of nuclear models [1]. At the Institute of Nuclear Physics at the Technische Universität Darmstadt [2], investigations of the nuclear structure at low-momentum transfers are performed by means of high-resolution inelastic electron scattering.

Origin of the force that binds the atomic nucleus together is the strong interaction. Quarks and gluons interact with each other to form the protons and neutrons that build up the atomic nuclei. Beyond the binding of the nucleons, the strong interaction results in a residual interaction, similar to the Van-der-Waals force, which is responsible for the formation and structure of the nucleus. One goal of nuclear physics is the better understanding of this resulting nuclear potential in order to draw conclusions about the static and dynamic properties of the nuclei. It is not yet possible to calculate the nuclear potential directly from the interaction of the quarks. Instead, different methods are used to generate the nuclear potential in different ways, so that experimental results are reproduced as well as possible.

The starting point for a dynamical description of a physical system is knowledge of the relevant degrees of freedom of the interaction. One first takes the simple assumption of a two-body interaction that can be described by a potential [3]. The nucleus is to be described in such a way that each nucleon is located in a potential field generated by the totality of the remaining nucleons. The force between two neutrons is the same as the force between two protons if the coulomb part is subtracted. The resulting potential can therefore be written for protons and neutrons together if an isospin dependence is included in the potential. For a system of two nucleons the wavefunction can be written as a product of a space function, a spin function, and a function for the isospin part. There are different approaches to model the required potentials. The most successful ones are a mainly phenomenological method, a model based on the exchange of virtual mesons and the chiral effective field theory method, which is based on a series expansion in the low-momentum range of the nucleus.

In the phenomenological method one uses an appropriate functional form for the potential with a sufficient number of parameters. The parameters are chosen so that the potential describes as closely as possible the experimental results. The general form of the interaction is limited by symmetry and invariance properties of the Hamiltonian operator. Most of the potential can be written as a local potential. But the inclusion of an additional tensor force is necessary to describe the $l = 2$ disturbance of the $l = 0$ ground state of the deuteron, since the central potential $V(r)$ conserves angular momentum and has l as a good quantum number. It is also common to include a spin-orbit interaction of the form $L \cdot S$ with the spin S and the angular momentum L which is also not completely local as it is linear in the momentum. Additional forces like three-body contributions can be included in a phenomenological way. The most advanced potentials available today are the Argonne-V18-potential [4] and the CD-Bonn-potential [5]. They are broadly employed in the construction of nucleon-nucleon forces and especially the interaction of complex nuclei, where the participation of individual nucleons becomes extremely difficult to describe [3]. Phenomenological potentials can often describe experimental results fairly well, but their construction is not particularly transparent in some parts. Furthermore, it is hardly possible to state realistic uncertainties of the theoretical calculation.

Another way to describe the nuclear force is to be found in analyzing the meson exchange process directly. The fundamental degrees of freedom of the strong interaction are, as described above, the quarks and gluons that make up color-neutral particles. Mesons are bound systems of two valence quarks. The basic idea of the meson exchange model is that the interaction between two nucleons is mediated by the exchange of massive mesons. Since the exchange particles are massive, the interaction has a short range. The simplest exchange potential is due to the exchange of just one pion which results in the Yukawa-potential [6] in analogy with the one-photon-exchange potential of electrostatics. But only the long-distance part of the potential can be explained in that way. To reproduce all relevant parts of the nuclear force, different kinds of mesons must be included in the final potential. The meson exchange model gets problems when it comes to the short-range behavior of the interaction. As soon as the density distributions of two nucleons strongly overlap, the underlying dynamics of quarks and gluons emerge, which cannot be described simply by the exchange of particles. Therefore, additional phenomenological terms are added to describe the short-range behavior of the interaction. They contain several parameters that are matched to experimental data. Furthermore, the selection of the considered set of mesons is based more on the number of required fit parameters and the necessary operator structure than on general principles [7].

A novel way to construct a nucleon-nucleon potential in a rather systematic and theoretically better-founded way is offered by the chiral effective field theory (chiral EFT). The starting point for the formulation is the identification of relevant scales, degrees of freedom and symmetries of the physical system [8]. For an effective description, pions and nucleons are identified as important degrees of freedom within the relevant momentum scale. With this, one obtains the most general Lagragian and the most general S-matrix. Physical results are then evaluated in a series development in powers of a low-momentum scale as it is indicated in Figure 1. This is an explicit approximation of the nuclear interaction for small momentum transfers. The difficulty of describing the short-range part of nuclear interaction accurately is not explicitly considered here, because it is of minor importance for the momentum scales that are relevant for the nuclear structure. The interactions themselves are point like. The corresponding coupling constants must be adapted to suitable data. Therefore, it is important to find matching observables which are sensitive to them. For the formulation of the higher orders the contributions by 3 body forces are crucial. The great advantage of this approach is that higher order terms, as well as contributions by three and four body forces can be included or neglected depending on the required accuracy and convergence behavior of the system. Furthermore, theoretical, and numerical uncertainties can be calculated and specified. This leads to a very systematic and clean approach to the nuclear force in the momentum range that is relevant for the nuclear structure. However, practical calculations are limited to relatively light nuclei and lowest orders of the series expansion, which are denoted as *LO, NLO,…* in Figure 1.

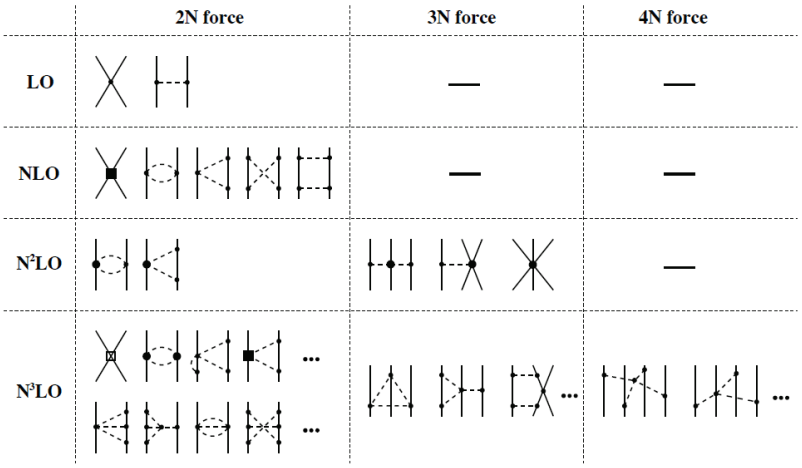

Figure 1: Contributions to the evolution of nuclear interaction from chiral EFT, grouped by particle number and order of the series expansion. Solid lines stand for nucleons, dashed lines for pions. LO stands for Leading Order, NLO for Next to leading Order. Slightly changed taken from [8].

For this reason, the experimental approach to measure observables of light nuclei at low-momentum transfers is of importance. The S-DALINAC is an ideal machine for this purpose. On these nuclei, predictions of the chiral EFT can be checked with great accuracy and specific aspects of the nuclear potential can be clearly identified. In fact, ^{4}He is an ideal benchmark nucleus to test different dynamical ingredients for the ab initio description of nuclei. While elastic form factors of ^{4}He have been extensively studied and typically the phenomenological approach (Standard Nuclear Physics Approach SNPA) and the more systematic chiral EFT lead to similar results, the situation is quite different for inelastic observables. A recent ab initio calculation of the monopole transition form factor of ^{4}He from the ground state to the first excited 0^+ state pointed to a large dependence of the results on the underlying interaction [9]. Three different Hamiltonians are used in the calculations. All of them describe the experimental ^{4}He ground-state energy within 1% and lead to the same elastic form factor but show large differences in their predictions for the monopole transition form factor $F_M^{tr}(q)$. In particular, at low-momentum transfers, where data were taken in Darmstadt in the 1960s [10], the discrepancies with respect to the chiral EFT prediction reaches a factor of about three. Since ^{4}He is a nucleus which should be particularly suitable for the execution of calculations within the framework of the chiral EFT, the question arises whether the measured deviations reflect a general problem of the theoretical method, or if there might be possible problems with the reliability of the experimental data. The chiral EFT method is based on a highly systematic and theoretically solid approach. In addition, the transparency with which possible measured values are extracted from the interaction is particularly high. If it should turn out that real measurements of already structurally simple nuclei such as ^{4}He differ strongly from the predictions of chiral EFT, this would indicate a major problem of the method. However, there are also well-founded considerations that call into question the correctness of the measured data.

A new measurement on the first excited 0^+ state of ^{4}He is needed to clarify the origin of the current problem and for concluding on the deviation of the most advanced ab initio calculations from the available data at low-momentum transfers. Figure 2 shows two examples. On the left-hand side, the electrical monopole transition form factor as a function of momentum transfer can be seen. It was calculated with three different models, plus the data points currently

available in the literature, which show discrepancies by a factor of 2 to 3. On the right-hand side, the theoretically calculated longitudinal response function as a function of the excitation energy, once with and once without the consideration of three-body forces, is shown. For the area shown, the effect of the inclusion of 3-body forces are particularly large, but experimental data are not yet available for this low-momentum transfer region. A corresponding experiment could therefore allow conclusions to be drawn about the appropriate implementation of 3-body forces in the nuclear potential. With the S-DALINAC it is possible to carry out measurements in precisely this low-momentum transfer area.

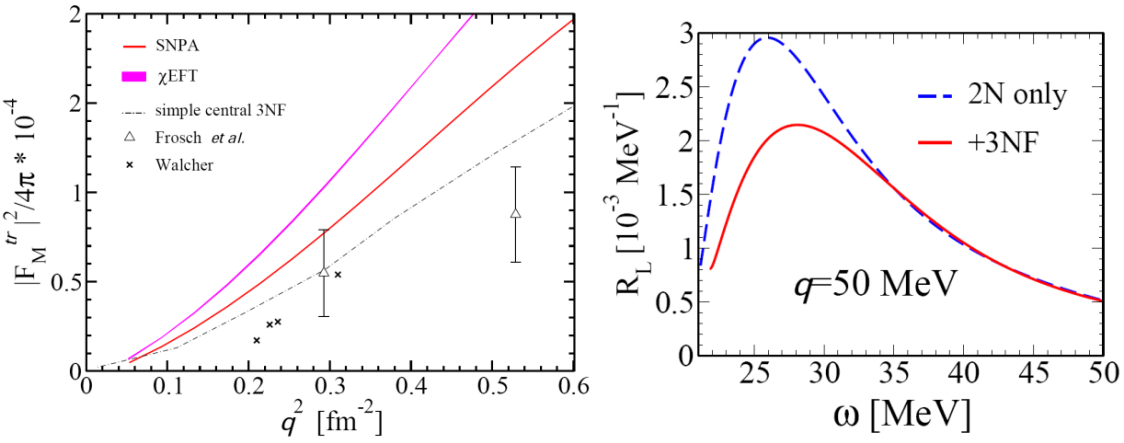

Figure 2: Left: Theoretically calculated electrical monopole transition form factor of the first excited state of ^{4}He as a function of momentum transfer for different nuclear potentials [9]. Right: Theoretical longitudinal response functions of ^{4}He as a function of excitation energy, once with and once without consideration of three-body forces [11].

For this reason, an electron scattering experiment at low-momentum transfer on a liquid helium target will be performed within the Collaborative Research Center 1245 "Nuclei: From Fundamental Interactions to Structure and Stars" [12]. Two different observables will be studied in detail. First, the width as well as the electrical monopole transition form factor of the first excited state. This is a 0^+ state at an excitation energy of 20.21 MeV. Second, the longitudinal response function $R_L(\omega)$ at excitation energies greater than 22 MeV.

In order to obtain sufficiently good statistics of the measured data in an acceptable measuring time while maintaining a good energy resolution, it is necessary to use sufficiently dense target material. Therefore, solid materials are usually preferred. However, since helium does not create any solid phase under vacuum conditions [13], other ways to achieve a large target thickness needs to be established. In the earlier experiments in Darmstadt normal-liquid helium was used as target material [14]. A possible problem may be that the fluctuating heat input into the boiling target might have led to bubble formation and an uncontrollable reduction of the effective target thickness. This would have resulted in too small scattering count rates, and hence in underestimated scattering cross sections and form factors.

Therefore, it was decided to accept the larger experimental effort of using a superfluid liquid target. The advantage of this approach is that the thermal conductivity of superfluid helium is almost infinitely large [15], avoiding the production of bubbles and corresponding changes of the effective target thickness.

This makes the construction of a suitable target setup, including a helium cryostat and a corresponding new scattering chamber inevitable. The handling of superfluid liquid helium is associated with certain difficulties due to the extremely low temperatures and its sometimes somewhat unusual behavior, which must be considered in the design.

2. Theoretical Background

The aim of this work is to construct and commission a superfluid helium target for electron scattering experiments. For this purpose, knowledge of low temperature physics must be combined with knowledge of electron scattering experiments. Therefore, in the first part of this chapter basic knowledge about electron scattering is summarized as far as it is relevant for the construction of the target system or the evaluation of the data obtained in the commissioning experiment. In the next part it will be considered how the used electron beam will deposit energy in the helium, since for the construction of a low-temperature cryostat the possible heat input is always of special importance. Subsequently, the properties of liquid helium are summarized, since the strange properties of helium provide further important basic conditions for the cryostat design.

2.1. Electron Scattering

Electron scattering experiments have been a frequently used instrument in modern nuclear structure research since Hofstadter's famous pioneering experiments at the Stanford linear accelerator [16]. Electron scattering has some practical advantages over other experimental techniques [17]. The interaction between the scattered electron and the nucleus under investigation is purely electromagnetic. The underlying Coulomb interaction and the related theory of quantum electrodynamics are among the best understood physical concepts so far. Inaccuracies in the data analysis, which are due to the lack of knowledge regarding the underlying interaction, are thus eliminated. In addition, the electromagnetic interaction is weak enough that the scattering processes can be treated in terms of perturbation theory, but large enough that necessary measurement times do not become excessively long.

In addition, electrons in the scattering process interact with the nucleus through the exchange of virtual photons. Compared to spectroscopy with real photons, this has two important advantages for the investigation of excited states. With the interaction by real photons all experiments are bound to the quantum mechanical selection rules for angular momentum states. These selection rules do not apply to virtual photons, so that for example 0^+ to 0^+ transitions can be considered, whereas they would be forbidden for real photons. Furthermore, electron scattering studies the excitation process instead of the decay. Thus, breakup experiments with excitation energies above the proton or neutron separation threshold are possible. Both advantages are especially essential for the measurement of the monopole transition form factor and the longitudinal response function of ^{4}He. An experiment in which the break-up reaction of the first excited 0^+ state is measured by detecting the decay products of the nucleus would be considerably more complex but at least imaginable. For the measurement of the longitudinal response function, on the other hand, such an experiment would hardly be possible due to the many possible decay channels.

Usually two cases in electron scattering are distinguished. Either the incident electron does not transfer any energy to the nucleus (except for the recoil energy), so that the investigated nucleus is in the ground state after the scattering process. This case is called elastic scattering. In the other case, additional energy is transferred from the electron to the nucleus, so that the nucleus is in an excited state after the scattering process. This case is called inelastic scattering.

This chapter is based on [1] and [17], but the notation is taken from [18,19].

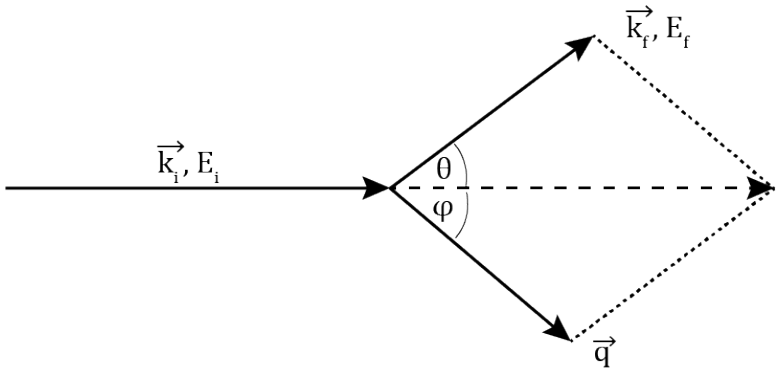

Figure 3: An electron with incident electron energy E_i and momentum $\vec{k_i}$ scatters on a nucleus with fixed position. Based on [17].

An electron with incident electron energy E_i and momentum $\vec{k_i}$ scatters on a nucleus with fixed position (Figure 3). After the scattering process it will have an energy E_f and a momentum $\vec{k_f}$ so the kinematic equations

$$\vec{k_\mathrm{i}} - \vec{k_\mathrm{f}} = \vec{q} \tag{2.1}$$

$$E_i - E_\mathrm{f} = E_\mathrm{x} + E_\mathrm{R} \tag{2.2}$$

are fulfilled, where E_x is the excitation energy of the nucleus and E_R is the recoil energy. For elastic electron scattering is $E_\mathrm{x} = 0$. The total value of the momentum transfer q in units of fm^{-1} can be written as

$$q = \frac{1}{\hbar c}\sqrt{\frac{4E_\mathrm{i}(E_\mathrm{i} - E_\mathrm{x})\sin^2\frac{\theta}{2} + E_\mathrm{x}^2}{1 + \frac{2E_\mathrm{i}}{Mc^2}\sin^2\frac{\theta}{2}}} \tag{2.3}$$

The final Energy of the outgoing Electron, which will be measured in the spectrometer, is

$$E_\mathrm{f} = \frac{E_\mathrm{i} - E_\mathrm{x}\left(1 + \frac{E_\mathrm{x}}{2Mc^2}\right)}{1 + \frac{2E_\mathrm{i}}{Mc^2}\sin^2\frac{\theta}{2}}. \tag{2.4}$$

The scattering behavior of relativistic spin-½ particles on a resting, point-like spin-0 particle is described by the Mott cross section formula [20]

$$\left(\frac{d\sigma}{d\Omega}\right)_\mathrm{Mott} = \left(\frac{Z^2\alpha^2}{4\,E_\mathrm{i}^2\sin^4\frac{\theta}{2}}\right)\cdot\left(1 - \beta^2\sin^2\frac{\theta}{2}\right) \tag{2.5}$$

with the atomic number Z, the fine structure constant α and the relativistic factor $\beta = v/c$. In accelerator-based electron scattering experiments β is usually almost equal to 1 so that (2.5) is reduced to

$$\left(\frac{d\sigma}{d\Omega}\right)_{\text{Mott}} = \left(\frac{Z^2\alpha^2}{4\,E_\text{i}^2\sin^4\frac{\theta}{2}}\right)\cdot\left(\cos^2\frac{\theta}{2}\right) \tag{2.6}$$

to a high degree of accuracy.

The measured cross sections $(d\sigma/d\Omega)_{\text{Exp}}$ show deviations from this theoretical prediction, which are caused by the fact that some of the assumptions leading to the Mott cross section, i.e. point-like nuclei, do not correspond to reality. A form factor $|F(q)|^2$ is defined which contains all information about the measured deviations which gives than insight into the nuclear structure

$$\left(\frac{d\sigma}{d\Omega}\right)_{\text{Exp}} = \left(\frac{d\sigma}{d\Omega}\right)_{\text{Mott}}\cdot\frac{1}{\eta}\cdot|F(q)|^2. \tag{2.7}$$

The recoil

$$\eta = 1 + \frac{2E_\text{i}}{M\sin^2\frac{\theta}{2}} \tag{2.8}$$

must be considered if the mass number of the target nucleus is small.

2.2. Energy loss of fast Electrons in Matter

During their passage through matter, all particles lose part of their kinetic energy. In the case of fast electrons, losses due to collisions with the atoms of the passing material on the one hand and, due to the low mass of the electrons, losses caused by bremsstrahlung on the other hand are most significant factors [21,22]

$$\left(\frac{dE}{dx}\right)_{\text{tot}} = \left(\frac{dE}{dx}\right)_{\text{rad}} + \left(\frac{dE}{dx}\right)_{\text{coll}}. \tag{2.9}$$

This chapter is based on [18,21,22].

The Bethe-Bloch formula (2.10) for electrons describes the energy loss per unit path length of the electrons caused by collisions as a function of the kinetic energy of the electrons. The kinetic energy τ is given in units of $m_\text{e}c^2$.

$$-\left(\frac{\text{d}E}{\text{d}x}\right)_{\text{coll}} = 2\pi N_A r_\text{e}^2 m_\text{e}c^2\rho\frac{Z}{A}\frac{1}{\beta^2}\left(\ln\left(\frac{\tau^2(\tau+2)}{2\left(\frac{I}{m_\text{e}c^2}\right)^2}\right) + F(\tau) - \delta - 2\frac{C}{Z}\right) \tag{2.10}$$

$$F(\tau) = 1 - \beta^2 + \frac{\frac{\tau^2}{8} - (2\tau+1)\ln 2}{(\tau+1)^2} \tag{2.11}$$

$$2\pi\,N_A\,r_\text{e}^2\,m_\text{e}c^2 = 0{,}1535\ \text{MeV}\frac{\text{cm}^2}{\text{g}} \tag{2.12}$$

$$\text{r}_\text{e} = 2{,}817\cdot10^{-13}\text{cm} = \frac{e^2}{4\pi\,\epsilon_0\,m_\text{e}c^2} \tag{2.13}$$

Here r_e is the classical electron radius, m_e the electron mass, N_A the Avogadro number, I the average excitation energy, Z the atomic number, A the atomic mass number and ρ the density of the absorber as well as $\beta = v/c$ the velocity of the electron. The last two terms δ and $2\,C/Z$ describe the density correction, as well as the shell correction, which depend on the absorber material.

For energies below some GeV, electrons and positrons are the only particles for which bremsstrahlung makes a non-negligible contribution to energy loss since the emission probability σ is inversely proportional to the square of the particle mass.

The energy loss due to bremsstrahlung depends on the one hand on the electric field of the incident particle and on the other hand on the strength of the shielding of the absorber material's nuclear field by the envelope electrons. Therefore, not only the kinetic energy of the incident electrons but also the atomic number of the absorber plays a major role in the calculation of the effective cross section. With the particle density N of the absorber, the energy loss per unit path length due to bremsstrahlung becomes

$$-\left(\frac{dE}{dx}\right)_{\text{rad}} = \frac{N\,E\,Z(Z+1)\,e^4}{137\,m_e^2 c^4}\left(4\ln\frac{2E}{m_e c^2} - \frac{4}{3}\right). \tag{2.14}$$

The ratio between the energy loss due to bremsstrahlung and the energy loss due to collisions is given approximately by

$$\frac{\left(\frac{dE}{dx}\right)_{\text{rad}}}{\left(\frac{dE}{dx}\right)_{\text{coll}}} \cong \frac{EZ}{700}. \tag{2.15}$$

The kinetic energy E in this case is expressed in units of MeV. For helium as absorber material and electrons with a kinetic energy of 80 MeV it is $E \cdot Z/700 \approx 0.2$.

2.3. General Properties of Liquid Helium

The noble gas helium exists in nature in two different stable isotopes, helium-3 and helium-4 [15,23], while the lighter ^{3}He is primarily produced as a waste product of nuclear reactors and hydrogen bombs by the decay of tritium. The proportion of ^{3}He in natural helium gas deposits is negligible.

The heavier and much more abundant ^{4}He is today mainly extracted from natural gas deposits [24], but is still relatively rare. The helium atom is spherical and symmetrical due to the closed s-electron shell [23] and thus represents a particularly simple many-particle system. It is also the smallest of all known atoms. This section is mainly based on [15].

2.3.1. Influence of the zero-point energy

A special property of helium is that it does not become solid under normal pressure conditions, even arbitrary close to absolute zero temperature. In most substances, the solidification temperature is calculated from an equilibrium of the attractive Van-der-Waals bond, which is created by fluctuating dipole-dipole interactions, and the repulsive thermal energy of the atoms. The attracting force sorts the individual atoms into a crystalline lattice structure, while the thermal motion of the particles disturbs and possibly cancels this order. In liquid helium, however, these two forces are both so small that another interaction, the zero-point energy,

which can normally be neglected, plays a role. In a first approximation, an atom can be considered as a harmonic oscillator. The ground state energy is given by the Schrödinger equation. Each atom of the liquid is assigned a small cage volume which is formed by the adjacent atoms. The ground state energy is then given by

$$E_0 = \frac{h^2}{8\,ma^2} \tag{2.16}$$

$$a = \left(\frac{V_\mathrm{m}}{N_A}\right)^{\frac{1}{3}} \tag{2.17}$$

whereby a is the radius of the sphere in which the atoms are confined, N_A is the Avogadro number, h is the Planck's constant, V_m the molar volume and m the mass of the helium atom [25]. The mass of a helium atom is very small, so the influence of the zero-point energy is particularly large.

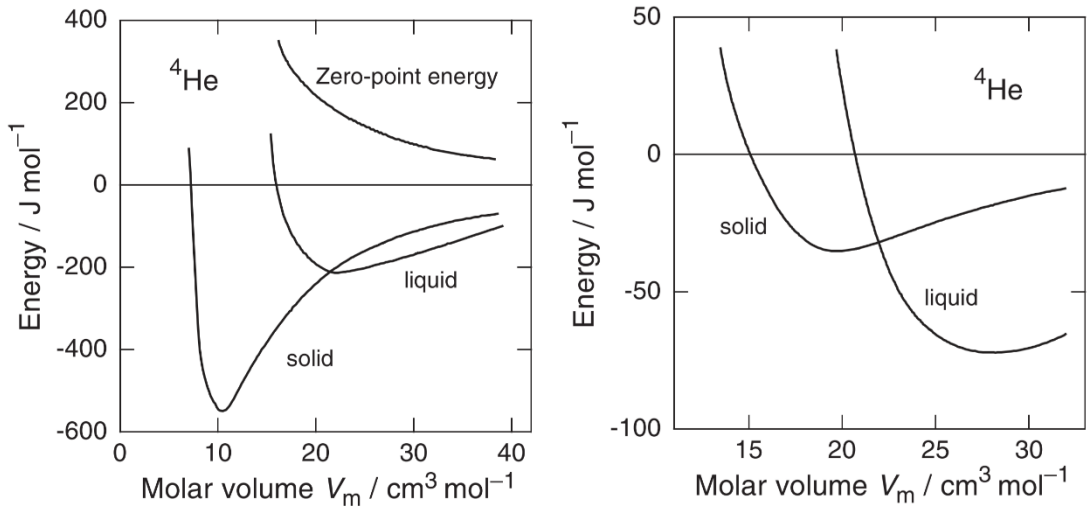

Figure 4: (Left) Representation of the potential energy of solid and liquid helium and the separated zero-point energy at $T = 0$ and normal pressure conditions,. (Right) Total energy of liquid and solid ^{4}He at $T = 0$ as a function of the molar volume. Taken from [15].

Figure 4 shows the influence of the zero-point energy on the formation of the aggregate phase along the vapor pressure curve at zero temperature. On the left-hand side, one can see that without the zero-point energy, which is positive across the entire range, the solid phase would be the energetically more favorable state. However, if the zero-point energy is added as shown on the right-hand side, the liquid phase is the energetically preferred one, so that no phase transition to the solid phase takes place. Furthermore, this behavior also ensures that helium has the lowest boiling point observed in nature, which makes helium the most important coolant in the field of low temperature physics. Helium-4 has a boiling temperature of 4.21 K. The density at the boiling point is 0.125 g/cm^3 and at the zero-temperature 0.145 g/cm^3.

2.3.2. Cooling by vapor pressure reduction

A method to cool the liquid helium below its boiling temperature is the usage of evaporation cryostats, which simply pumps the vapor above the liquid bath. The density dependence on temperature is given by the T_{90} definition of the temperature scale

$$T_{90}(p) = \sum_{i=0}^{9} A_i \left(\frac{\ln P - B}{C} \right)^i \tag{2.18}$$

with the Pressure P in Pascal, $B = 5.6$ and $C = 2.9$ [13]. The coefficients A_i are given in Table 1. In this way it is possible to reach temperatures down to roughly 1.3 K. Due to the logarithmic behavior of equation (2.18), it is necessary to pump more and more to achieve even lower temperatures, so that the extra effort becomes disproportionately large. A plot of equation (2.18) can be found in Figure 5.

Table 1: Coefficients A_i for ^{4}He given for equation (2.18).

A_0	A_1	A_2	A_3	A_4
1.392408	0.527153	0.166756	0.050988	0.026514
A_5	A_6	A_7	A_8	A_9
0.001975	-0.017976	0.005409	0.013259	0.0

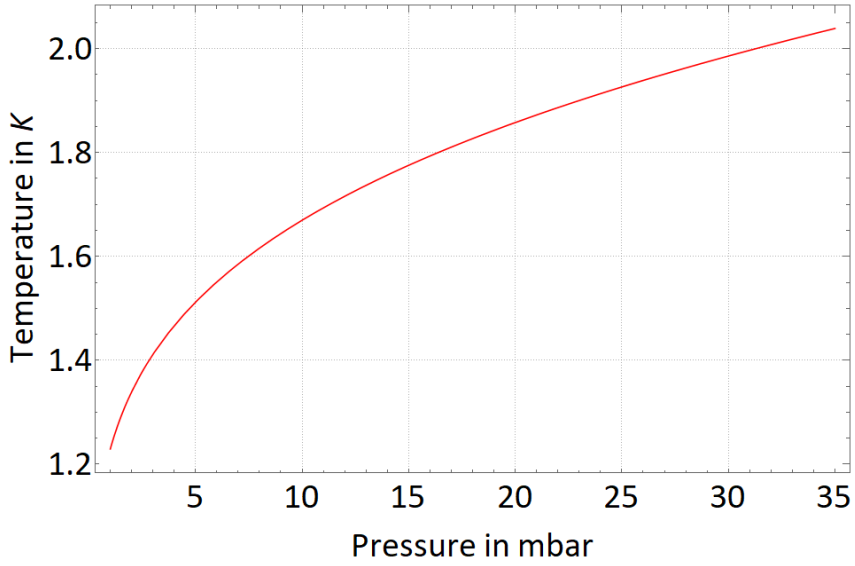

Figure 5: Dependence of temperature on vapor pressure according to equation (2.8). Temperatures down to 1.3 K can be reached efficiently with this method.

2.3.3. Specific heat and Lambda point

Another special characteristic of liquid helium is found in the temperature-dependent specific heat curve. Figure 6 shows the specific heat as a function of temperature in a range from 1 K to 3 K. A sharp maximum can be seen at a temperature of 2.17 K.

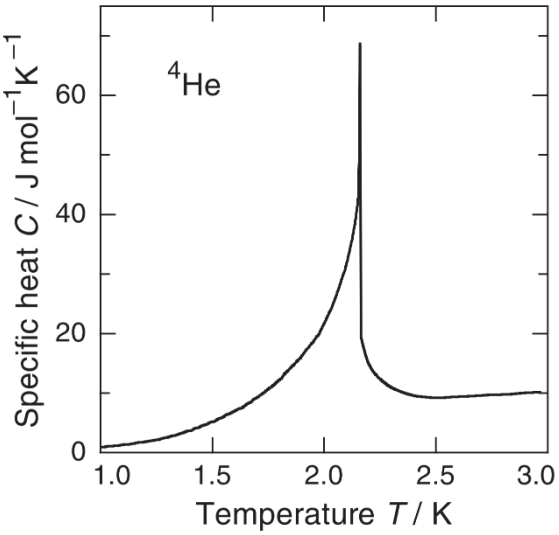

Figure 6: Specific heat of ^{4}He at the transition from the normal fluid to the superfluid phase as a function of temperature. Taken from [15].

Such a maximum in the specific heat usually indicates a phase transition where the incident heat is not used to change the temperature but to rearrange the structure within the substance. However, in this case it is not a transition between a solid and a liquid phase, but a transition between two different liquid phases. Therefore, the phase at higher temperatures is called helium-I and the phase at lower temperatures is called helium-II. Thanks to the characteristic shape of the curve, which is reminiscent of the Greek letter λ, this phase-transitional point is called the lambda point.

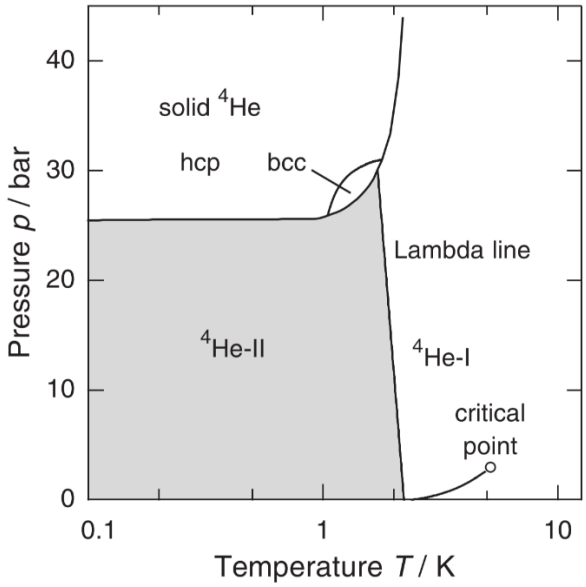

Figure 7: Pressure-temperature phase diagram of ^{4}He. Taken from [15].

The ^{4}He pressure-temperature phase diagram is shown in Figure 7. The lambda line describes the phase transition of the two liquid phases helium-I and helium-II. The temperature at which the transition occurs depends on the external pressure. At normal pressure the transition takes

place at a temperature of 2.17 K and shifts with increasing pressure to lower temperatures until it reaches the melting curve at 1.9 K [13]. At pressures above 25 bar, solid helium with different lattice structures can be produced. The boundary line between the solid and liquid phase also shows an abnormal minimum, which is, however, so weak that it cannot be seen in the figure. A triple point does not exist.

If a liquid is cooled below the boiling temperature, the density of the liquid depends on the temperature. Figure 8 shows the density dependence of liquid helium at vapor pressure as a function of temperature.

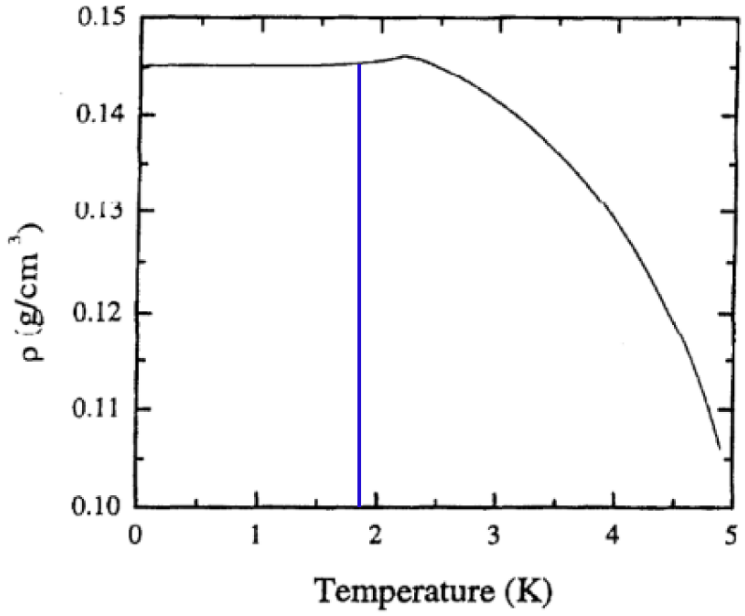

Figure 8: Density dependence of helium with the temperature at vapor pressure. Slightly modified taken from [13].

With decreasing temperature, the density increases strongly and forms a well visible maximum at 2.17 K. Then the density drops slightly and forms a plateau. Between 1.9 K and 1.3 K, the density fluctuates by only 0.2 % [13].

2.4. Properties of superfluid ^{4}He

At higher temperatures close to the boiling point, liquid helium behaves like a dense gas consisting of classical particles. At a temperature of 2.17 K, the lambda point, all kinds of properties of the liquid change abruptly [23]. This transition can be seen with the naked eye. Above the lambda point, the cold liquid is bubbling constantly, and visible boiling bubbles rise in the liquid. If the liquid gets cooled into the range of superfluidity, the entire liquid is suddenly completely still, and the liquid only evaporates from the surface [15].

Probably the most fundamental property of superfluid liquids is the ability to flow through the smallest capillary without friction. The viscosity of helium-II is several orders of magnitude smaller than that of helium-I. Furthermore, the flow velocity of the liquid is almost independent of the current pressure conditions. On the other hand, the measured viscosity depends strongly on the type of experiment with which it is measured. This at first sight somewhat strange behavior can be described by means of the two-liquid model.

It is assumed that the helium-II liquid is composed of a normal-fluid and an ideally superfluid component [15,25]. The total density ρ of the liquid is the sum of the two components ρ_n and ρ_s.

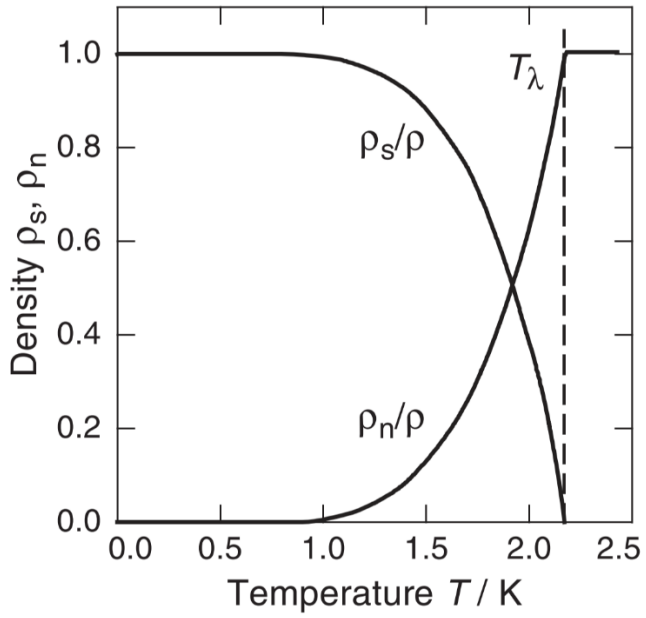

Figure 9: Density curve of the normal-fluid and the superfluid components in helium-II. Taken from [15].

The density fraction of the normal-fluid component is a function of the temperature. At absolute zero it is equal to zero and increases up to one when reaching the lambda point [13]. Figure 9 shows the progression of the proportions of both components. Of course, the assumption that helium-II is composed of two different components is only a model and does not imply that helium-II is actually a mixture of two different liquids. It is assumed that the superfluid component does not carry any entropy, does not experience viscous friction nor exhibit any turbulences.

With this two-fluid model it is for example possible to explain the differently measured viscosities depending on the experimental setup. If the viscosity of a liquid is measured via the flow through a thin capillary, the normal fluid component is largely blocked and only the superfluid component, which flows entirely without friction, moves through the capillary. The observed viscosity is therefore zero. Another possibility to measure the viscosity of liquids is the rotary viscometer. Here, a torque is measured on a stationary hollow cylinder, which is applied by an inner, rotating cylinder via the liquid in between. Since the superfluid component has no viscosity at all, it cannot contribute to the transmission of torque. Therefore, the total observed torque is transmitted by the viscosity of the normal fluid component. This viscosity does not become zero even at temperature zero. Instead, the viscosity is determined by the temperature-dependent free path length of the helium excitations. This results in a completely different curve of the viscosity of helium-II than that obtained by measuring with a capillary.

Another unusual property of superfluid helium is shown in so-called beaker experiments [15,25]. If an empty vessel is dipped into a bath of superfluid helium, helium flows into the beaker until the filling level in both vessels has equalized. Conversely, helium flows out of the immersed pot into the helium bath when the level in the beaker is above the level of the bath.

Figure 10 shows various beaker experiments. Due to the comparatively large Van-der-Waals force between the cup and the helium, a thin film is formed over the entire wall so that the levels can equalize.

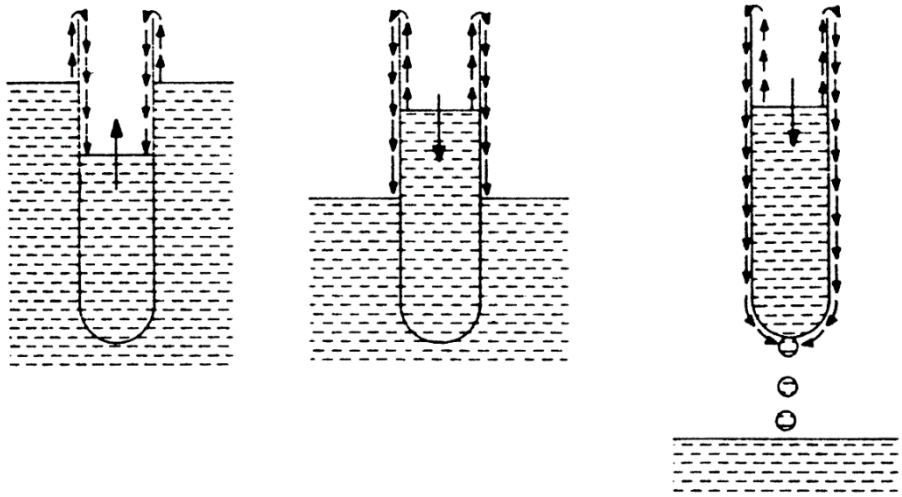

Figure 10: Representation of different beaker experiments. The superfluid helium crawls along the walls of the vessels until the level in both vessels is balanced. Taken from [25].

A for this work particularly important property of superfluid liquids is related to heat transport. The thermal conductivity of helium-II is about five orders of magnitude greater than that of helium-I [15]. This explains directly why visible boiling and the associated boiling bubbles disappear abruptly when the lambda point is undershot. The high thermal conductivity causes a homogeneous temperature distribution over the entire liquid, so that evaporation only occurs at the surface. This is the point where the temperature difference to the outside world is high.

3. Experimental Facility

The target system is to be used at the superconducting Darmstadt Linear Accelerator S-DALINAC at the Quadrupole Clamshell spectrometer QCLAM. A large part of the required infrastructure is therefore already in place and provides further basic constrains for the design of the required cryostat and the associated scattering chamber. Therefore, this chapter first introduces the accelerator and then the spectrometer, including the detector system, used for the experiments.

3.1. The Electron Accelerator S-DALINAC

The electron accelerator S-DALINAC (see Figure 11) is a superconducting continous wave linear accelerator [2]. The accelerator cavities are made of niobium and are kept at a temperature of 2 K using liquid helium. The electrons are pre-accelerated in the injector to 10 MeV and can be used already in the DHIPS setup for bremsstrahlung experiments [26]. Alternatively the pre-accelerated electrons can be fed into the main accelerator. Originally, the accelerator was designed and built with two recirculations. Recently, however, a third recirculation was added, which also allows the S-DALINAC to be operated as an energy-recovering linac [27]. When using the recirculation beam lines, the electrons can be guided back to the starting point of the main accelerator one or three more times via dipole magnets, allowing the accelerator cavities to be used to accelerate every electron up to 4 times. All in all, this allows the electrons to be accelerated to a maximum of 130 MeV.

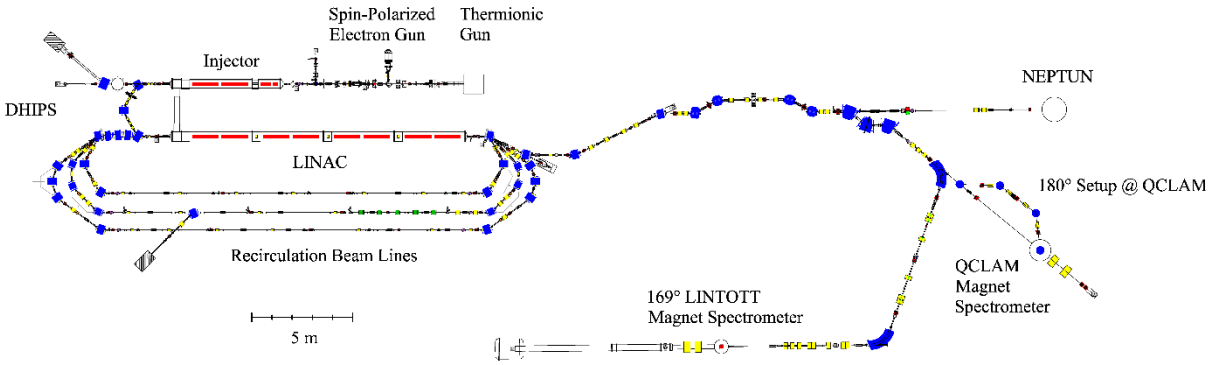

Figure 11: The accelerator S-DALINAC with beamline and experimental areas: Bremsstrahlung experiments at DHIPS, (γ, γ'x)-experiments at NEPTUN, QCLAM spectrometer with 180° chicane and 169° Lintott spectrometer

The accelerated electrons can then be guided to the experimental positions in the experimental hall. There are the photon tagger NEPTUN [28], the (e, e' x)-spectrometer QCLAM [2], which is described in more detail in chapter 3.2, and the high resolution (e, e')-spectrometer Lintott [2].

3.2. The QCLAM Spectrometer

To be able to measure the form factor (2.7) as described in chapter 2.1 and thus obtain information about the nuclear structure, the energy or momentum of the scattered electrons must be determined. However, a direct measurement is technically difficult. Therefore, the scattered electrons are instead sent through a magnetic field which is oriented perpendicular to the direction of flight of the electrons. Due to the Lorentz force, the electrons are directed on a circular path. The radius depends on the momentum of the scattered electron. The momentum information is thereby converted into a much easier to measure position information.

The QCLAM spectrometer [2,29] is one of the two large electron spectrometers at the S-DALINAC (Figure 12). The name stands for "quadrupole-clamshell spectrometer" since it has a focusing quadrupole at the beam entrance and a shell-like deflecting dipole magnet to bend the scattered electrons into the focal plane and the detector system. It has a large angular acceptance of 35 msr and a large momentum acceptance of ±10 %. At beam energies up to 200 MeV, scattering angles in the range of 19° to 161° can be detected with an energy resolution $\Delta E/E$ of $3 \cdot 10^{-4}$ [30,31]. With the help of a special chicane in the beam line it is also possible to perform measurements under a scattering angle of 180°. Due to the large acceptance ranges, the spectrometer is particularly suitable for the investigation of nuclear states where small count rates are expected.

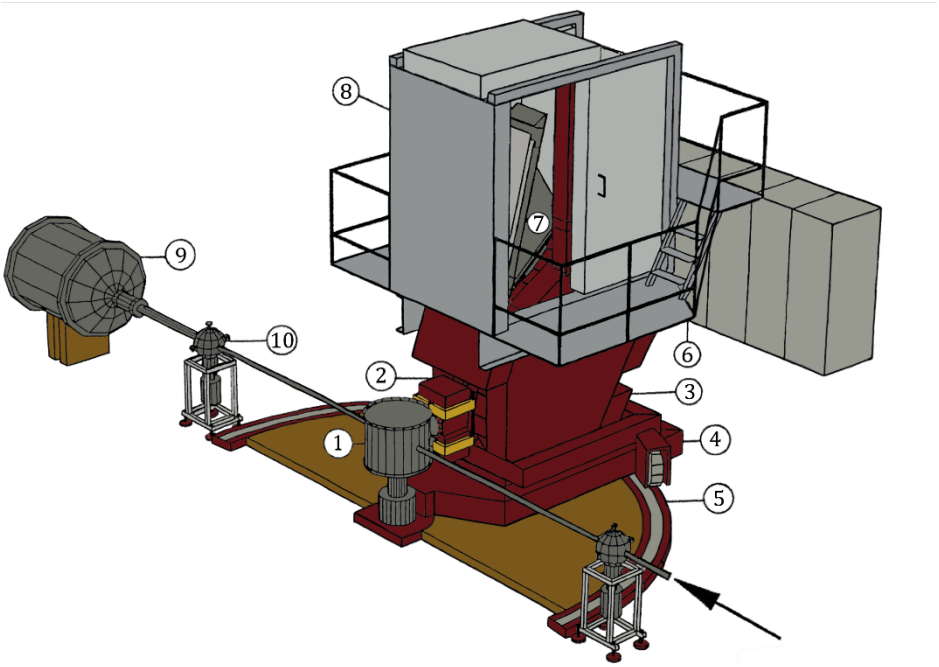

Figure 12: Experimental setup of the QCLAM spectrometer with beam line and beam dump. The arrow indicates the incoming electrons. ① Scattering chamber, ② Quadrupole magnet, ③ Dipole magnet, ④ Rotating and sliding frame, ⑤ Guide rail, ⑥ Working platform, ⑦ Detector system, ⑧ Lead shielding, ⑨ Beam dump, ⑩ Vacuum pumping station. Taken from [29] and slightly changed.

First the accelerated electrons enter the scattering chamber where they hit a target, usually a thin foil. Most of the electrons pass through the target without deflection and are stopped in the beam dump located behind the scattering chamber. This beam dump also provides the measurement of the beam current, which is needed for the data analysis. However, a small part of the electrons will interact with the atomic nuclei of the target, allowing these electrons to be scattered in all directions so that some of them enter the spectrometer (Figure 13). In order to cover the desired scattering angles, the spectrometer is mounted on a rotating bearing and can be turned around the scattering chamber.

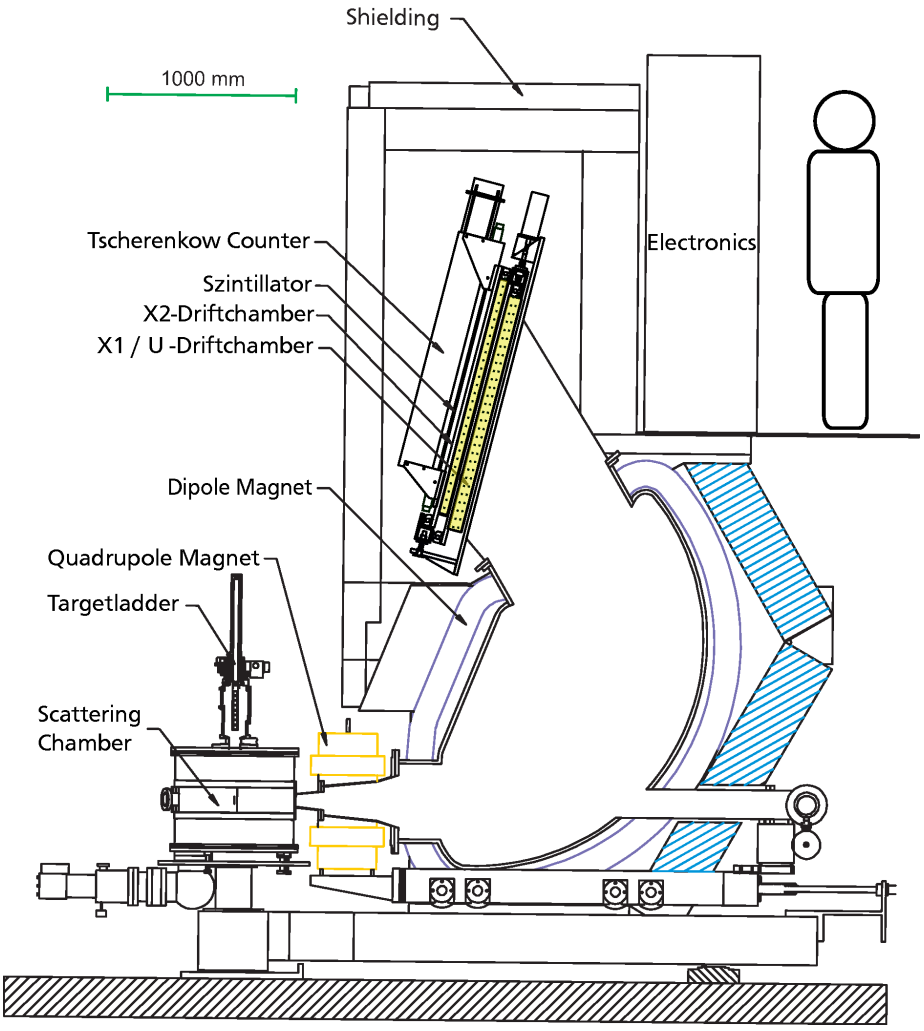

Figure 13: Schematic representation of the QCLAM spectrometer which consists of a scattering chamber, the magnet system with quadrupole and dipole magnet and the detector system. Taken from [32].

The magnet system consists of a focusing quadrupole and a momentum-selective bending dipole magnet [29]. The quadrupole magnet allows to focus the scattered electrons in horizontal direction. This focusing is required to achieve the large angular acceptance of the spectrometer without having to move the pole shoes of the dipole magnet too far apart. In addition, the quadrupole has an additional fifth neutral pole and which is used to correct imaging errors due to higher multipole components. The dipole magnet is used to generate the dispersion. The two pole shoes are inclined planarly by 2.54° with respect to the disperse plane. Together with the convex leading edge and the concave trailing edge of the pole shoes, a focusing of scattered electrons with the same energy is created in the focal plane. In addition, imaging errors are further reduced. A more extensive magnet system would have been necessary for a further reduction of higher order optical aberrations [30]. However, the large acceptance of the spectrometer leads to the fact that the focal plane of the spectrometer is curved and that the position-sensitive detector system cannot be put in the focal plane itself, anyway. Therefore, the detector must be designed in such a way that a recalculation of the full trajectories of the scattered electrons through the magnet system can be performed and thus the points of penetration through the focal plane can be reconstructed. In this way, imaging errors can be subsequently corrected within the framework of data analysis.

The detector system [32] of the QCLAM spectrometer consists of three vertical multi-wire drift chambers arranged one behind the other in the direction of the incoming electrons and a system of two trigger detectors, consisting of a Cherenkov counter and a scintillator. The scintillator is read out with two, the Cherenkov detector with one photomultiplier. A cross-section of the detector system is shown in Figure 14.

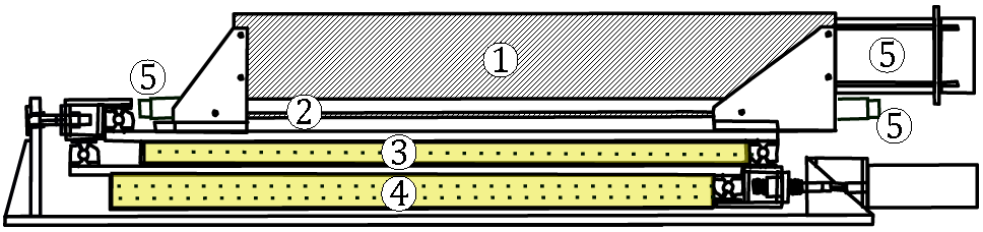

Figure 14: Drift chambers with support structure and trigger detectors. ① Cerenkov detector, ② Scintillator, ③ X2 wire plane, ④ U and X1 wire plane, ⑤ Photomultiplier. Slightly changed taken from [32].

The basic principle of multi-wire drift chambers is similar to that of a Geiger-Müller counter tube [21]. A drift chamber layer consists of a row of adjacent anode wires which are stretched between two cathode foils. A high voltage is applied to the two cathode foils so that an electric field is created between the cathode foils and the counting wires. In addition, the space enclosed by the foils is filled with a mixture of a counting gas and a quenching gas [32]. Originally, a mixture of argon and isobutane was used for this purpose, but was changed to a mixture of argon and CO_2 at some point in time [33].

If an electron enters the drift chamber, counting gas atoms are ionized and electron avalanches are generated along the path, analogous to the operation of a proportionality counter tube. The secondary electrons thus released are accelerated along the field lines towards the anode wires due to the high voltage applied, as shown in Figure 15. All the field lines that end in one anode wire are called drift cells. By measuring the drift times within the different drift cells the trajectory of the primary electron can be reconstructed.

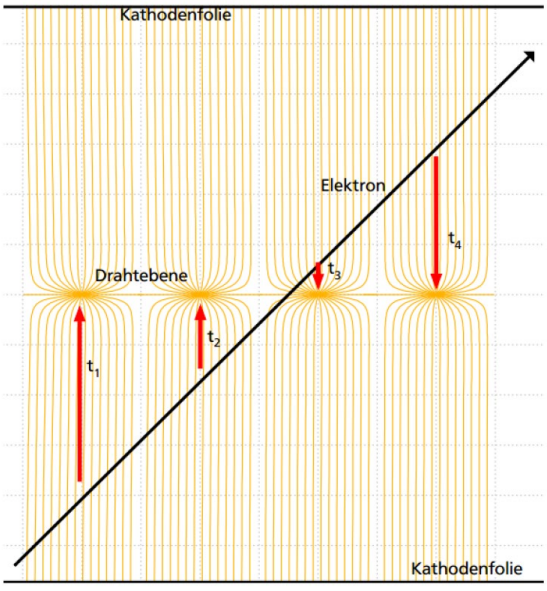

Figure 15: Schematic illustration of the electron trajectory through a drift chamber layer. On its way through the chamber the electron ionizes argon atoms. By measuring the drift times the path of the electron through the chamber can be reconstructed. Taken from [33].

Since the detector system is a three-dimensional object and since electrons can enter the chamber at different angles due to the large acceptance ranges of the spectrometer, a minimum of three wire planes, as shown in Figure 14, are required to determine all necessary quantities. The two planes X1 and X2 are used to measure the dispersive coordinate and the angle [32]. The third U-chamber measures the non-dispersive coordinate. In order to actually get additional information from the third chamber, the wires are rotated by 26.5° with respect to the wires of the other two chambers.

The more drift cells respond during a particle passage, the more accurate the measurement of the intersection points becomes. At the same time, the path length of the electrons in the detector must be as small as possible due to the small angle scattering within the chambers. As a compromise, the wire planes are set up with an angle of tilt of 44° relative to the reference beam.

For the actual measurement of the drift times in the individual chambers, an additional starting signal for the time measurement is required. The signal of the scintillator is used to do this. The scintillator is equipped with photomultipliers at both ends, so that the mean value of both signals will be used to determine the starting time. This eliminates differences in scintillator light propagation time caused by different striking points of the electrons. In addition, there is an extra Cherenkov detector, on which, however, a photomultiplier was installed on only one side. The time information of the Cherenkov detector is thus position-dependent and is not used for measuring drift times. Instead, this trigger detector is used for additional geometrical background suppression.

With this detector system the trajectory of the scattered electrons can be reconstructed. Thus, it is possible to reconstruct the curved focal plane of the spectrometer, to correct various imaging errors by software and, finally, to measure the energy of the scattered electrons with an angular resolution.

4. Design of the Target System

The aim of this work was to develop, build and test a superfluid helium target for electron scattering experiments at the QCLAM spectrometer (Section 3.1) for subproject A1 of the Collaborative Research Center 1245 [12]. For this purpose, the geometric requirements of the spectrometer and the existing beam line on the one hand, and difficulties in handling liquid helium on the other hand must be considered.

4.1. Requirements

It is planned to measure the width and form factor of the first excited state of ^{4}He, the 0^+ state at 20.21 MeV, with a precision of a few percent at the S-DALINAC by high-resolution inelastic electron scattering at low-momentum transfer using beam energies of 30-100 MeV and angular settings ranging from 69°-165°. The data will allow for a precise measurement of the monopole form factor at squared momentum transfers ranging from 1.0 fm^{-2} down to 0.03 fm^{-2}. To determine the longitudinal response function at excitation energies > 22 MeV, measurements with beam energies between 40 MeV and 60 MeV and scattering angles between 55° and 95° are planned [12,34].

For the new helium target, a dedicated scattering chamber needs to be developed which must be able to cover all these scattering angles. In addition, the electron beam should have a free path onto the target and into the spectrometer avoiding the passage of other material as much as possible. Due to the low temperatures required, however, it is essential to shield the outside temperature as comprehensively as possible with mounted heat shields. These two requirements are contradictory and must be balanced in the design of the cryostat according to the requirements.

Previous experiments have been conducted on normal fluid helium. It is possible that the boiling bubbles that occur in these experiments were underestimated. The resulting overestimation of the effective target density would lead to an underestimation of the resulting cross sections. In order to eliminate this problem in a new measurement, the newly developed target should be made of superfluid helium. The liquid, 4 K cryogenic helium can be ordered from the neighboring Institute of Solid-State Physics and collected in a helium Dewar. The target should therefore be filled with 4 K helium. It must then be cooled down to the desired temperature and transferred to a suitable target cell.

As shown in equation (2.18), the effort to achieve lower temperatures increases rapidly. The temperature should therefore be kept as close as possible to the Lambda point. On the other hand, the density dependence to the temperature decreases slightly below the lambda point. The goal is to stay well within the plateau range shown in Figure 8 even if the heat input to the target fluctuates to some extent, while keeping the effort and helium loss as low as possible. Therefore, the desired temperature is set to 1.8 K.

4.2. Design

For the design of the new target as well as the associated scattering chamber and the helium cryostat, two main criteria must be considered. First, the new system must fit into the environment of the QCLAM spectrometer. This entails a whole range of geometric conditions that must be fulfilled by the new design.

The second factor to consider is the heat input into the target. This results from the geometric configuration in the form of thermal radiation from the surrounding temperature on the one hand and from the additional heat input into the target by the electron beam on the other hand.

4.2.1. Geometrical Design

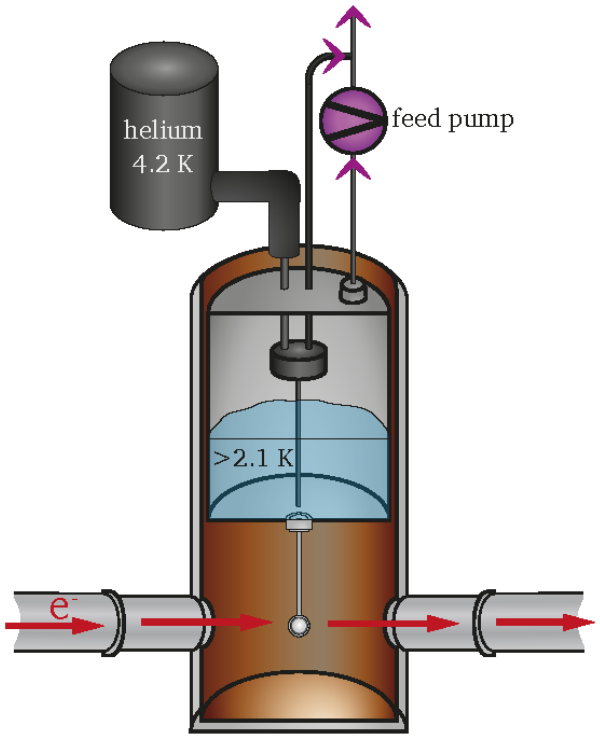

Figure 16: General target setup consisting of a scattering chamber, a target cell, superfluid helium reservoir with a feed pump and a 4.2 K helium tank that fills the superfluid reservoir. Heat shields prevent heat radiation from the outside.

Figure 16 shows one possibility of how a target that meets our needs could look like. The setup consists of a scattering chamber with coupling possibilities to the existing beamline, as well as the spectrometer itself. The electron beam comes from the accelerator from the left and hits the actual target in the middle of the scattering chamber. Most of the electrons are not scattered but exit the target on the other side. From there they go straight into the beam dump of the QCLAM spectrometer. The scattered electrons then are to be registered in the spectrometer. Therefore, there must be the possibility to flange the spectrometer to the scattering chamber for different scattering angles as it can be seen in Figure 12. The target itself consists of a thin-walled capsule filled with superfluid helium. The target capsule must be capable of being rotated, since the orientation relative to the beam axis must be changed depending on the scattering angle [18]. Due to the relatively large geometric extent of a liquid target, the correct alignment of the target, as it is shown in Figure 17, is particularly important in this case.

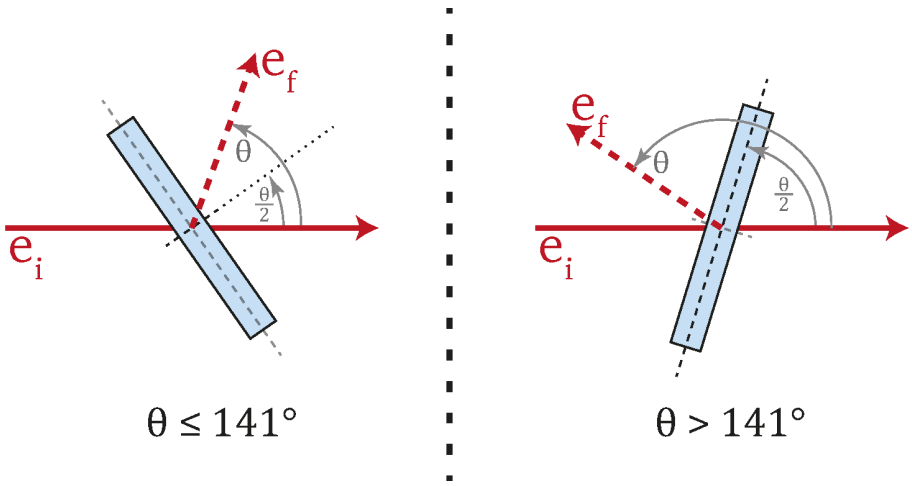

Figure 17: Positioning of the target depending on the scattering angle θ relative to the beam axis. Left for the transmission geometry (θ ≤ 141°), right for the reflection geometry (θ > 141°).

For the later experiment it is particularly important that the conditions in the target are identical all the time. The use of superfluid helium has decisive advantages over normal liquid helium, even if the technical effort involved is significantly higher:

First, the low viscosity. In the target cell, helium evaporates continuously through heat radiation from outside and through energy deposition by the electron beam (cf. Chapter 2.2). The evaporated helium must be replaced somehow with helium from a storage vessel. If the viscosity of the liquid would be too high, it is possible that the helium cannot follow up fast enough and thus a constant filling of the target cannot be guaranteed. In earlier experiments with cold liquid targets this has indeed caused problems [35].

A second advantage is the high thermal conductivity described in chapter 2.4. In order to calculate a cross section for a nuclear excitation, the areal mass density of the target must be known. In helium-I, boiling bubbles rise all the time, which reduce the effective mass coverage and make it uncertain. In helium-II these bubbles do not exist and therefore they cannot cause uncertainties.

In order to replace the helium evaporated in the target cell, a storage container with superfluid helium must be mounted above the target, which itself is filled from a storage tank with helium at boiling temperature. In order to cool the helium down below 2 K, the vapor pressure above the liquid helium is pumped out. Since the helium losses during cooling with this technique are quite large [15], it is advisable to bring only a small volume to the required temperature and to install an additional 4 K tank in the cryostat, from which the 2 K reservoir can be filled. If a finely adjustable needle valve is installed between the two tanks, the 2 K tank can also be filled continuously. A heat exchanging system should minimize the required cooling capacity and thus the helium consumption.

The entire system is in a vacuum environment, which provides thermal insulation of the helium tanks from the outside temperature on the one hand and undisturbed beam passage on the other hand. Heat shields made of copper or another material with good thermal conductivity shield the liquid helium from the outside temperature as much as possible in order to obtain the necessary low temperatures. For this purpose, it is also useful to install an additional tank which is filled with liquid nitrogen at boiling temperature. This tank is only thermally connected to the outermost layer of the heat shields, so that the heat shields connected to the liquid helium

can only see the boiling temperature of nitrogen instead of 300 K from outside. In order to further reduce heat input from the outside temperature, special super-insulation layers can be used, each consisting of many individual layers, which can be wrapped around the tanks. To keep thermal bridges as small as possible, all connections to the outside must be kept as small as possible. This means that the tanks are only connected to the outer scattering chamber at a few points. Unfortunately, this makes the cryostat less stable and it must be handled with care.

A particular problem of this special cryostat is the need for many (and for low-temperature applications large) necessary gaps in the heat shields. They are needed to allow the electron beam to reach the target and the beam dump unhindered and to allow the scattered electrons to enter the spectrometer undisturbed. At each of these locations, the thermal radiation from the ambient temperature hits the superfluid helium completely and heats it up accordingly.

One possibility to reduce this problem would be windows made of thin foils instead of real holes in the heat shields. If the spanned area is not too large, they work almost as well as the rest of the shield material. However, these foils would also cause a significant disturbance of the electron beam and are therefore undesirable.

Funnel-shaped heat shields could be an alternative. Figure 18 shows a schematic representation of such heat shields. The path of the electron beam is still completely open, but the heat radiation is stopped at least from a large solid angle range. However, in this case the focusing of the electron beam must be maintained over a longer distance instead of just on a single point at the target position.

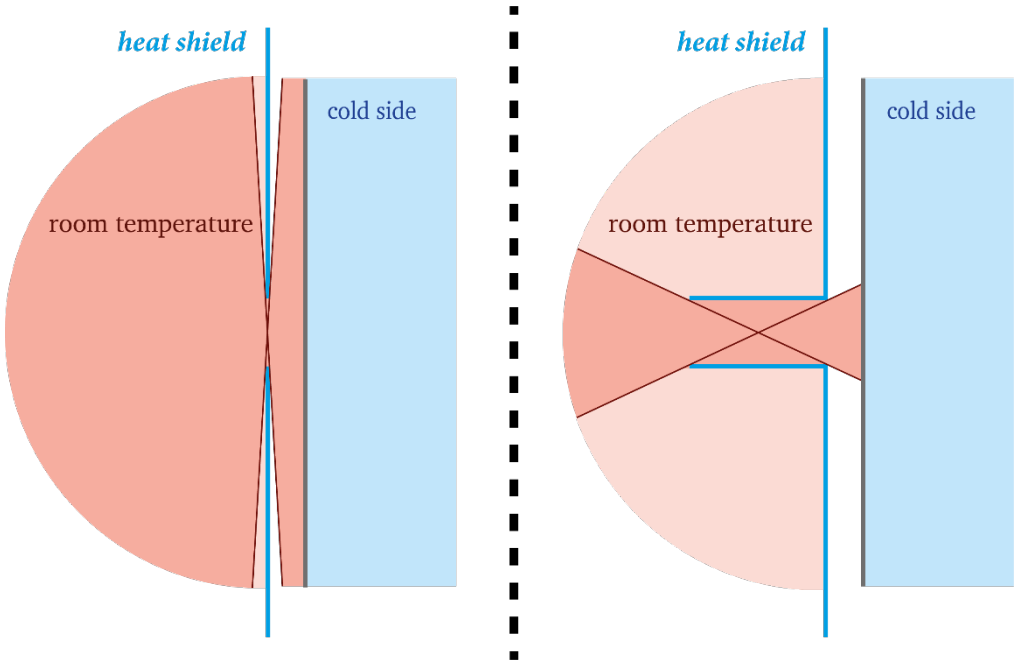

Figure 18: Angular dependency for the blocking of the outside temperature by the heat shields. On the left: plane shield with single hole. On the right: Funnel-shaped hole with same diameter. A large proportion of the external heat radiation is stopped while the electron beam maintains a free path.

With this it is possible to construct a scattering chamber for the helium target. The chamber must be able to be partially connected to the existing geometry of the spectrometer and the beam line. The existing scattering chamber for regular scattering experiments therefore serves as a starting point [36]. Especially the flanges to the spectrometer entrance are no standard

components. For these flanges and some other components there are no drawings available. These dimensions were measured directly at the spectrometer.

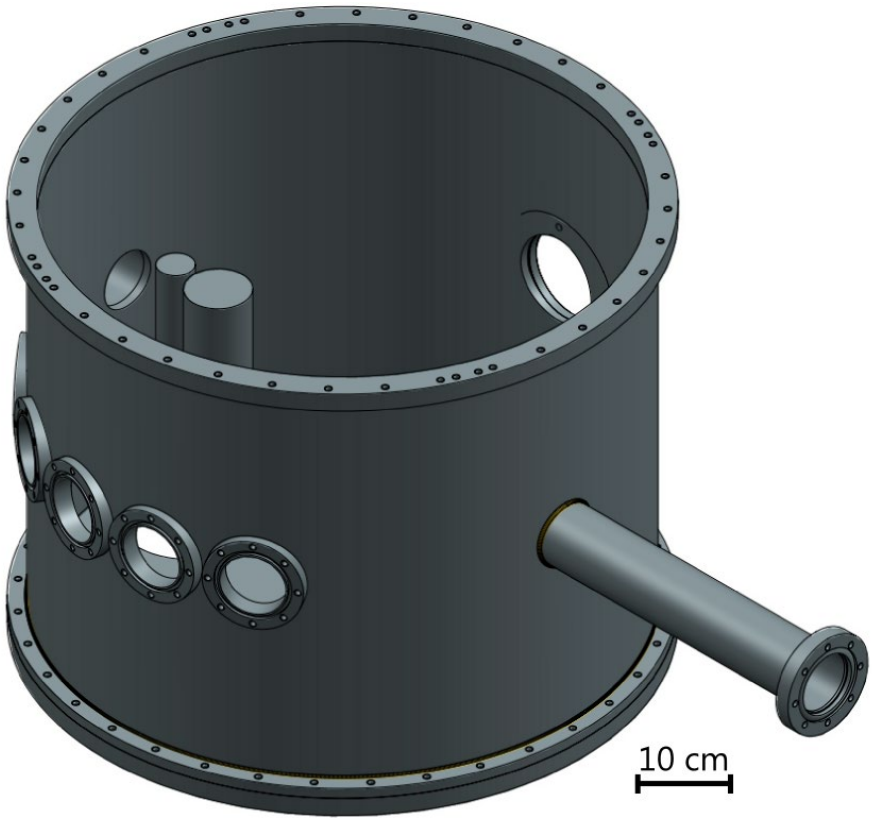

Figure 19: 3D model of the scattering chamber for the helium target. Taken from [18].

Figure 19 shows the result. There is an incoming and an outgoing flange for the main beam along the beam axis. The flanges on the front-left side allow the spectrometer to be flanged at different scattering angles and on the back-right side there is a flange for a vacuum pumping station. There is a total of 6 equidistant spectrometer flanges for scattering angles between 55° and 155°. With beam energies between 30 MeV and 130 MeV, q^2 values according to (2.3) between 0.017 fm^{-2} and 1.41 fm^{-2} are possible.

Two cylinders are visible inside the scattering chamber. These serve as placeholders for a camera system with which the beam position can be displayed on a fluorescent target so that the operators are able to monitor the electron beam during beam operation.

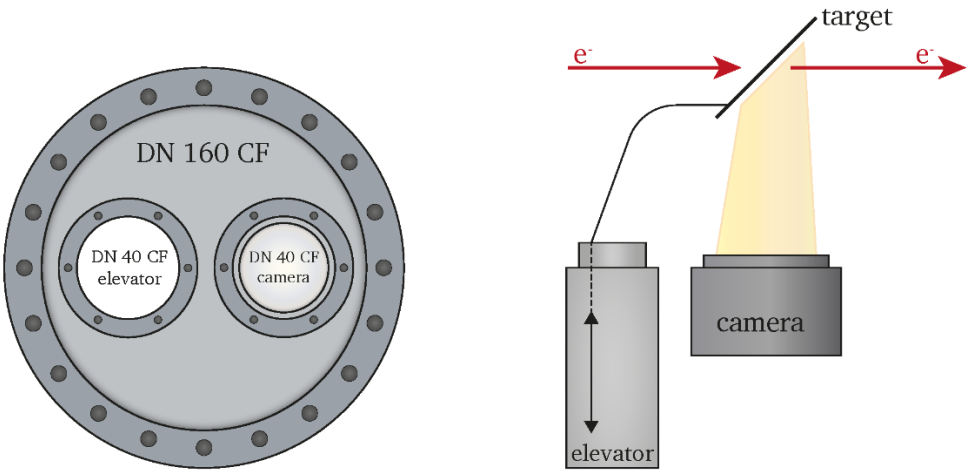

Figure 20: Luminous target system that can be moved into the scattering chamber from below to make the position of the beam spot visible. In contrast to setups with normal targets at room temperature, the luminous target must be mounted on a separate elevator in front of the actual target. Based on [18].

Figure 20 shows a sketch of the luminous target structure. Similar systems are already installed in the beamline of the S-DALINAC. The beryllium oxide fluorescent target is tilted downwards to an angle of 45° and moved to the height of the beam axis by means of an elevator with compressed air. The holder to which the target is attached is equipped with an angle piece so that a camera mounted behind the elevator in the direction of the beam can look straight at the target from below. The camera does not have to be moved. Instead, the focal length of the lens is focused on the beam axis position. If the electron beam hits the beryllium oxide, a beam spot becomes visible from below and can be used at the control room for beam adjustment.

In principle, it would be preferable to be able to observe the beam spot at the target position of the helium target, but this is not feasible in this case because the helium target is frozen in the cold state and therefore cannot be moved to bring a luminous target to this position instead. It is also not possible to observe the beam spot by means of optical transition radiation (OTR) light, because the camera must be mounted outside the scattering chamber at the right place for a certain scattering angle. This would allow a continuous beam spot observation at the actual target position but would require many more holes in the heat shields, which should be avoided in any case.

Technical drawings for the camera system can be found in the appendix 10.1.

In addition to the scattering chamber with the target and the cryostat, some external devices are required. On the one hand a vacuum pumping unit with pre-pump and turbopump to create the vacuum in the scattering chamber. Then a feed pump to reduce vapor pressure of the helium in the superfluid reservoir and thus reduce the temperature of the helium as described in chapter 2.3.2. In order to control the temperature to a certain value, an appropriate device must be attached to the pump, which can adjust the pumping capacity of the pump. Thermometers and a temperature controller are required to measure the temperature of the liquids. Level sensors would also be helpful to monitor the level of each tank.

4.2.2. Calculation of Beam induced Heat load

As already described at chapter 2.2, high-energy electrons lose energy when passing through matter and this energy must of course be deposited somewhere.

The energy loss can be calculated with equations (2.10) and (2.14). For an upper estimation it is assumed that all the energy lost by the electron beam during its passage through matter is deposited in the target material, although especially the bremsstrahlung photons will for the most part escape from the target. The energy loss caused by bremsstrahlung is relatively small in the interesting energy range, but not negligible [37].

As an alternative to equations (2.10) and (2.14), "stopping powers" are tabulated for a whole range of different materials [37].

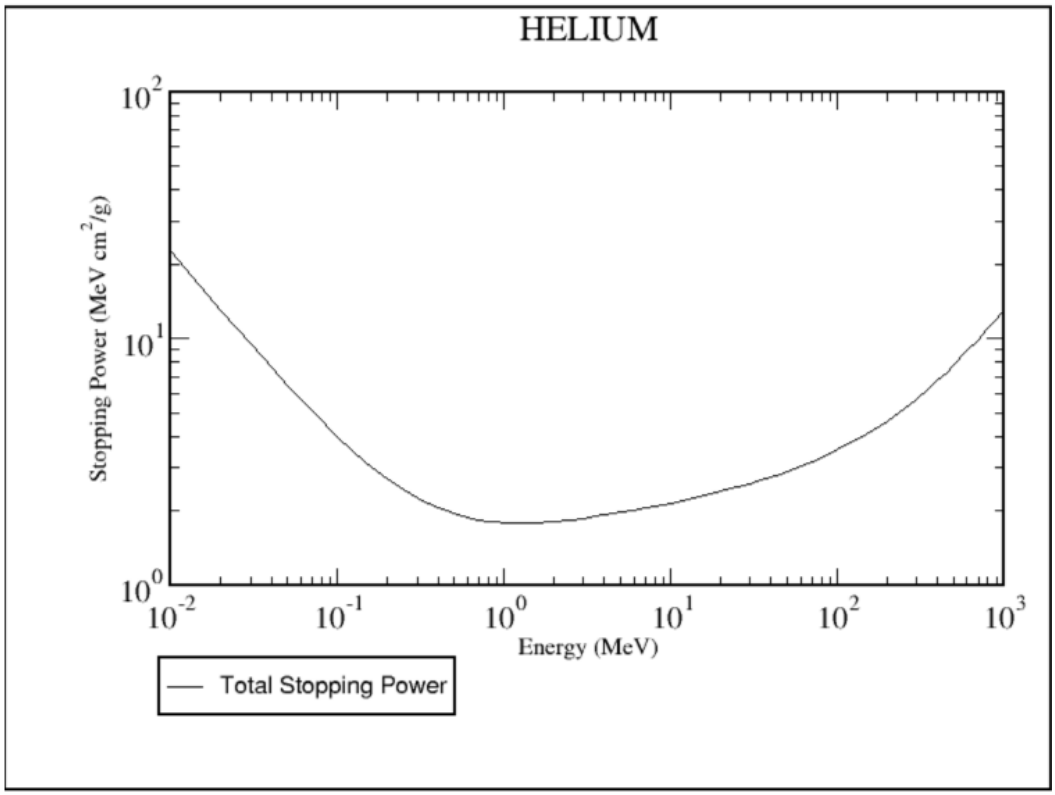

Figure 21: Energy dependent stopping power for fast electrons in helium. Taken from [37].

Figure 21 shows the energy-dependent energy loss in units of $\mathrm{MeV} \cdot (\mathrm{cm}^2/\mathrm{g})$ of electrons in helium, as a function of the energy of the electrons in MeV. The electrons accelerated by the S-DALINAC have an energy between 30 MeV and 130 MeV. The energy range that is of interest here is therefore completely behind the minimum. For an estimation of an upper limit it is assumed that the energy of the electron beam is 150 MeV since all needed values are tabulated for this energy. The tabulated values have the advantage over the values calculated according to equation (2.9) that various numerical corrections have been included and are therefore similar, but somewhat more accurate.

For 150 MeV electrons there is a stopping power of $4.095\ \mathrm{MeV} \cdot (\mathrm{cm}^2/\mathrm{g})$ in helium. With a mass coverage of $50\ \mathrm{mg/cm^2} = 0.05\ \mathrm{g/cm^2}$ this results in an energy loss of

$$4.095\ \text{MeV}\frac{\text{cm}^2}{\text{g}} \cdot 0.05\frac{\text{g}}{\text{cm}^2} = 0.205\ \text{MeV} \tag{4.1}$$

per electron. The S-DALINAC delivers a beam current I with a maximum of 2 µA to the QCLAM spectrometer.

$$I = \frac{Q}{t} = \frac{charge}{time} \tag{4.2}$$

2 µA are therefore

$$\frac{I}{e} = 1.248 \cdot 10^{13}\frac{\text{electrons}}{\text{second}} \tag{4.3}$$

of which every single electron deposits 0.205 MeV in the helium. This translates to $3.284 \cdot 10^{-14}$ J. So, the total current of 2 μA stores a maximum of

$$1.248 \cdot 10^{13} \cdot 3.284 \cdot 10^{-14}\frac{\text{J}}{\text{s}} = 0.41\ \text{W} \tag{4.4}$$

in the helium part of the target.

The window material of the target capsule will be aluminum. Figure 22 shows the energy dependence of the stopping power of aluminum. Form 150 MeV electrons the stopping power is $7.583\ \text{MeV} \cdot (\text{cm}^2/\text{g})$.

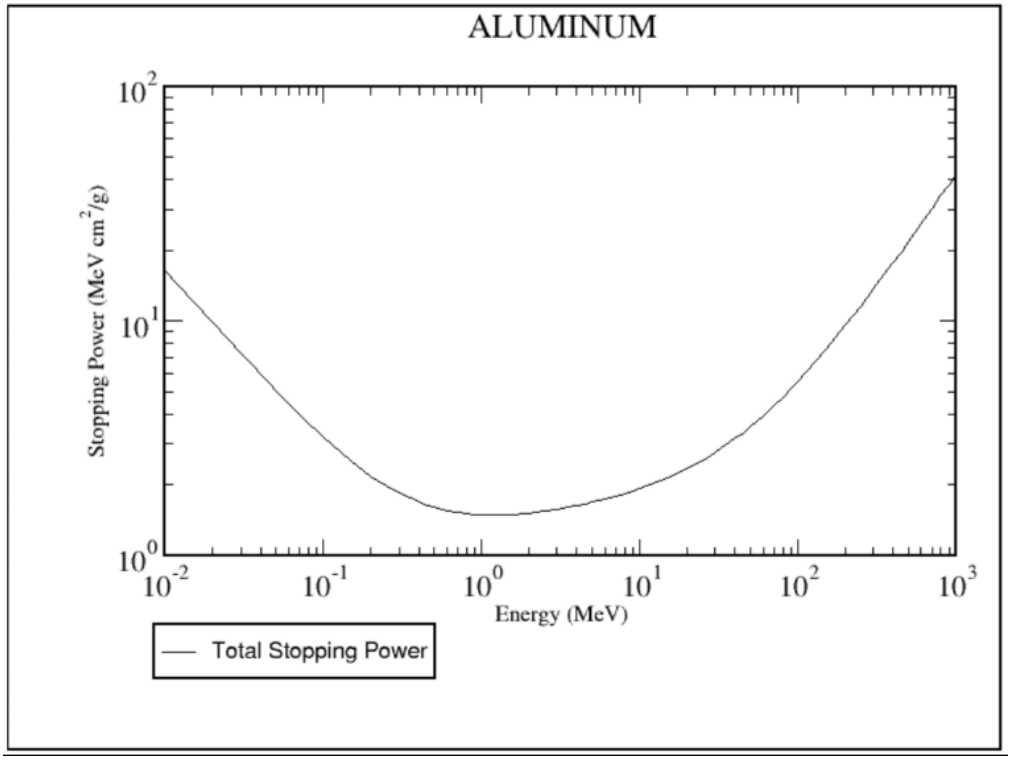

Figure 22: Energy dependent stopping power for fast electrons in aluminum. Taken from [37].

Aluminum has a density of 2.700 kg/m^3. If one assumes a total wall thickness of the windows of 0.4 mm, this results in a mass overage of 108.4 mg/cm^2 and thus a further heat input of

$$7.583\ \text{MeV}\frac{\text{cm}^2}{\text{g}} \cdot 0.108\frac{\text{g}}{\text{cm}^2} = 0.819\ \text{MeV} \tag{4.5}$$

per electron into the target. Thus, a total heat input of 2.05 W results from the sum over the contributions of helium and aluminum. However, this value is an upper estimate, the actual value should be significantly lower.

As soon as the thermal energy deposited in the target is known, it is possible to roughly estimate how much helium will evaporate. This is important to know for the sizing of the helium tanks.

Helium has an evaporation energy of 20.413 kJ/kg [38]. Assuming that the 0.4 W deposited directly in the helium by the electron beam is completely converted into heat of evaporation, i.e. no heat can be removed, then according to equation (4.6) one gram of helium is completely evaporated after 51.03 seconds.

$$\frac{20.413\frac{\text{J}}{\text{g}}}{0.4\frac{\text{J}}{\text{s}}} = 51.03\frac{\text{s}}{\text{g}} \tag{4.6}$$

Thus, 0.0196 g evaporate in one second and 70.56 g in one hour. This corresponds to a liquid volume of 0.56 liters per hour. This is again an upper estimate, but losses due to heat radiation from outside are not considered.

4.3. Count Rate Estimations

To be able to estimate the required beam time for the planned experiments, possible spectra are simulated and counting rates are roughly predicted. The data shown in Figure 23 were measured at the DALINAC in the late 60s [10]. These spectra are used as a basis and will be adapted to the conditions of the QCLAM spectrometer and the planned target geometry as well as the accelerator S-DALINAC. The theoretical cross sections shown in Figure 2 are used to generate possible spectra for other momentum transfers.

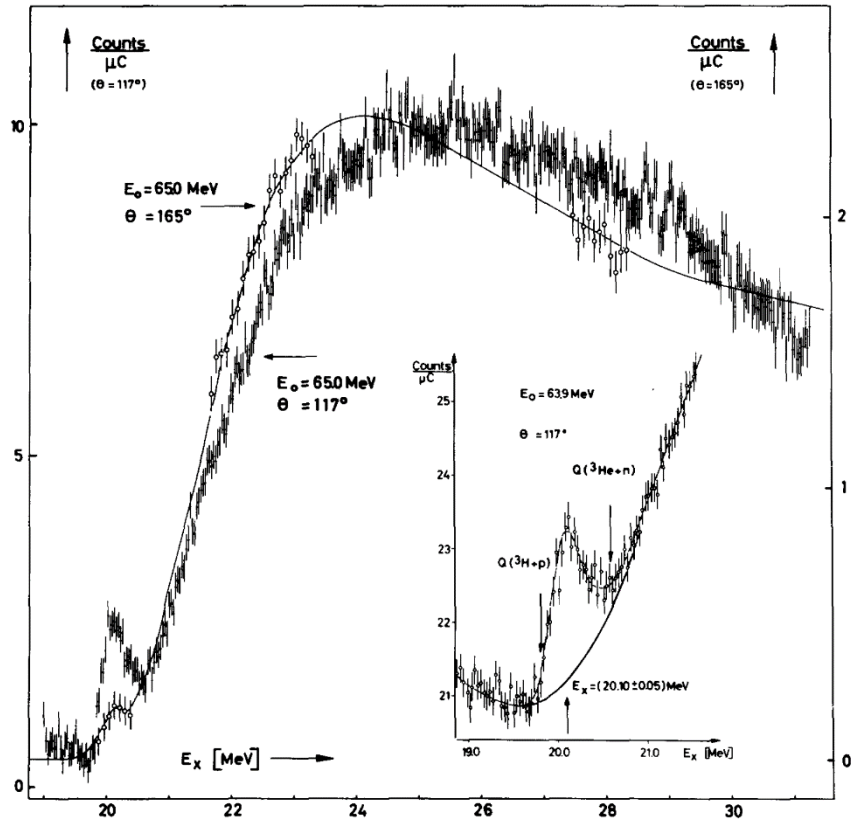

Figure 23: Measured spectrum of the first excited 0^+ state of ^{4}He. The spectra were obtained at the DALINAC in the late 60s [10].

For the measurement shown in Figure 23, a normal liquid helium target with an assumed areal mass density of 120 mg/cm^2 was used. Our target will have an areal mass density of about 55 mg/cm^2. Therefore, the spectra must be multiplied by a factor of 0.42 to fit our target.

The spectrometer that was used was different as well and the detector system had a different functionality. The QCLAM spectrometer uses multiple multiwire drift chambers to detect the scattered electrons. To generate a spectrum, a manual binning must be performed, which can be adapted to the conditions of the experiment. For the simulation of the possible spectra a bin width of 50 keV is used. This width is below the width of the excited state so that the peak is not washed out but is also not to small so that a maximum number of events can end up in the individual bins.

The individual bins are then multiplied by a Poisson distributed random number to generate a statistical variation. Furthermore, the solid angle of the QCLAM spectrometer is significantly larger than the solid angle of the previously used 120° spectrometer. The solid angle of the QCLAM spectrometer is up to 35 msr [29], that of the 120° spectrometer 12 msr [39]. For the simulation of the spectra the full solid angle of the QCLAM spectrometer is assumed. The data must therefore be multiplied by a corresponding factor 2.92.

With these adjustments, the spectrum shown in Figure 23 for a beam energy of 65 MeV and a scattering angle of 117° will appear as shown in Figure 24. For this purpose, a beam current of 2 μA, a measuring time of 1 hour and the maximum possible solid angle of 35 msr for the QCLAM spectrometer were assumed.

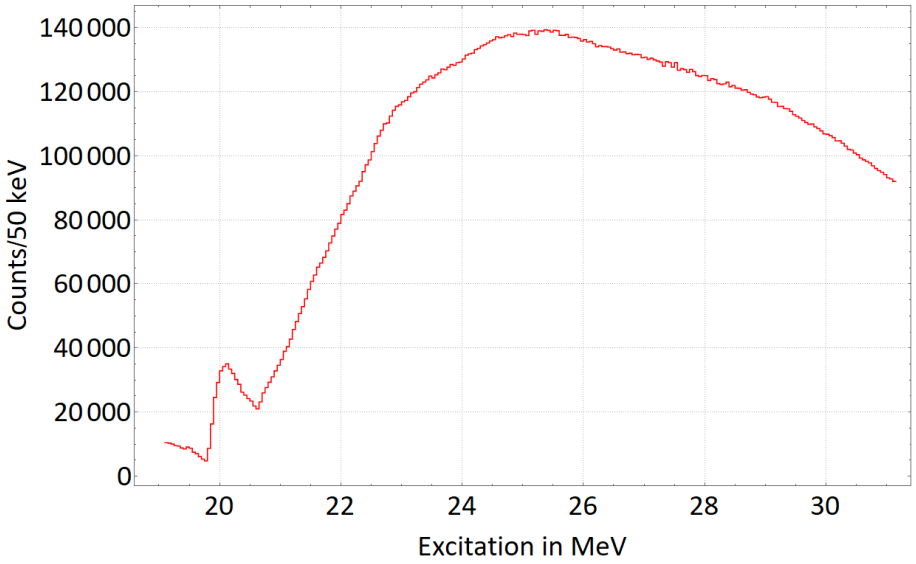

Figure 24: Simulated spectrum for a beam energy of 65 MeV and a scattering angle of 117°. A beam current of 2 µA, a measuring time of 1 hour and the full 35 msr solid angle of the QCLAM spectrometer were assumed.

To obtain spectra for the planned beam energies and scattering angles, the spectrum from Figure 23 for the beam energy 64 MeV and the scattering angle 117° is used. The simple central 3NF line from Figure 2 is used to generate spectra for other momentum transfers since this is the closest to the values measured in [10]. The momentum transfer for a beam energy and scattering angle combination can be calculated according to equation (2.3). For a beam energy of 64 MeV, a scattering angle of 117° and an excitation energy of 20.21 MeV $\left(q(64\ \text{MeV}, 117°)\right)^2 = 0.22\ \text{fm}^{-2}$. The simple central 3NF line is therefore multiplied by a constant factor so that it is normalized to 1 for $q^2 = 0.22\ fm^{-2}$. To calculate scattering rates for other momentum transfers, the spectrum (64 MeV, 117°) is multiplied by the value corresponding to the normalized curve at the matching q^2 value. For the planned beam energy of 49 MeV and the scattering angle 95°, that results in the spectrum shown in Figure 25.

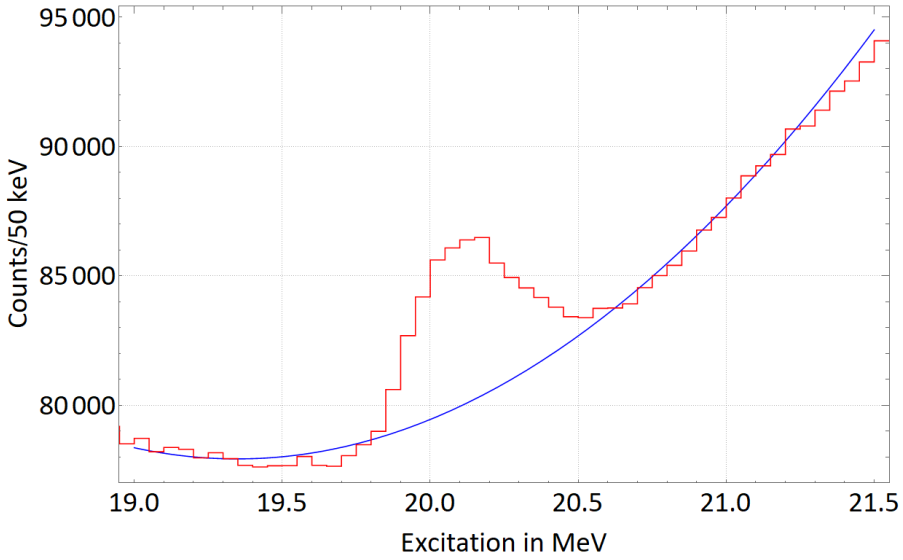

Figure 25: Simulated spectrum for the planned beam energy of 49 MeV and the scattering angle 95°. A beam current of 2 µA, a measuring time of 1 hour and the full 35 msr solid angle of the QCLAM spectrometer were assumed.

To determine how many events are in the peak of the excited state a parabola was fitted to the background. For the given spectrum, 55,000 events per hour for a beam current of 2 μA and the full solid angle of the QCLAM spectrometer are calculated. Estimates for further momentum transfers are summarized in Table 2. If a smaller beam current or a reduced solid angle of the QCLAM spectrometer is used in the measurement, the expected count rates can be adjusted linearly.

Table 2: Estimated count rates for the first excited 0^+ state for different beam energies and scattering angles. The counting rate per hour was rounded to nearest thousands.

Beam energy	**Scattering angle**	**Momentum transfer q^2**	**Counts/hour**
49 MeV	75°	0.06 fm^{-2}	40,000
49 MeV	95°	0.09 fm^{-2}	55,000
60 MeV	95°	0.14 fm^{-2}	107,000
60 MeV	135°	0.22 fm^{-2}	202,000
100 MeV	135°	0.71 fm^{-2}	945,000

The treatment for the longitudinal response function is based on [40] where experiments including evaluation for higher momentum transfers are described. The angle-dependent response function for a given momentum transfer consists of a longitudinal component R_L and a transverse component R_T

$$R_\theta(q,\omega) = \lambda^2 \, R_L(q,\omega) + \left(\frac{\lambda}{2} + \tan^2\frac{\theta}{2}\right) R_T(q,\omega) \tag{4.7}$$

with $\lambda = Q^2/q^2$, which is the squared 4-momentum transfer $Q^2 = q^2 - \omega^2$ divided by the momentum transfer described in equation (2.3), where ω is the energy transfer to the nucleus. The function R_θ can also expressed by the experimental double-differential cross section divided by the differential Mott cross-section

$$R_\theta(q,\omega) = \frac{d^2\sigma(\theta, E_0, \omega)}{d\Omega \, d\omega} \cdot \frac{1}{\sigma_{\mathrm{Mott}}(\theta, E_0)} \tag{4.8}$$

where E_0 corresponds to the initial energy of the electron beam. To get the longitudinal response function $R_L(q,\omega)$, a Rosenbluth separation must be performed. The first step is to record a spectrum. The scattering angle and the beam energy are fixed. The energy transfer, and thus the momentum transfer and the function $R_\theta(q,\omega)$ vary with the excitation energy. Figure 26 shows an arbitrary example spectrum. In a specific measurement fixed quantities are shown in green. All quantities that vary within the same spectrum are shown in red. The spectrum is divided into several bins, integrated over them and $R_\theta(q,\omega)$ calculated according to equation (4.8). For each bin there is a function $R_\theta(q,\omega)$ for a different momentum transfer.

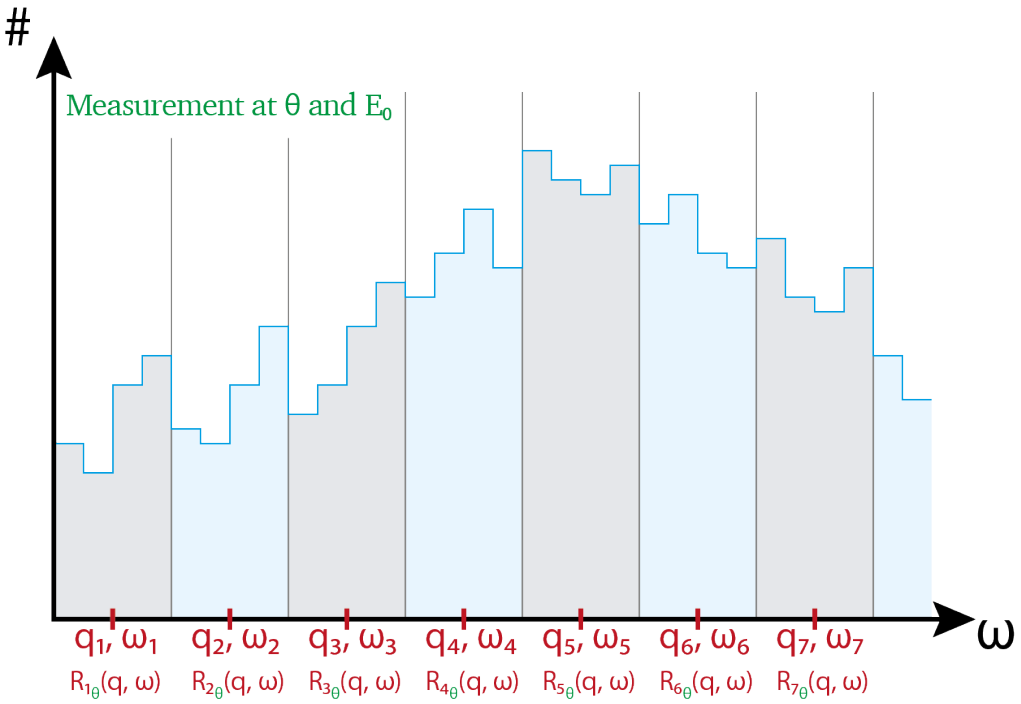

Figure 26: Arbitrary spectrum at fixed scattering angle and fixed beam energy. All quantities that are fixed for this spectrum are shown in green. All quantities that are different for each bin are shown in red.

Next, the individual $R_\theta(q,\omega)$ are plotted over $\tan^2 \theta/2$ as it can be seen in Figure 27. Since the scattering angle is equal for all bins, and thus for all $R_\theta(q,\omega)$, all points appear on a vertical line.

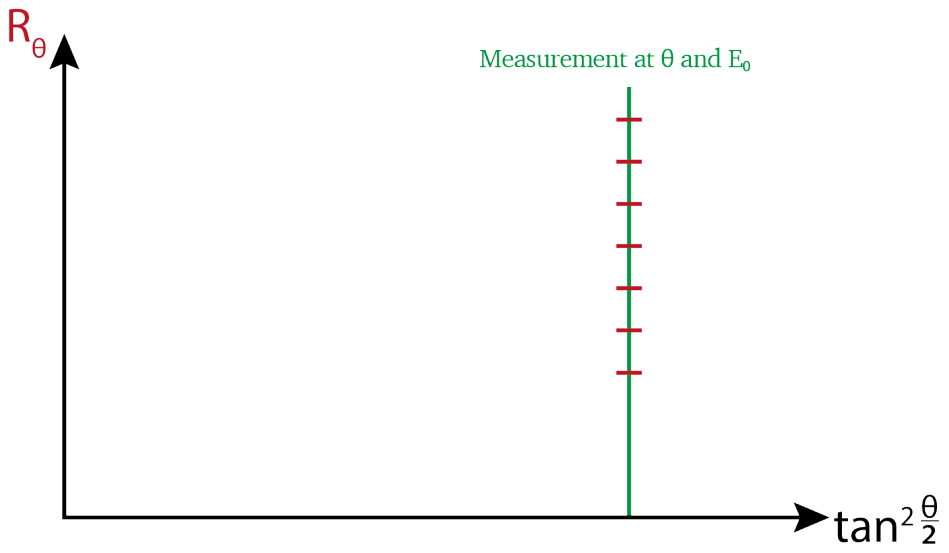

Figure 27: All points $R_\theta(q,\omega)$ obtained by equation (4.8) are plotted over $\tan^2 \theta/2$. Since the scattering angle is the same for all points belonging to the same spectrum, all points are on a vertical line.

To obtain the functions R_L and R_T, several spectra at different scattering angles and different beam energies must be recorded. The $R_\theta(q,\omega)$ are calculated for each measurement and for each bin and then plotted on the diagram as shown in Figure 28. In the next step, the points with

the same momentum transfer can be connected. The functions R_T and R_L then result from the slope and the R_θ axis intercept of the different lines according to equation (4.7).

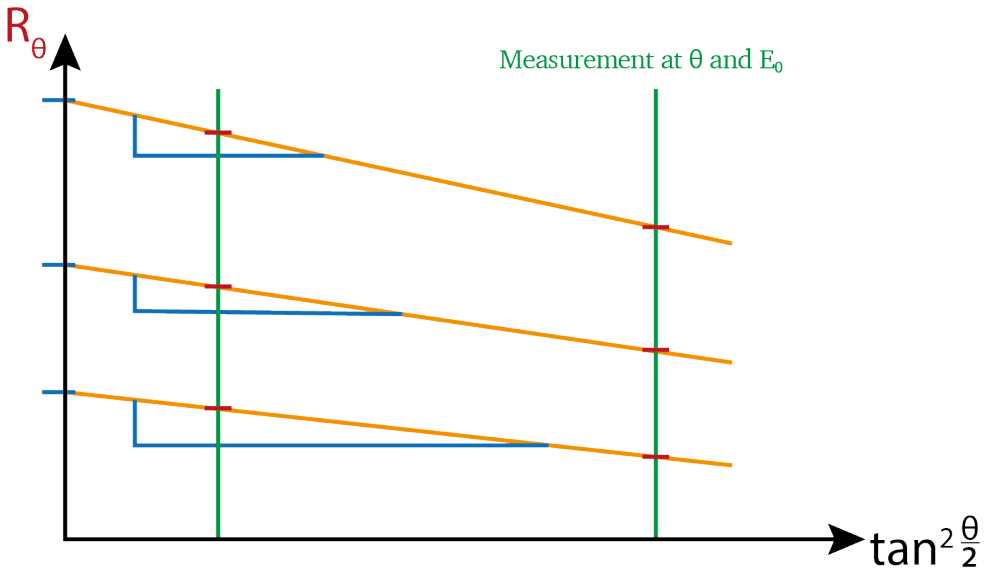

Figure 28: If spectra for different scattering angles and beam energies are recorded and the points $R_\theta(q,\omega)$ are calculated and inserted, points with the same momentum transfer can be connected. The values for R_T and R_L result from the slope and the axis intercept according to equation (4.7).

To estimate the count rate for these kinds of spectra, the theoretical +3NF calculation in Figure 28 is used as a basis. Due to the necessary Rosenbluth separation a simple transfer of the curve to a spectrum is not possible. Therefore, in this case it is assumed that the transverse component is zero. According to equation (4.7), a horizontal line then results for $R_\theta(q,\omega)$.

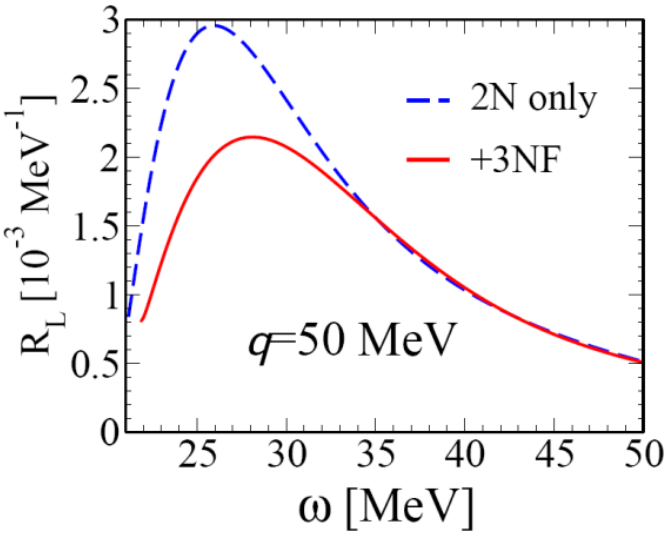

Figure 29: Theoretical longitudinal response functions of ^{4}He as a function of excitation energy, once with and once without consideration of three-body forces [11].

In this case, the experimental cross section can be calculated from the theoretical function R_L using equation (4.9).

$$\frac{1}{\lambda^2} R_\theta(q,\omega)_{R_T=0} = \frac{1}{\lambda^2} \frac{d^2\sigma(\theta,E_0,\omega)}{d\Omega\, d\omega} \cdot \frac{1}{\sigma_{\text{Mott}}(\theta,E_0)} = R_L(q,\omega) \tag{4.9}$$

$$N_{\text{counts}} = \frac{d^2\sigma(\theta,E_0,\omega)}{d\Omega\, d\omega} \cdot \Delta\Omega \cdot t_{\text{live}} \cdot \Sigma_{\text{QCLAM}} \cdot \frac{I \cdot \Delta t}{e} \cdot \frac{\rho dx \cdot N_A}{M} \tag{4.10}$$

According to equation (4.10), to obtain a spectrum with a count rate, the solid angle $\Delta\Omega$ of the spectrometer, the lifetime t_{live} and efficiency Σ_{QCLAM} of the detector system, the number of collected electrons $I \cdot \Delta t/e$ and the number of target particles $\rho dx \cdot N_A/M$ must also be taken into account. For the calculation $\Delta\Omega = 35$ msr, $t_{\text{live}} = 0.8$, $\Sigma_{\text{QCLAM}} = 0.5$, $I = 2$ µA, $\Delta t = 1$ hour and $\rho dx = 55$ mg / cm^2 are assumed.

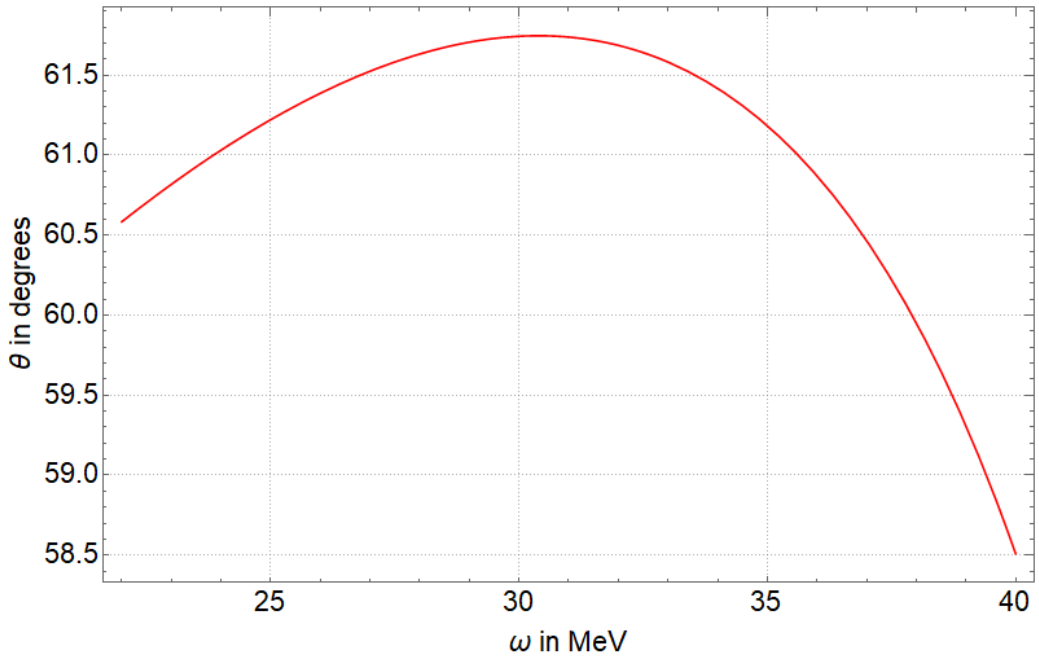

Figure 30: Angle dependence on the excitation energy for the simulated spectrum resulting from Figure 29.

It should also be noted that the function R_L is given for a fixed momentum transfer of 50 MeV. If the function is divided into individual bins, then this results in individual bins for a certain combination of scattering angle and beam energy. As a value for the beam energy, 60 MeV is selected as an intermediate energy for the S-DALINAC. The values that are then used to estimate the count rate are on the curve shown in Figure 30. In Figure 31 the spectrum obtained in this way is shown once in a 3-dimensional representation and once as a projection in Figure 32. Counting rates for lower beam currents and reduced solid angles can easily be scaled down linearly.

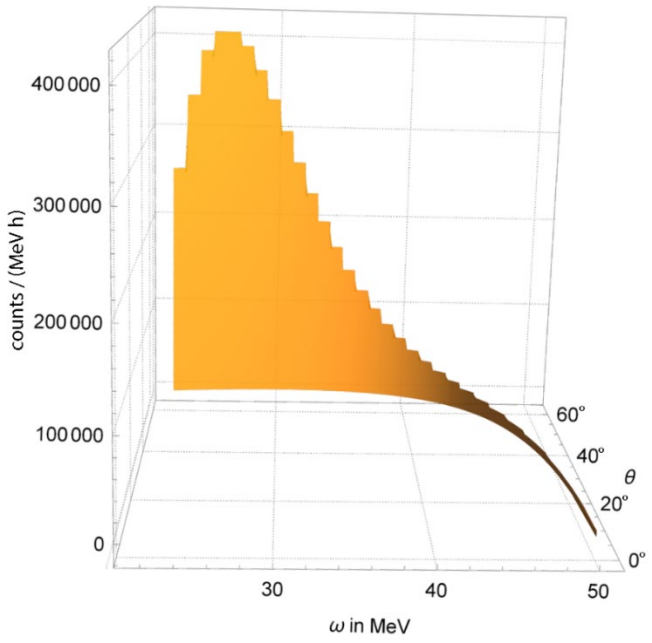

Figure 31: Counting rate estimation for the measurement to determine the longitudinal response function as a function of energy transfer and scattering angle according to equations (4.9) and (4.10).

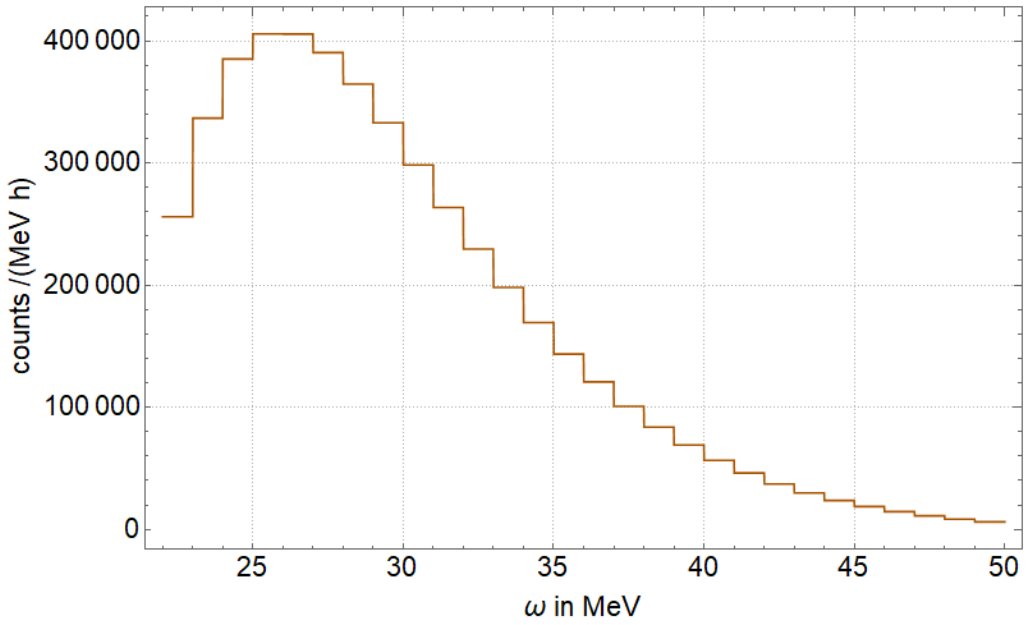

Figure 32: Projection of the count rate estimation from Figure 31 onto the curve of the angular dependence from Figure 30.

5. Target Assembly and Cold Tests

This section describes the actual design of the cryostat and its components, including all the additional components required for the operation. This is followed by a description of the assembly and initial operation. Then the development of a cooling procedure is described and the results of the first cold tests are shown. The target including scattering chamber and cryostat is manufactured by the company CryoVac.

5.1. Assembly and Vacuum Tests

Figure 33 shows a cross-section of a CAD drawing of the manufactured cryostat system. It consists of an outer vacuum chamber, three cryo-tanks, the target cell and three actively cooled, highly polished aluminum heat shields. The uppermost tank has a volume of 18.5 liters and is filled with liquid nitrogen. Its main purpose is to cool the outermost heat shield layer as well as to operate as a thermal sink for wiring. The radiation shield blocks direct room temperature radiation to the LHe system. The middle tank (He I tank) has a volume of 16 liters and is filled with liquid helium at the boiling temperature of 4.2 K at atmospheric pressure. This tank is used firstly to cool the second radiation shield layer to helium temperature and secondly it serves as a storage tank for the second helium tank below. The third tank (He II tank) has a volume of 5.6 liters. It is filled with liquid helium via a capillary from the He I tank. The flow through the capillary can be controlled and blocked with a cryogenic in-line needle valve. By means of a vacuum pump (feed pump) connected to a separate pumping port of the He II tank, the vapor pressure of the liquid in the He II tank can be reduced and thereby the temperature of the liquid helium in this tank will be decreased as it was described in chapter 2.3.2.

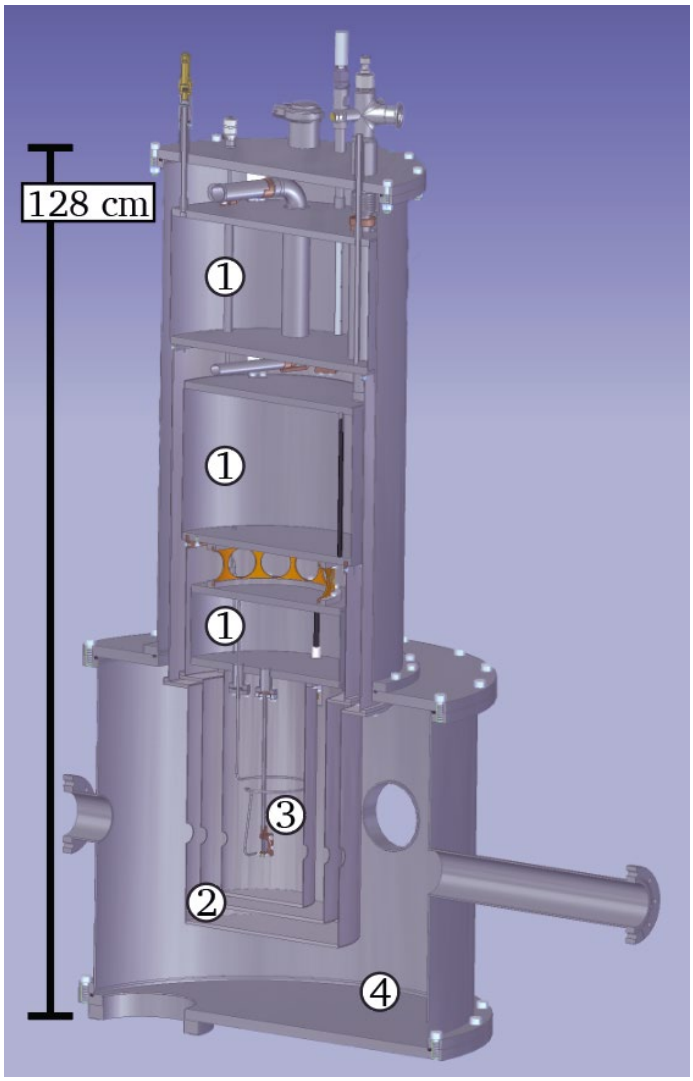

Figure 33: Cross section through the 3D model of the cryostat. Three cryo-tanks ①, multi-stage heat shields made of aluminum ②, and the target cell ③ made of copper with aluminum windows are in an outer vacuum chamber ④ made of stainless steel. There are several holes in the shields to allow both the electron beam and the scattered electrons to pass. Slightly changed taken from [19].

The target cell is supplied with helium from the He II tank and is thermally shielded by the radiation shield of the He II tank, such that the temperature stability of the target is further increased. The target cell is directly connected to the reservoir of the He II tank. The outer shell of the target cell is made of copper. Two circular 0.20(1) mm thick aluminum plates, serving as windows. They have a free diameter of 20 mm and are clamped between the copper frames at a distance of d = 3.7(2) mm. Indium serves as sealing material. The complete target cell unit is fixed with two rotatable CF16 flanges at the bottom of the He II vessel, so that the target cell can be rotated according to the scattering angle of the spectrometer as described in chapter 4.2.1 and Figure 17. There are two stainless steel tubes connecting the target cell with the He II tank. One tube starts almost at the bottom of the He II vessel and the second one sticks into the He II vessel so that its opening is always in the vapor phase. When filled with superfluid helium at a temperature of 1.8 K it provides an expected areal mass density of $\overline{m_0} = \rho_{\mathrm{He}} \cdot d = 54(2)\ \mathrm{mg/cm^2}$ on perpendicular incidence of the beam. However, the rotation of the target cell relative to the beam axis increases the effective target thickness to

$$\overline{m_{\mathrm{eff,trans}}} = \frac{\overline{m_0}}{\cos\frac{\theta}{2}} \tag{5.1}$$

if the target is placed in transmission geometry and to

$$\overline{m_{\mathrm{eff,refl}}} = \frac{\overline{m_0}}{\sin\frac{\theta}{2}} \tag{5.2}$$

if the target is placed in reflection geometry [18]. In each radiation shield there are eight circular openings which allow the primary electron beam and the electrons scattered into the spectrometer to pass through the target without additional scattering. Openings not used for the specific spectrometer settings can be closed by means of aluminum flanges to reduce thermal load on the system. This means that each time a new scattering angle needs to be set in the experiment, the entire cryostat must be warmed up so that the flange of the previous scattering angle can be closed and that of the new scattering angle can be opened. However, since the target must be rotated to the correct angle anyway, this makes no real difference. But it means a forced interruption of the experiment for about 2 weeks for each new scattering angle. Another way to change the momentum transfer is to change the energy of the electron beam according to equation (2.3). Usually it takes much longer to change the electron energy instead of the scattering angle, because the whole accelerator settings must be redone, but in the case of the helium target it should at least be considered as an option.

The scattering chamber itself is made of stainless steel. The wall thickness is 3 mm. Possible scattering angles are 55°, 75°, 95°, 115°, 135° and 155°. The flanges to the spectrometer are non-standard components. The beam lines to the accelerator and the Faraday Cup are connected with DN 63 CF flanges. On the side facing away from the spectrometer there is an DN 100 ISO-K flange for the connection of a vacuum pumping unit. At the bottom of the chamber the DN 160 CF flange for the camera system can be connected. Plans for the scattering chamber, including the flanges to the spectrometer, can be found in the appendix 10.2.

The upper cryostat was delivered fully assembled with all pipes, sensors, tanks, and super insulation foil, ready to use. Only the transport lock had to be removed, which was intended to protect the sensitive heat shields and the unstably mounted tanks during transport. It is especially important to remove the screws in the correct order because the tanks are only fixed with very few connection points inside the cryostat to avoid thermal bridges. If the transport lock is removed by unscrewing the screws that hold it in place in the wrong order such that the weight of the transport lock hangs on one side of the tank or the whole weight of the transport lock on the wrong tank, the tank could be severely damaged or even torn off. An instruction in which order the screws must be loosened can be found in the operating manual of the cryostat. In general, when working on the cryostat, including the removal of the transport lock, care must be taken to ensure that the cryostat is never tilted and does not wobble or vibrate strongly, as this could also cause the tanks to break off or be otherwise damaged. If the cryostat needs to be transported again in the future, the transport lock must be reattached in reverse order.

The rest of the target system was delivered in individual pieces and had to be reassembled. There were no instructions what to put where, but all parts were made very accurately and fit together very well. Figure 34 shows a photo of the assembled cryostat and the target cell. To lift the upper cryostat, two crane lifting eyes are screwed into designated threads in the lid of the cryostat. If the entire cryostat including the scattering chamber is to be lifted, the scattering

chamber is screwed onto the cryostat and the entire system is lifted by the crane lifting eyes on the lid of the upper cryostat.

On the photo with the target cell on the righthand side the two connecting tubes to the He II vessel can easily be seen. The thicker tube is used to fill the cell with superfluid helium. It is located exactly in the vertical axis of rotation of the cryostat, so that the target cell is rotated around this tube depending on the scattering angle. The thinner tube ends in the gaseous phase of the He II tank. This tube is flexible so that it can adapt to the rotation of the thicker tube.

Figure 34: Photos of the mostly assembled cryostat in the laboratory, with the scattering chamber and some of the heat shields on the left and the target cell connected to the cryostat on the right.

Vacuum tests could then start. During these tests, a few adjustments must be made to the vacuum pump. This is always the case if the cryostat was open for a longer time period and is to be put under vacuum again. The tanks of the cryostat are wrapped with many layers of super-insulation foil between which water from the air humidity accumulates. To be able to pump gas out of the spaces between the foils, the foils are perforated with many small holes. However, the holes are as small as possible in order not to reduce the effectiveness of the foil unnecessarily. Especially when a lot of moisture is collected between the layers, it takes a relatively long time to get rid of the water between the layers and to create a good vacuum. A Pfeiffer HiCube is used as a vacuum pumping station. An oil-free diaphragm pump MVP 070 backing pump and a HiPace 300 DN 100 ISO-K turbopump are installed in it. Basically, a

pumping station of this type functions largely automatically. When the pump is switched on, the backing pump activates first, and then the turbopump automatically starts to spin as well.

However, in the case of the humid cryostat, the problem arises that the pressure inside the vacuum chamber cannot be reduced fast enough by the backing pump. The turbine of the turbopump is slowed down too much by the residual gas and does not reach the specified switching point within the predefined timespan. In order not to damage the turbopump, the entire pump system is shut down with an error message and vented. The vacuum chamber of the cryostat is also vented during this process.

To prevent this, the turbopump must be switched off at the pumping station with setting no. 23 (→ MotorPump off - use the arrow keys to switch to the desired setting, then press both arrow keys simultaneously to select or confirm the selected setting). Then the pumping station is switched on and the pre-vacuum can be pumped. It is worthwhile to use dry nitrogen to aerate the vacuum chamber once every few hours and then pump the vacuum again. This procedure helps to flush residual water out of the insulation layers more quickly. The pumping station does not have to be switched off for this. As soon as a good backing pressure is reached, the turbo pump can be switched on again (setting no. 23 → MotorPump on).

It is important to make sure that a good vacuum pressure is reached before starting the cooling of the cryostat. As soon as the tanks are cooled with liquid nitrogen, the pressure in the vacuum chamber drops sharply as residual gas particles freeze on the tanks and the heat shields, thus reducing the function of the polished heat shields. For this reason, it is also advisable to fill only the nitrogen tank first. The helium tanks can then be filled with nitrogen for pre-cooling when the vacuum does not change any further.

5.2. Cold Test with liquid Nitrogen

After the assembly of the cryostat and the achievement of a good vacuum, the sensors had to be connected to the measuring instruments to start the cold tests. It is important that the cables are plugged into the correct sockets on the cryostat lid and the measuring instruments, otherwise some of the installed sensors may be damaged. The type and shape of the plugs would make incorrect wiring possible, so special care is required. In addition, the description of the socket locations in the operating manual of the cryostat has errors. In order to simplify the correct cabling in the future, labels have been attached to the cables, the ports on the cryostat and the sockets of the display units.

For the first cold test only the nitrogen tank was filled with liquid nitrogen. A level sensor is installed in this tank, which displays the level of the tank either in absolute cm or relative in %. A calibration of the sensor was carried out as part of a bachelor thesis [41]. The nitrogen inlet is marked with NI on the edge of the cryostat lid, the nitrogen outlet with NO. Figure 35 shows both with a corresponding marking. To fill the tank, the cap is simply removed from the inlet tube. If the tank is not being filled, the cap should be put on the inlet again to prevent contamination of the tank. For the nitrogen outlet, it must be ensured that it cannot become blocked. Depending on whether the cryostat is on the floor or on a platform, and depending on the size of the person working with the cryostat, it may be useful to attach a piece of silicone tubing to the nitrogen outlet so that the working person does not inhale the evaporating nitrogen excessively. During filling, there should be a slight overpressure up to a maximum of 200 mbar on the nitrogen can used for filling.

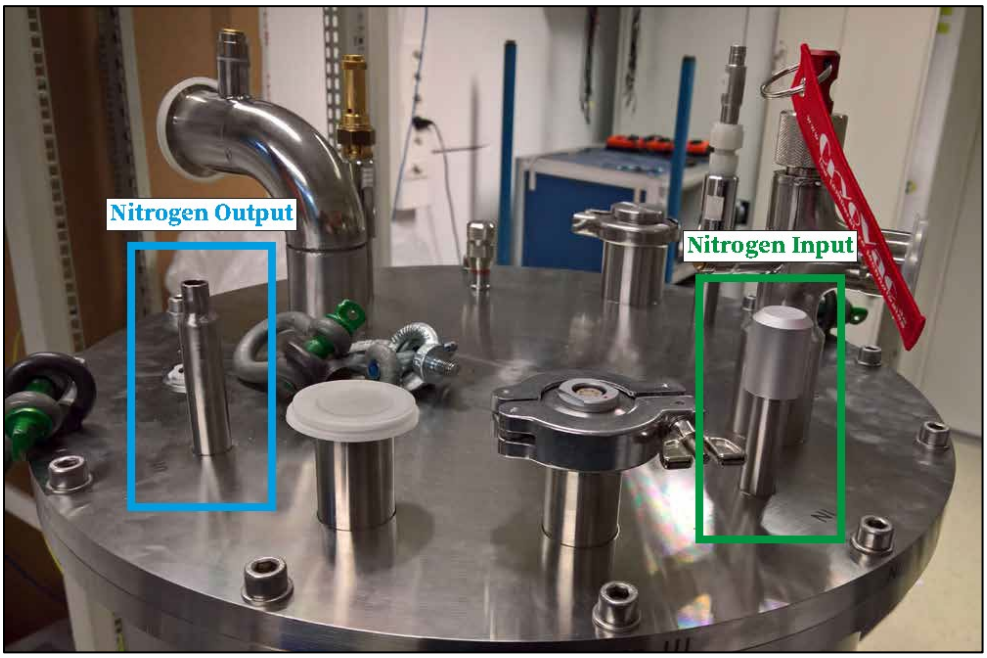

Figure 35: Lid of the cryostat. The nitrogen inlet is located on the right and is closed with a lid that can be simply pulled off. The nitrogen outlet is on the left side.

Right after filling, the level display fluctuates relatively strongly by several millimeters, as the value read by the sensor depends on the temperature and the entire tank must initially cool down to nitrogen temperature. This process takes about 48 hours. After that, the display of the filling level does not fluctuate at all. Figure 36 shows the level development after the first filling of the nitrogen tank.

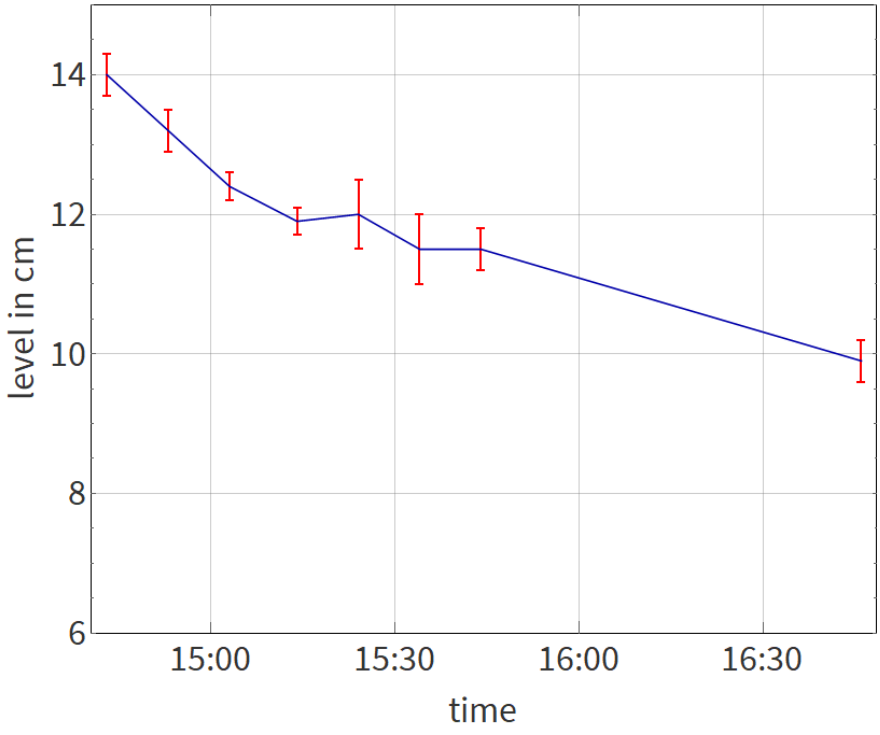

Figure 36: Gradient of the filling level display after the first filling process. At the beginning, the displayed values fluctuate strongly.

Figure 37 shows the filling level curve over a larger time period. In the meantime, the tank has been refilled with liquid nitrogen two times. After the whole tank has cooled down, about 0.3 cm evaporate per hour.

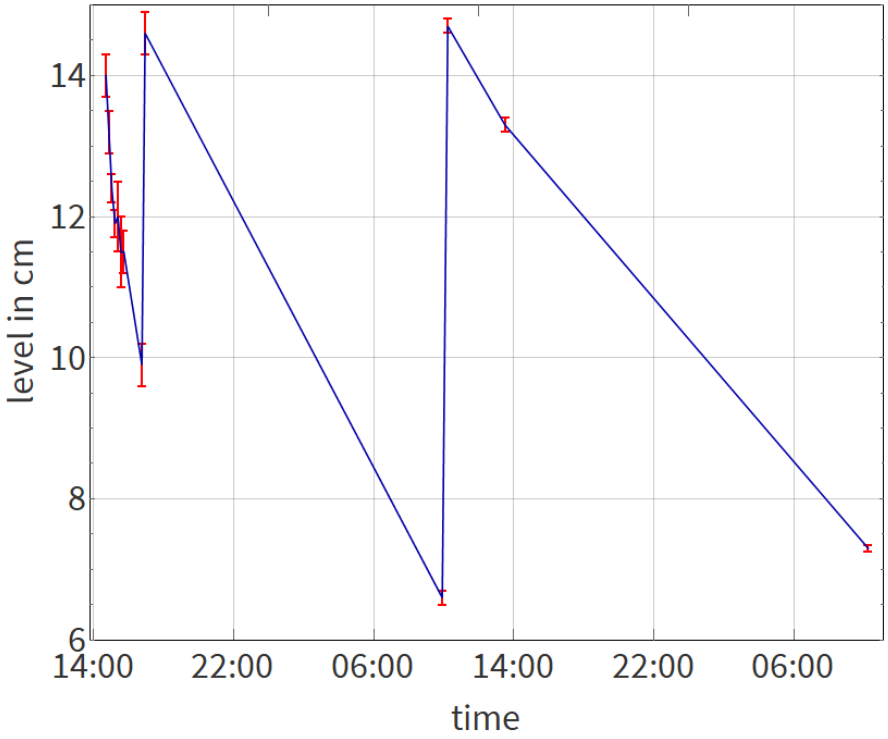

Figure 37: Level curve of the nitrogen tank after the first filling process over a slightly longer period. The fluctuation of the measured values decreases significantly after the tank has cooled down completely after about 48 hours.

Next, the He I tank was filled with liquid nitrogen. This tank has a level sensor for liquid helium and a diode temperature sensor located at the bottom of the tank. The level sensor only works at helium temperatures and cannot be used for filling with nitrogen. Instead, the temperature display can be used for a first orientation. Figure 38 shows the inlet and outlet of the He I tank. The inlet is not marked on the lid but has a red metal plug in it, the outlet is marked with HO I. The seal of the helium inlet can be screwed open and closed. It must permanently be ensured that the helium outlet is never blocked, while there is any cold liquid inside the tank.

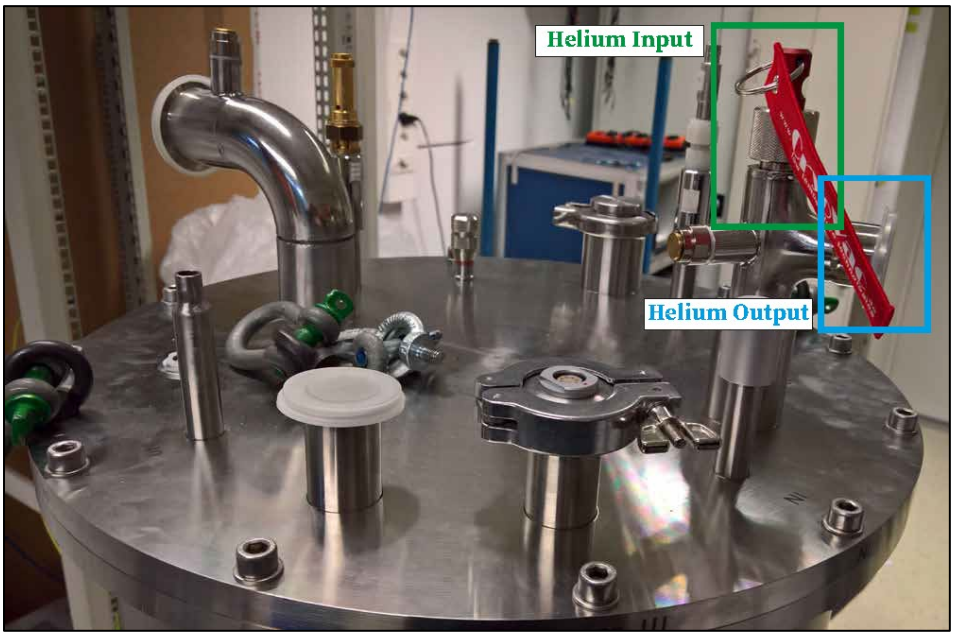

Figure 38: The lid of the cryostat marked with the helium inlet and the helium outlet of the He I tank. The plug of the inlet is secured with a screw cap. As soon as the tank is filled with cold liquid, the cap must be removed from the helium outlet.

During the filling process, the temperature display of the tank decreases continuously until it stops at the boiling temperature of nitrogen. As soon as the temperature stops changing, it starts to form liquid inside the tank. Since there is no direct way to monitor the level, care must be taken during the filling process to prevent the tank from overflowing. To check the level, the filling process can be interrupted, and a plastic rod can be inserted into the filling opening. After a short time, the rod is pulled out again and briefly waved through the air. A layer of frost forms where the rod was immersed in the liquid, which can be measured with a folding rule or similar. As soon as the tank cooled down completely, no liquid evaporates within the measuring accuracy of the rod method if liquid nitrogen is still present inside the nitrogen tank.

To fill the lower He II tank, the needle valve (Figure 39) must be opened. The temperature in the He II tank is measured by a calibrated Cernox CX1030 sensor which is located at the bottom of the tank. The level indicator also only works for liquid helium temperatures. However, there is no way to measure the level in the He II tank using the rod method. Therefore, this tank must be filled very carefully. The outlet of the He II tank is marked with HO II. A self-regulating heating hose can be connected to this outlet, which in turn is connected to a Pfeiffer DUO 65 feed pump. The pumping rate can be specifically reduced with the aid of a control block between the heated hose and the feed pump. If the pump is used to pump the nitrogen-filled tank, the tank cools down to 63 K, which corresponds to the melting temperature of nitrogen.

Overall, the cold test with liquid nitrogen was successful. The cold test with helium could then start.

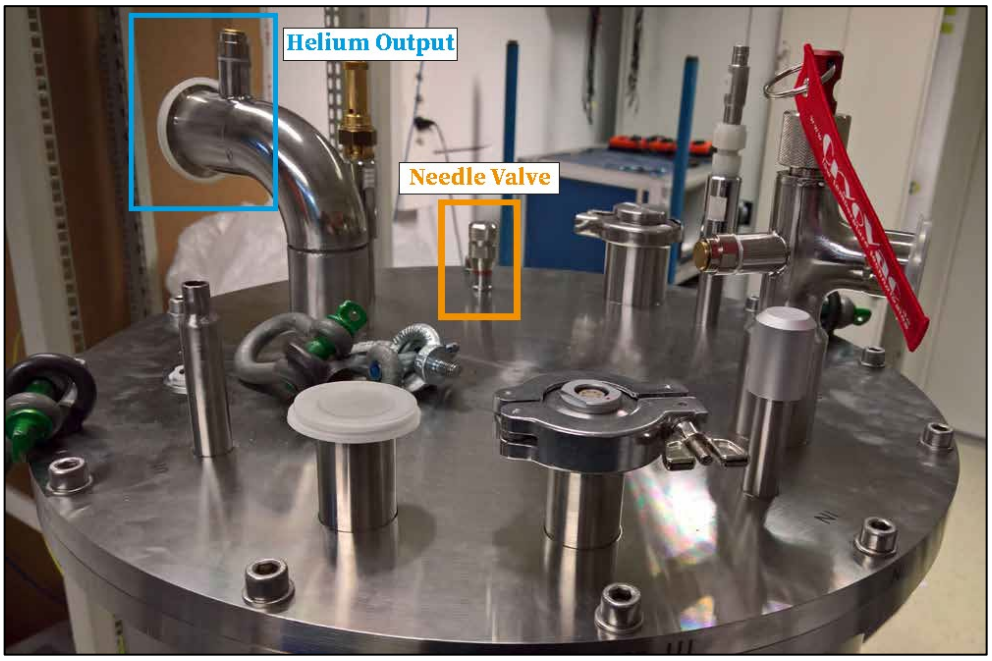

Figure 39: The lid of the cryostat marked with the outlet of the He II tank and the adjusting screw of the needle valve between the He I tank and the He II tank. A self-regulating heating hose will be connected to the outlet of the He II tank, which will then lead to a feed pump to cool the liquid inside the tank.

5.3. Cold Test with liquid Helium

Since the cryostat is too tall to insert the helium transfer line from above into the cryostat lid without hitting the ceiling of the laboratory room, the test with liquid helium cannot be performed in the laboratory. Instead, the target was set up in the experiment hall at the QCLAM spectrometer. In this context, it was possible to test at the same time whether the scattering chamber could be installed in the QCLAM beamline in a correct manner.

One problem encountered was that the CF flanges of the new scattering chamber to the beam line were not designed to be rotatable. Also, the flanges of the beamline which are connected directly to the scattering chamber are not rotatable, so that the two flanges could not be connected at first. However, there are enough rotatable flanges in the beam line, so that the beam pipe pieces could be turned to fit. The scattering chamber was aligned with a cross line laser at the height marks of the spectrometer as well as other position marks distributed in the experimental hall, of which, unfortunately, the correctness and accuracy is not exactly known. To better determine the intended center of the scattering chamber, the spectrometer was rotated around it. In principle, the spectrometer should be flange-mountable to all flanges of the scattering chamber if the center of the scattering chamber is at the correct position. However, the correct rotation of the scattering chamber relative to the beam axis cannot be determined in this way. And since the connecting piece at the entrance of the spectrometer is not exactly straight due to an assembled bellow, the determination of the center with this method is not overly exact either.

The imprecise alignment of the beam line on the one hand and the scattering chamber on the other hand caused problems later in the experiment. In the meantime, the correct beam axis together with the correct center of the scattering chamber has been determined by the geodesists from Frankfurt who have already assisted in the improved alignment of the

accelerator [42]. The axis of rotation of the spectrometer determined within this context is the most important fix-point for any alignments.

Figure 40 shows the cryostat connected to the spectrometer. The vacuum chamber with the target and the cryostat is in the middle ①. In front of it ③ is the vacuum pumping station. ② shows the feed pump used to cool the liquid below the atmospheric pressure boiling temperature. A self-regulating heating hose ⑤ warms up the cold helium exhaust gas to about room temperature before it reaches the pump, so the oil inside the pump cannot freeze. On the left are the readout devices ④ that are connected to the network via Ethernet. The EPICS IOC required for this was created as part of a Bachelor thesis [41,43]. The QCLAM spectrometer is partly visible in the background.

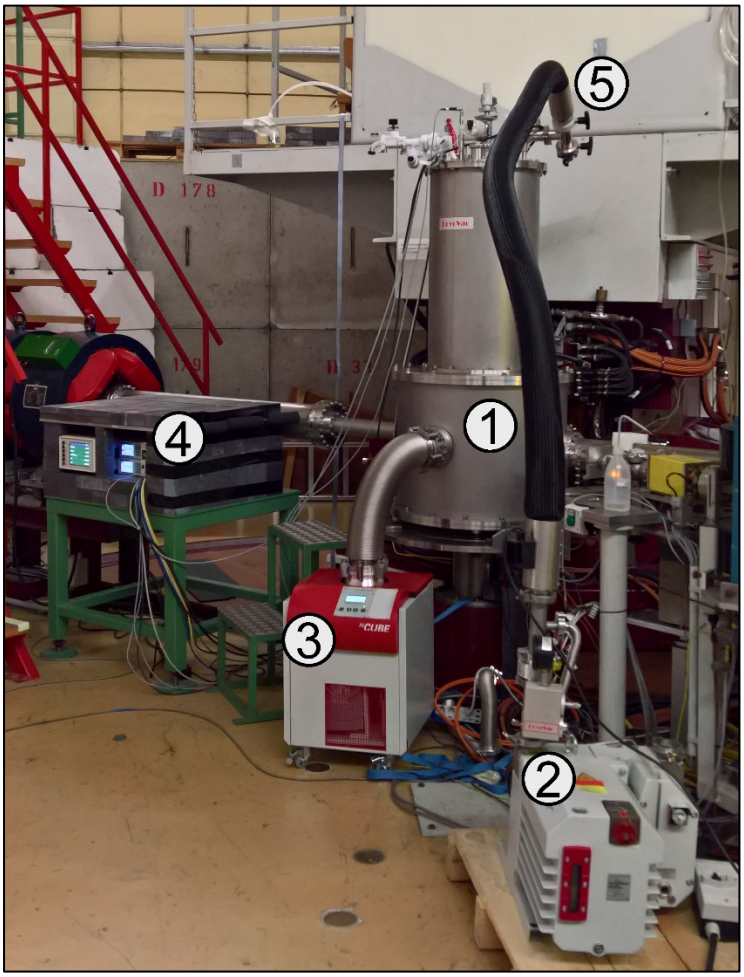

Figure 40: Photography of the assembly of the target at the QCLAM spectrometer. The vacuum chamber with the cryostat and the target cell inside can be seen in the middle ①. The corresponding vacuum pumping station is placed in front of it ③. A feed pump with connected control block at the front right ② is used to cool the liquid helium below the boiling temperature. A self-regulating heating tube ⑤ warms up the helium evaporated helium gas before it enters the pump. The readout electronics are on the left ④.

For the cold test itself, the cryostat must first be filled with liquid helium. This requires a relatively precisely defined procedure, which had to be developed at the beginning. The first step is to create a good vacuum. Depending on the weather conditions this can take up to 2 days. Then the cooling procedure can be started. The vacuum chamber of the QCLAM spectrometer

should be separated from the scattering chamber by closing the lever valve between the spectrometer and the scattering chamber.

Then, the whole system is pre-cooled by filling the nitrogen tank and then, when there is no decrease in the vacuum pressure anymore, the He I tank with liquid nitrogen. During this procedure, the needle valve connecting the He I tank and the He II tank must be closed. As soon as there is a sufficient level of liquid nitrogen in the He I tank the needle valve can be opened carefully allowing liquid nitrogen to drip into the lower tank and evaporate, whereby also the He II tank is cooled by the enthalpy of the evaporating nitrogen. The needle valve must be closed before liquid nitrogen starts to collect within the He II tank, as it will not be possible to remove residual liquid nitrogen in an easy manner from the He II tank. Therefore, the needle valve will be closed above 80 K. This procedure must be repeated several times as the He II tank warms up due to the thermal mass connected to this tank, namely the radiation shield and the target cell with its support.

Once the He II system and the cell will reach stable 90 K, the precooling can be finished and the remaining liquid nitrogen can be pressed out of the He I tank by means of a tube inserted through the top quick lock. For this purpose, an additional end piece was constructed for the helium transfer line, which extends completely to the bottom of the He I tank. As residual liquid nitrogen in the He system, including the cell, will freeze when further cooling down the system with liquid helium, which might cause a blocking in the tubes, it must be made sure, that all nitrogen and possible liquid oxygen has evaporated. To ensure that, the complete He system will be let warm up again to about 100 K.

Then the filling of the helium tanks with liquid helium can be started. The liquid helium can be picked up from the solid-state physics department with a Dewar vessel designated to this purpose. Care must be taken to ensure that the Dewar is tilted as little as possible and that the pressure in the vessel does not become too high. Then the helium can be transferred to the cryostat. For this purpose, there is a helium transfer line specially made for this cryostat which consists of three parts. A fixed section is completely inserted into the transport vessel. A partially flexible connecting piece is attached to it. The third part is inserted into the He I inlet of the cryostat and screwed tight. It is important to ensure that the correct end piece is attached to it. A photography is shown in Figure 41. Most parts of the helium line consist of thin-walled vacuum-insulated tubes, which are quite sensitive. Therefore, the lifter must be handled very carefully, and the flexible part must not be bent too much.

Figure 41: Part of the helium lifter that is inserted into the cryostat. The angled part is always used and can be connected to the flexible part of the helium lifter on one side. On the other side, one of the two sections pictured is screwed on. Part “a” was supplied with the siphon and is intended for filling the He I tank with liquid helium. Part “b” was additionally produced and used during the pre-cooling process to press liquid nitrogen out of the He I tank.

Once all sections are in position, the two open ends of the helium line can be joined. The tap on the helium vessel is turned on briefly to flush the helium line with helium gas. Then the two ends can be connected. The tube of the transfer line has been at room temperature when it was immersed in the liquid helium, so that there is already a certain overpressure on the transport vessel. If the pressure becomes too low, a helium gas cylinder can be connected to increase the overpressure up to 200 mbar again. A higher overpressure only causes higher helium losses and has no further advantages. Unfortunately, there is no helium return line in the experimental hall. All the evaporated helium is blown into the air and is therefore lost. Keeping helium losses as low as possible becomes even more important. As soon as helium is to be filled into the helium tanks, it must be ensured that there is always a liquid level in the nitrogen tank. The feed pump must be connected to the He II outlet. The temperature of the two tanks can be watched to monitor the filling process. For this purpose it is possible to display the time derivative (shown as V1 and V2) of the temperature of the individual tanks on the temperature controller as it can be seen in Figure 42.

Figure 42: Display units of the cryostat sensors. On the left is the temperature controller, in the middle are the display units for the level sensors and the display for the scattering chamber vacuum is on the right. To protect the electronics against radiation, all display units are located inside a lead shield.

At the beginning of the filling process the needle valve must be flushed with gaseous helium to remove impurities and residual gas that would otherwise freeze when the boiling temperature

of helium is reached. The valve would clog and filling of the He II tank would be impossible. To do so, the He I tank is filled with helium gas by means of the liquid helium transfer line. The tubes of the transfer line must cool down to helium temperature first, and it will output only helium gas into the Cryostat at the beginning of the filling process. The bypass valve of the control block of the feed pump will be opened, and the needle valve between the two helium tanks needs to be closed at the same time. The pressure in the He II tanks drops below 3 mbar. The bypass valve of the control block is then closed and the needle valve opened so that as much gaseous helium as possible flows through the needle valve from the He I tank into the He II tank and impurities such as nitrogen or hydrogen are removed. This process is repeated several times. Care must be taken, that the pressure in the He II tank does not exceed 1 bar. After it has been made sure that the complete He system, including the cell, are filled with gaseous helium, the two helium tanks can then be filled with liquid helium. For this purpose, it is important that both tanks are filled at the same time. The derivative that can be displayed on the temperature controller helps to adjust the filling process so that both tanks are full at about the same time. During the filling process the feed pump must be switched on so that there is a slightly lower pressure in the He II tank. This ensures, that cold He gas will be sucked into the He II vessel and it will be cooled by the enthalpy of this gas. By means of the control block it is ensured, that the pressure in the He II vessel will remain at about 900 mbar. The filling process can be influenced by changing the overpressure in the helium storage vessel, the degree of opening of the needle valve and the under pressure in the He II tank.

As soon as the temperature has dropped below 10 K, the level sensor can be switched on. Since the level sensor sends a short heat pulse into the liquid helium during each measurement process, the sensor is normally operated in such a way that it scans the level only once every 5 minutes. However, this is not fast enough for the filling process. For this reason, the sensors of both tanks are switched to continuous readout using the connected display unit. When the filling process is completed, they should be switched back to the reduced sample and hold readout mode, otherwise the evaporation rate of the liquid helium will be increased measurably. When using the level sensor, it should be noted that it only works in helium at atmospheric pressure or in the superfluid phase. The pressure in the He II tank must therefore not be set too low, or the sensor will display pure nonsense.

As soon as a sufficient level of liquid is reached in both tanks, the temperature in the He II tank can be reduced. The needle valve is closed, and the pumping speed of the feed pump is increased by opening the control block step by step. The corresponding temperature curve of the He II tank is displayed in Figure 43. At ① the boiling temperature of helium at atmospheric pressure is reached so that a liquid level can form. For a few hours, the temperature is somewhat unsteady, as the control valve of the feed pump must be adapted to the new situation and the cryostat including the heat shields need some time to freeze. In principle, it would be possible to reduce the temperature directly, but since it is recommended to wait until the temperature is stable before starting the experiment, this would only lead to unnecessary helium losses. The most important steps of the cooling procedure are briefly summarized in Table 3.

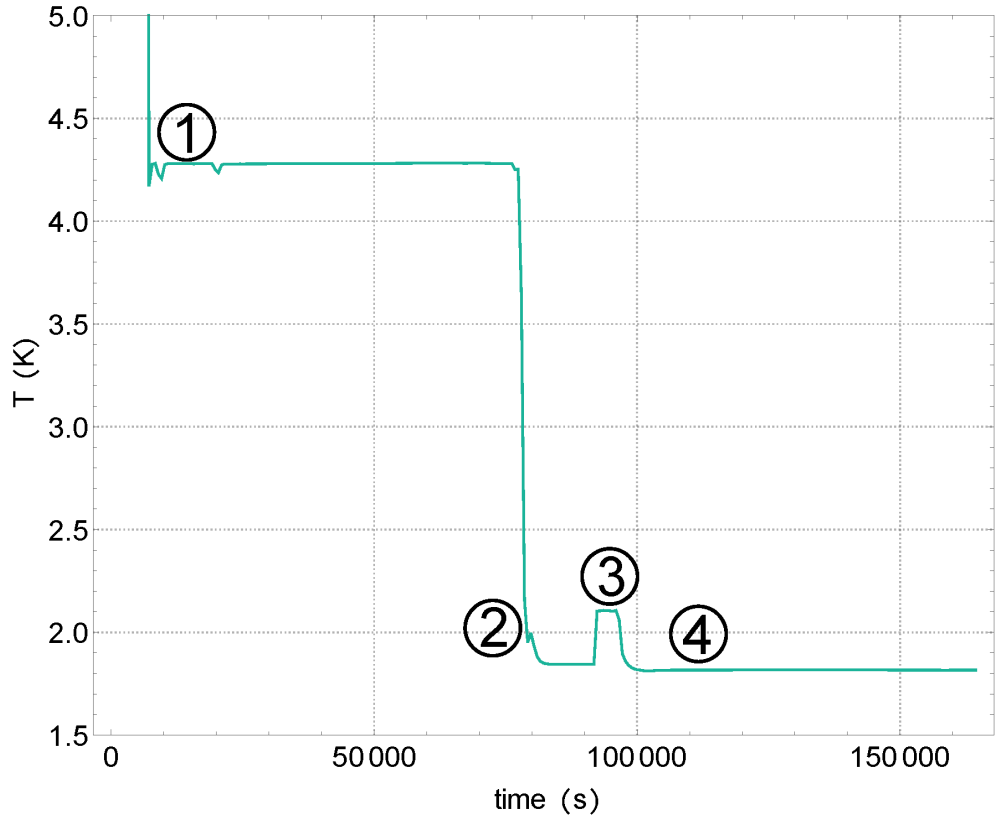

Figure 43: Temperature curve of the He II tank during the cooling procedure. ① A liquid level is formed in the tank. ② Phase transition to the superfluid phase. ③ The needle valve is opened to possibly increase the time period until the tank needs to be refilled. ④ Stable temperature of about 1.8 K reached.

Once the temperature is sufficiently stable, the pressure of the vapor above the liquid inside the He II tank can be decreased to reduce the temperature of the liquid helium. At ② the lambda point at 2.1 K is finally reached so that the phase transition into the superfluid phase takes place. The length of time in which a measurement can be performed without interruption is determined by the evaporation rate of the liquid helium in the He II vessel. In order to extend this period, the needle valve is slightly opened again at ③ to test whether the operating period of the cryostat can be increased in this way. Consequently, there is a constant refill from the warmer He I tank to the He II tank. The control block of the feed pump must be adjusted accordingly. At ④ a stable temperature of 1.8 K is finally reached. The pressure above the liquid is roughly 10 mbar.

Table 3: Summary of the individual steps necessary for the cooling procedure of the helium cryostat. Particularly steps 4 and 5 must be executed very carefully.

1.	Vacuum	Creating good insulating vacuum to remove residual moisture from the super insulation foil.
2.	Pre-cooling	Pre-cooling of the helium tanks to liquid nitrogen temperature. Residual liquid nitrogen must be removed and the He system must be let warm up to 100 K.
3.	Attaching helium vessel	Connecting the helium transport vessel and the He I tank via the helium transfer line.
4.	Flushing	The needle valve between the two helium tanks must be flushed with gaseous helium by opening and closing the needle valve and the bypass valve of the feed pump in a predefined order.
5.	Filling	Both helium tanks must be filled simultaneously. The pressure in both tanks must be observed and adjusted carefully.
6.	Cooling to 1.8 K	The temperature of the He II tank can be reduced. A pressure of 10 mbar corresponds to a temperature of 1.8 K.

In order to measure the operating duration of the cryostat system without the influence of the electron beam, the tanks were filled, and the filling level was recorded. The needle valve between the two helium tanks was closed in one measurement and afterwards slightly opened for a second measurement in order to determine the period of time during which helium was present in the He II tank.

First the helium loss with closed needle valve is examined. Figure 44 shows the temperature in the He II tank. During the experiment, this temperature should be as constant as possible to avoid density fluctuations. As it can be seen, equilibrium is quickly established, and the temperature line remains constant. Figure 45 shows the filling level in the He I tank. As expected, the curve is simply linearly falling due to the constant heat input from outside. The helium level in the He II tank is shown in Figure 46. Here again, the trend is quite linear. Most of the heat radiation is intercepted by the He I heat shield, as it was shown during the cold tests with liquid nitrogen. The loss in the He II tank is therefore mainly due to the cooling by the feed pump. The helium loss of the two tanks and the possible operating period are summarized in Table 4.

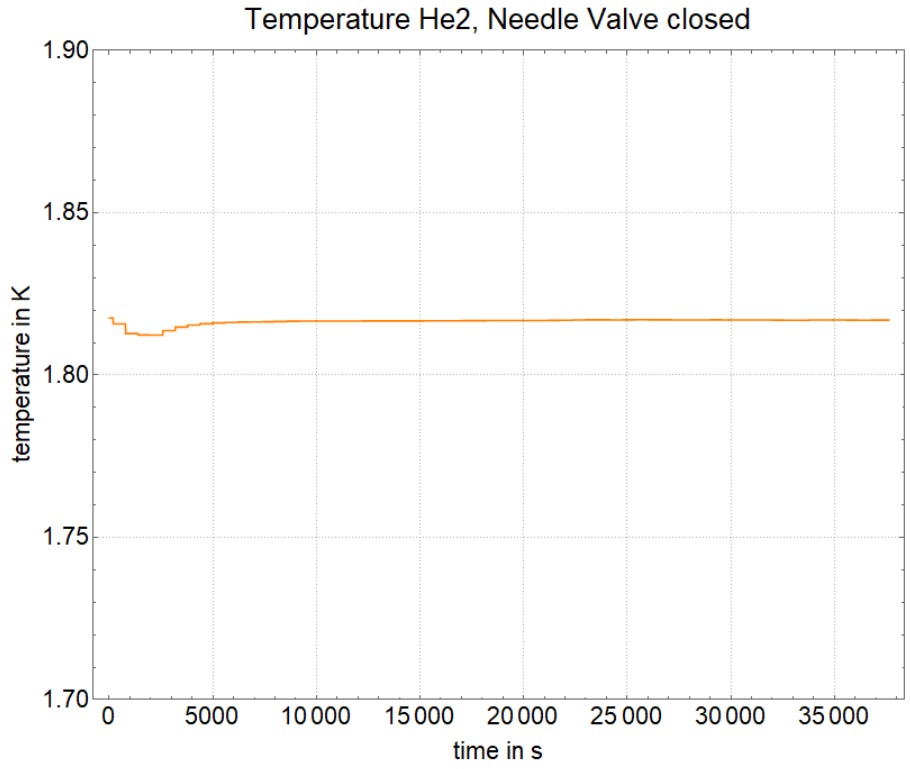

Figure 44: Temperature curve in the He II tank while the tank is being drained without an electron beam. Due to the constant temperature of the surrounding nitrogen shield and the constant pumping rate of the feed pump, the temperature is constant after the settling process.

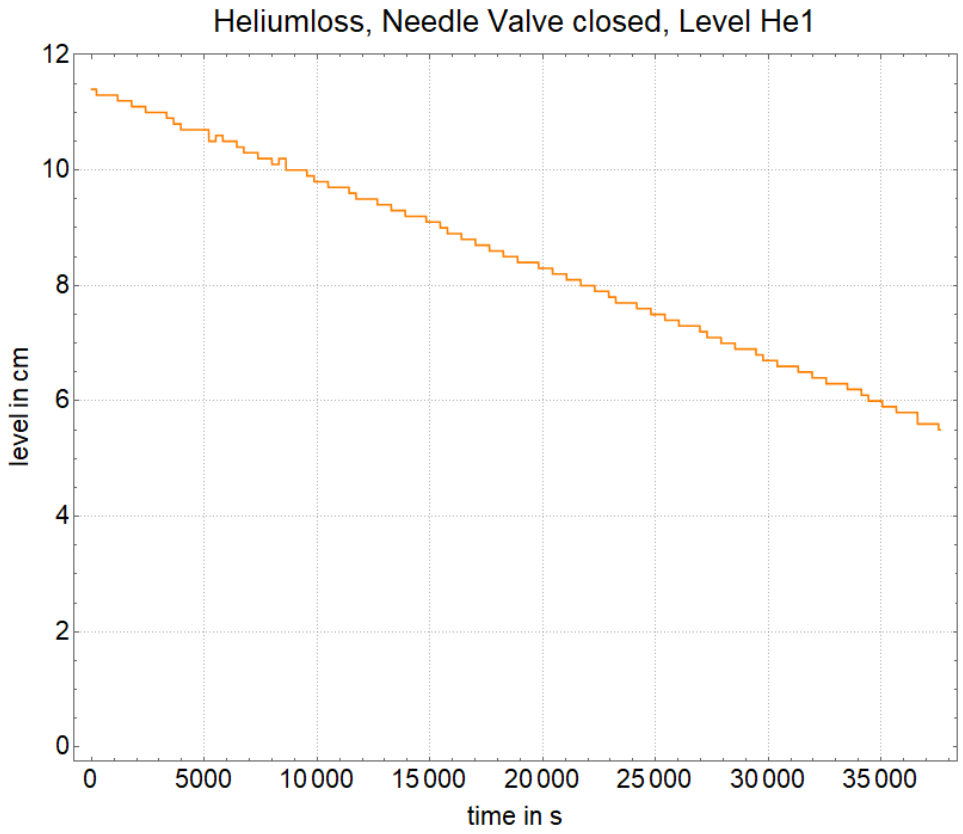

Figure 45: Level curve of the He I tank with closed needle valve without electron beam. The helium loss is at a constant rate of 0.56 cm per hour.

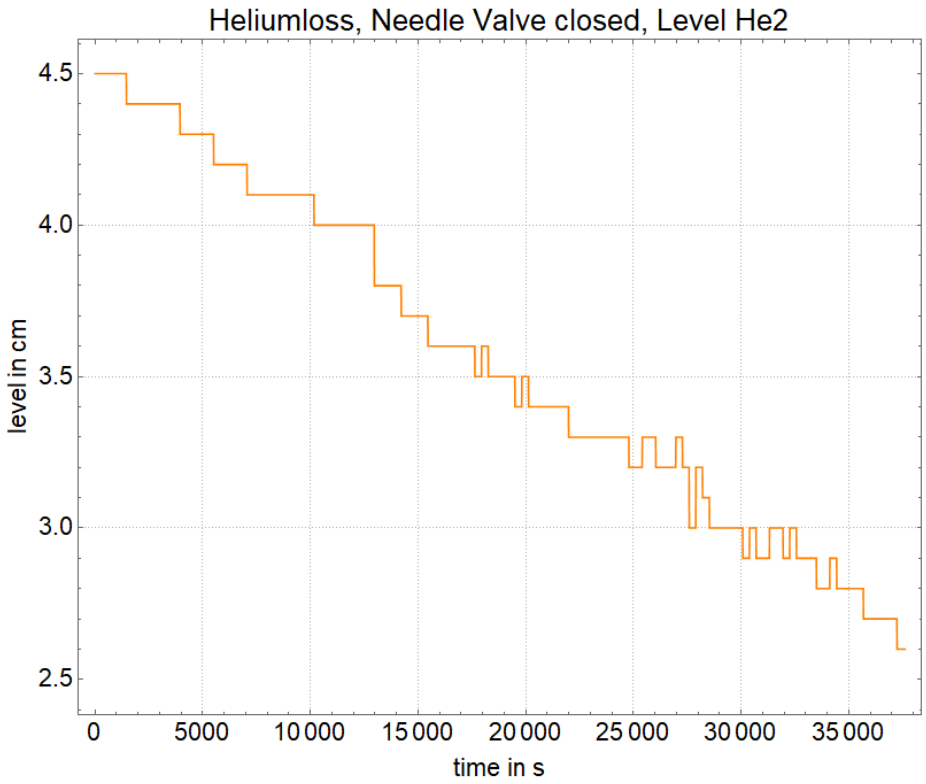

Figure 46: Level curve of the He II tank with closed needle valve without electron beam. The helium loss is constant at 0.18 cm per hour.

Next, the helium loss was measured when the needle valve is slightly opened and thus a continuous drip of helium from the He I tank into the He II tank occurs. It is particularly important to ensure that the amount of helium that drips must be smaller than the amount that evaporates in the He II tank to prevent an overflow of the tank. There are two interesting components to consider. First, the operating time of the cryostat should be as long as possible in order to interrupt the experiment as little as possible. For this purpose, the time in which the He II tank is filled, and the temperature remains constant is important. Next, the helium consumption of the entire system should be kept as low as possible. Here the sum of the consumption of both tanks is interesting. Figure 47 shows the temperature curve in the He II tank with slightly opened needle valve. It can be seen that the temperature first remains constant after the settling process, but then suddenly drops from 1.82 K to 1.77 K, which corresponds to a density change below 0.03 % [13]. This is due to the fact that the He I tank is empty at some point, so that no more helium drips into the He II tank, which also means that the additional heat input from the 4.2 K warm helium disappears. Figure 48 shows the corresponding curve of the He I level. Figure 49 shows the filling level of the He II tank. As soon as the He I tank is empty, the level drops faster, because no additional helium is added. Table 4 summarizes the corresponding values.

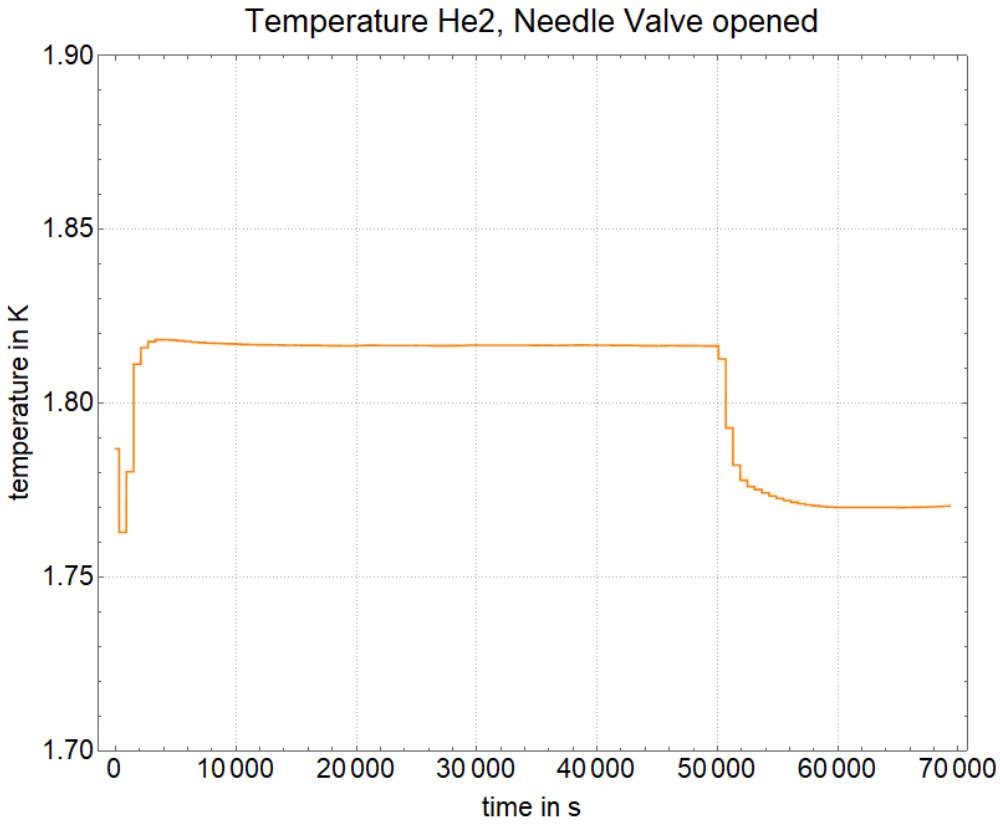

Figure 47: Temperature of the He II tank while the cryostat is drained without electron beam, with the needle valve slightly open. The temperature is constant after the settling process and then drops suddenly from 1.82 K to 1.77 K as soon as no more helium drips from the He I tank.

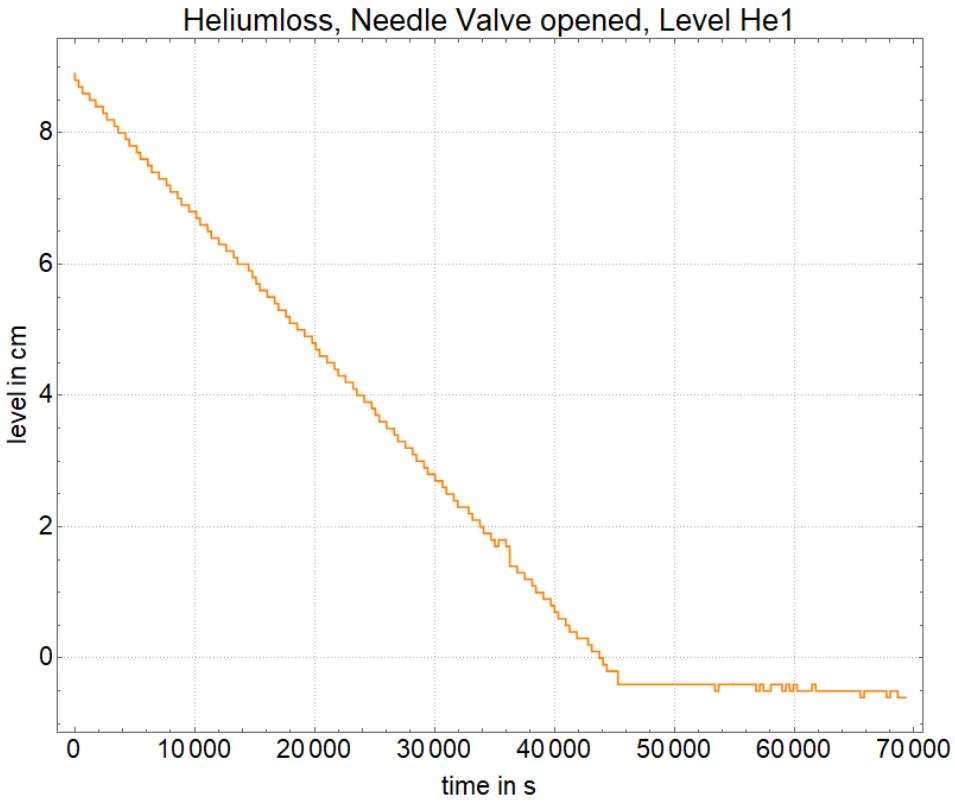

Figure 48: Level curve of the He I tank with opened needle valve without electron beam. The helium loss is constant at 0.72 cm per hour.

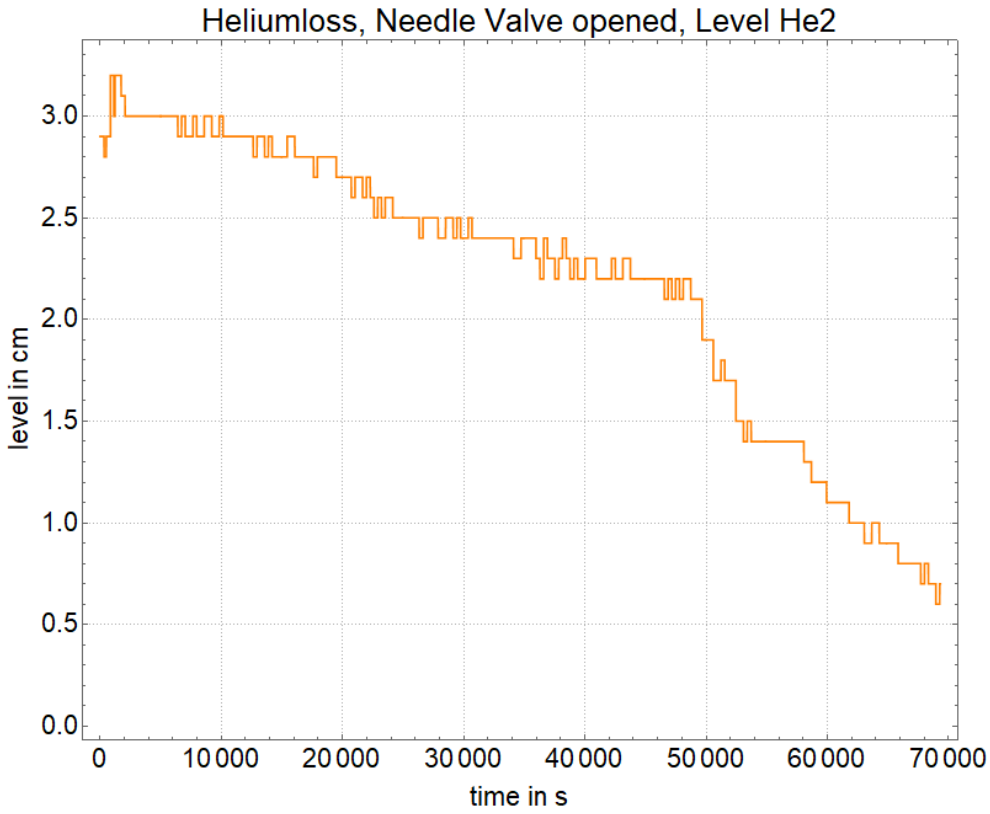

Figure 49: Level curve of the He II tank with opened needle valve without electron beam. The helium loss is constant at 0.07 cm per hour until the He I tank is empty. As soon as the He I tank is empty, the helium loss increases to 0.24 cm per hour.

The comparison of the values in Table 4 shows the differences between operating the cryostat with the needle valve opened or closed. To determine the time until the tank is empty, it was assumed that the tank was filled to its maximum capacity. Especially for the He II tank this is not very realistic, because there is always a helium loss during the cooling below the boiling temperature and the tank can therefore never be completely filled. However, this is not relevant to compare the two operating modes.

Table 4: Helium loss of the individual tanks without electron beam. For the "time until empty" column it was assumed that the tanks are filled to full capacity. Especially for the He II tank this is not realistic. The extrapolation of the operating period for the He II tank, especially when the He I tank is empty, should be treated with caution. The section of the opened needle valve is divided in two rows: The measurement starts with the first row when there is liquid in both He tanks. After the He I tank is emptied out, the changed behavior of the He II tank is noted in the last row.

	Loss He I tank per hour	**Time until He I tank empty**	**Loss He II tank per hour**	**Time until He II tank empty**	**Helium Loss in 30 hours**
Needle valve closed	0.51 cm ≙ 0.42 liter	38.1 hours	0.18 cm ≙ 0.11 liter	50.9 hours	15.9 liter
Needle valve opened	0.72 cm ≙ 0.54 liter	29.6 hours	0.07 cm ≙ 0.04 liter	29.6 hours	17.4 liter
	empty	empty	0.24 cm ≙ 0.14 liter	(31.5 hours)	(4.2 liter)

It is shown that it is in principle possible to extend the operating period of the cryostat by opening the needle valve slightly, but for the cost of the increase of the overall helium loss. Furthermore, the heat shields of the 4 K tank heat up over time, which could reduce the stability of the He II tank. It therefore seems to be more practical to operate the cryostat with the needle valve closed, as in this case longer reliably stable operation with lower helium loss is possible. An exception could be when experiments are performed at very high beam currents with high electron energy, where the heat input by the electron beam into the target, and thus the helium loss in the He II tank, is particularly large and thus, the He II tank runs empty before the He I tank.

6. Commissioning Experiment

To test whether the target would behave as expected in the experiment, a commissioning experiment was conducted. Afterwards the data was processed and evaluated.

6.1. Experiment

Measurements were performed at a beam energy of 42.5 MeV and a scattering angle of 75°. This corresponds to a squared momentum transfer of 0.047 fm^{-2}.

First, measurements without helium were performed to investigate the possibilities of geometrical beam adjustments. Usually a movable target ladder with a fluorescent target in the center of the scattering chamber is used to focus the electron beam on the target position. However, when using the helium target, it is not possible to place the luminous target at the exact target position. Instead, the luminous target is located a few cm in front of the target position as described in 4.2.1. To adjust the electron beam correctly to the helium cell, a Mylar foil was fixed on the target cell at room temperature. Then the electron beam was adjusted to different positions of the crosshair of the luminous target and the Mylar foil was burned through in a controlled way. Figure 50 shows on the left side the target cell to which a piece of Mylar foil was attached. On the right-hand side, the foil after exposure to the electron beam is shown. In this way it was possible to assign spots on the luminous target to beam positions on the helium target. However, care must be taken not to raise the beam current higher than necessary as the target is designed to not dissipate heat if there is no cold liquid in the target cell. The measurements were performed with a current such that approximately 10 nA was displayed on the Faraday cup. As it can be seen, the burn marks on the Mylar film are clearly shifted upwards. In fact, there were a few problems with the adjustment of the electron beam due to an inaccurate alignment of the beam guiding elements and the target. The origin could not be found out exactly during the measurement. Meanwhile the alignment of the beam guiding elements has been carried out again with the help of the geodetics. In future experiments this problem should be solved. It also turned out that the windows of the target cell are too narrow and some of the planned scattering angles cannot be reached at all. An improved target cell is described in section 7.

Figure 50: Left: Target cell with Mylar foil, taken through the opening of the heat shield. Right: Mylar foil with burn marks after electron beam exposure. The oval shape of the burn marks results from the rotation of the target according to the scattering angle. One can see that the alignment could be performed but it was not ideal.

Normally there is as little material as possible in the scattering chamber of the QCLAM spectrometer to avoid secondary scattering of the electrons on other things than the actual target. In the helium scattering chamber, however, there are several layers of heat shields inside the scattering chamber and the target cell itself also consists of a lot of material. A careful adjustment of the high energy scraper system was necessary [44]. Without using the scraper, the background in the detector system of the spectrometer was too large and the system was permanently overloaded, but the use of the scraper system made the measurements possible. The ideal scraper setting was found to be +0.2 mm open on the left and +0.1 mm on the right-hand side. The halo scraper was not ready to use at the time of the experiment but would probably provide a great advantage for future measurements. After that, several measurements with different dipole and quadrupole settings were performed, so that the whole focal plane was covered with elastic aluminum lines due to the aluminum windows. This is necessary for the later evaluation of the spectra and the efficiency calibration of the detector system. Unfortunately, during the measurement some areas of the detector system were malfunctioning, so that the efficiency of the drift chamber was quite different for the sections of the focal plane. Furthermore, certain parts of the focal plane were not usable at all.

Table 5: Values of the used dipole and quadrupole current settings of the QCLAM magnets for a beam energy of 42.5 MeV. The whole focal plane is covered with the shifted elastic lines.

Dipole current in A	56	57	59	61	63	65	67	69	70	71
Quadrupole current in A	72.8	74.1	76.7	79.3	81.9	84.5	87.1	89.7	91.0	92.3

Afterwards the cryostat could be filled with helium as described in chapter 5.3 and the measurements on helium could be started. The measurement with helium lasted 8 days in total. The helium tanks had to be refilled about every 20 hours. However, most of the time the tanks were not filled in a fixed pattern, but the filling times were adjusted so that the measuring time could be used optimally. For example, the tanks were filled when the accelerator needed a break due to oscillations in the cryostats. The temperature remained extremely stable throughout the measurement and the cryostat itself caused absolutely no problems. Figure 51 shows a section of the helium temperature curve. The temperature fluctuations were less than 0.1 K even when the beam current fluctuated significantly. The density fluctuation thus stays below 0.1 % [13] which causes a negligibly small impact on the cross section measurements.

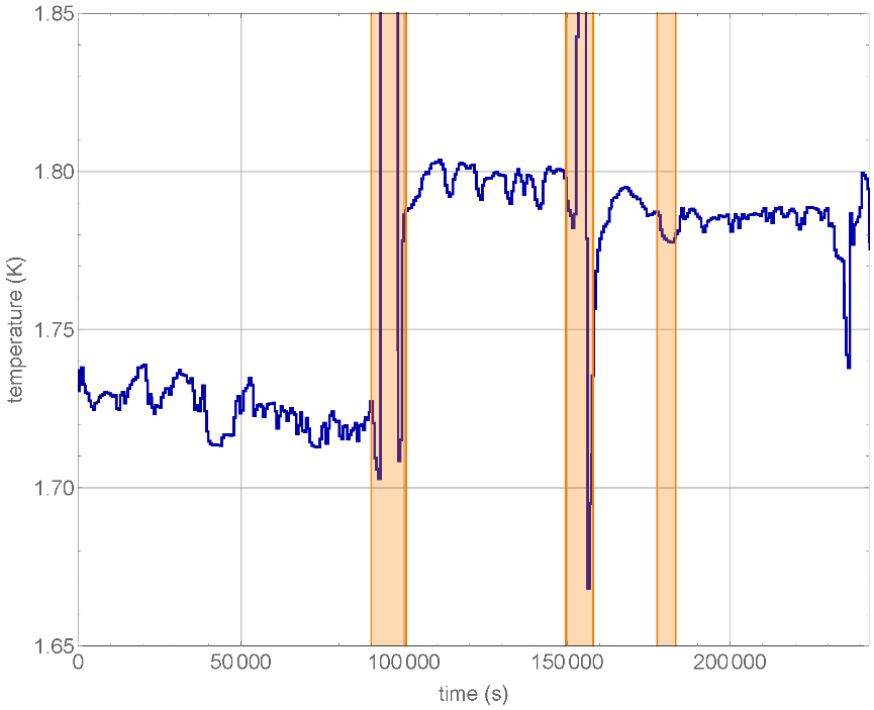

Figure 51: Section of the temperature curve during the experiment. Orange bars represent times during which the system was refilled. During these periods, no electron beam was present.

The elastic line of helium and the excited state were measured alternately. Some problems were caused by the fact that the behavior of the QCLAM spectrometer was largely unknown, since it had not been used for measurements for a long time and the data acquisition software is completely new [31]. For example, it was found that the offset of the measured current at the Faraday Cup suddenly changes when the magnetic field at the spectrometer is changed. The reason for this is still under investigation. To work around this problem, a 5-minute current measurement without electron beam was performed between all measurements for which the magnetic field had to be adjusted to determine the new offset.

Several times the target was drained completely and measured further until the temperature of the target had risen to about 30 K. In this way a background measurement for the empty target could be performed.

6.2. Data Analysis

For the data analysis several steps were necessary to prepare the measured data. The data acquisition program of the QCLAM spectrometer [31] as well as Wolfram Mathematica 12 [45] were used to perform the corrections and to evaluate the data.

6.2.1. Corrections due to the curved focal plane

In the first step of the data analysis corrections are made to improve the energy resolution. There are several successful methods for this purpose, in this case the technique based on the method of [46] is used.

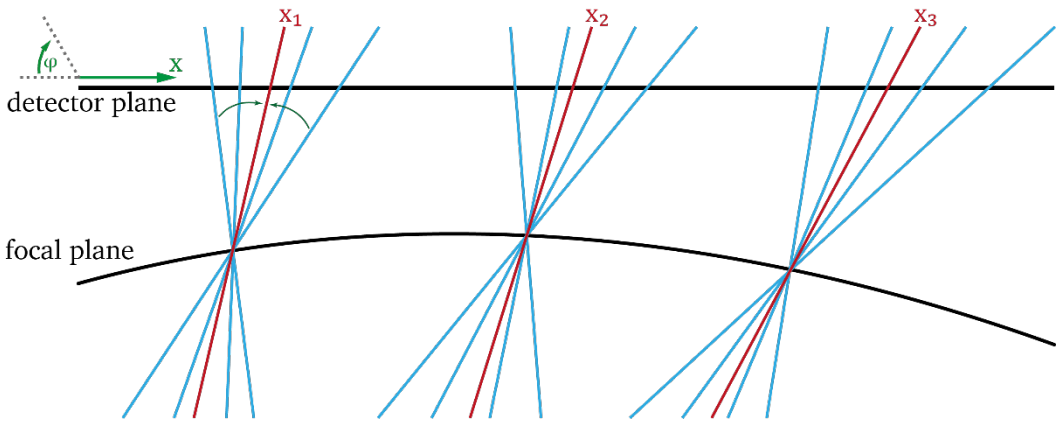

Figure 52: Illustration of the correlation between detector coordinates and focal plane. Electrons with 3 different energies are focused on 3 points of the focal plane. In the detector plane they arrive at different points at different angles.

In the QCLAM spectrometer the focal plane is curved and is also not contained in the detector plane. This means that in the ideal case, all electrons with the same momentum strike the same point in the focal plane, but as shown in Figure 52, they hit the detector at different points and at different angles. This means that electrons with the same momentum are distributed over a broad area of the detector plane. If one would simply transfer the x-position in the detector system into energy values without further correction, the resulting spectrum would be heavily smeared, and the energy resolution would be correspondingly poor. Therefore, the detector system of the spectrometer consists of several layers, so that not only the position but also the angle of the incident electrons can be determined. In the next step, the measured dispersive coordinates x and the dispersive angle φ are entered into an x-φ diagram as shown in Figure 53.

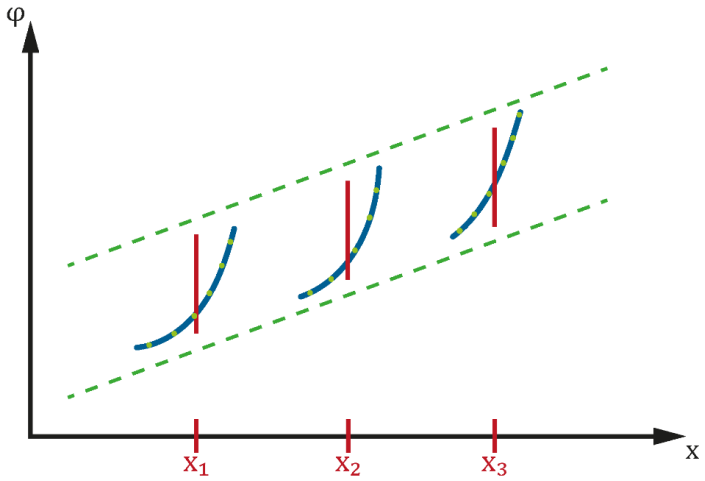

Figure 53: The locations in the detector plane measured according to Figure 52 are entered in an x-φ diagram. For each momentum focused in the focal plane, a banana-shaped line is obtained. Function (6.1) is used to map the 2-dimensional coordinates to the one-dimensional focal plane to produce a spectrum with good energy resolution.

The function

$$f(x,\varphi) = a \cdot x + b \cdot \varphi + c \cdot x \cdot \varphi + d \cdot x^2 + \cdots \tag{6.1}$$

is now simultaneously fitted to all banana shaped x-φ-curves. The 2-dimensional x-φ coordinates are mapped to the 1-dimensional focal plane coordinates. The bananas are effectively bent straight. Alternatively, it is also possible to fit all bananas individually with the function

$$f(x, \varphi) = a \cdot x + b \cdot \varphi \tag{6.2}$$

and, in a second step, to interpolate between them to map the whole focal plane between the measured bananas. Since in the described experiment only the elastic line was available, there were never several lines in the spectrum at the same time. Instead, the elastic line was shifted over the whole detector system using different magnetic field settings shown in Table 5, so that measured values are available for the entire focal width. Therefore, the two-step-method was performed.

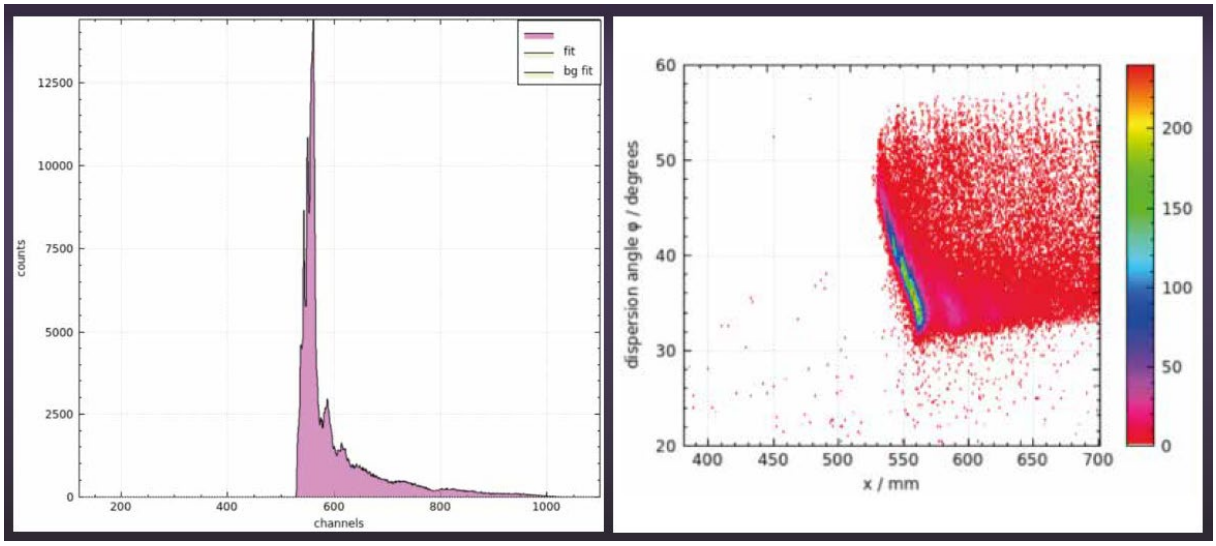

Figure 54: The measured values are displayed by the data acquisition software. Tracks through the 3 drift chamber levels are reconstructed automatically. Left: Uncorrected measured spectrum. Right: Display of the assigned x-φ coordinates.

The x-φ coordinates can be displayed directly in the data acquisition software of the QCLAM spectrometer [31]. Figure 54 shows an uncorrected measured spectrum with the corresponding x-φ values. Points can be marked on the lines, which can then be exported as shown in Figure 55.

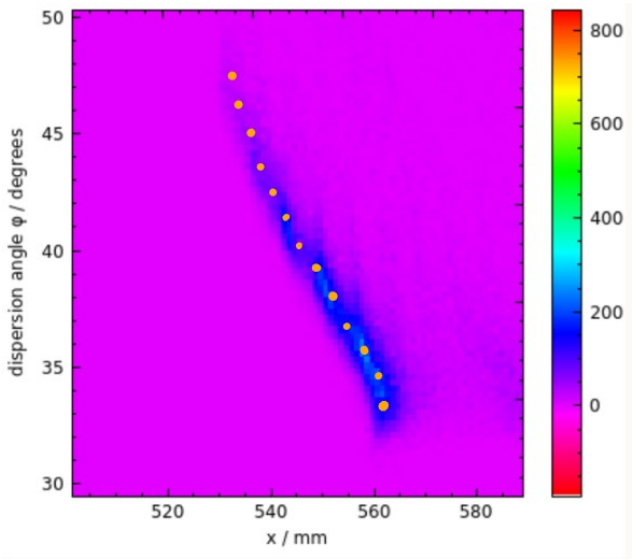

Figure 55: The x-Phi coordinates can be marked within the data acquisition program. The coordinate pairs are then exported and can be processed for the execution of the banana-shape correction.

Functions of the form of equation (6.3) are then adapted to these values

$$x(\varphi) = a_0 + a_1(\varphi - \varphi_0)^2. \tag{6.3}$$

To perform the interpolation for the entire focal plane, all functions are taken at a fixed value for $\varphi_c = 52°$ and the functions $a_1(x)$, $a_0(x)$ and $\varphi_0(x)$ are plotted and polynomials are fitted to these functions.

These polynomials can then be inserted into the function

$$f(x, \varphi) = a_0(x) - a_1(x) \cdot \left(\varphi - \left(\varphi_0(x)\right)\right)^2. \tag{6.4}$$

Finally, this function is imported back into the data readout software and the measured spectra are corrected and printed. Figure 56 shows the spectrum from Figure 54 with applied correction. This makes the shape of the elastic line much narrower and more defined.

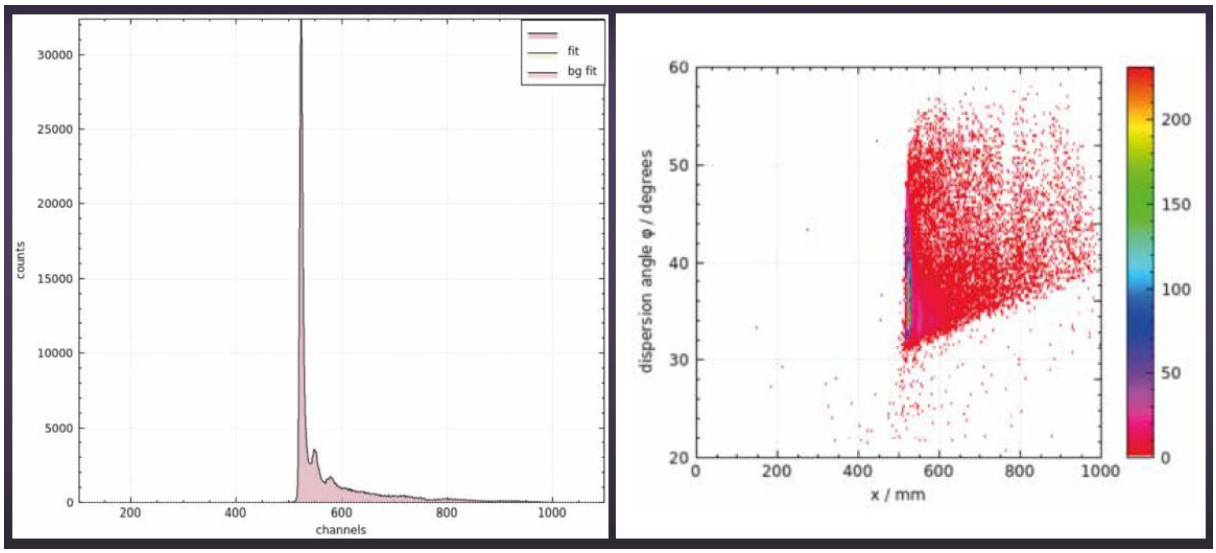

Figure 56: spectrum after performing the banana-shape correction. The 2-dimensional x-ϕ-plot shows a vertical line. The elastic line visible in the spectrum is refined.

In the meantime, the QCLAM software has been significantly improved. Manual processing of the data in this way is no longer necessary [31].

6.2.2. Reduction of possible geometric acceptance of the spectrometer

In the next step the possible geometric acceptance was limited by software cuts. As shown in Figure 57, it is possible to perform this restriction directly in the data acquisition software. In this way, the measured statistics are reduced, but events that occurred because electrons scattered at the edges of the heat shields could be removed in this way.

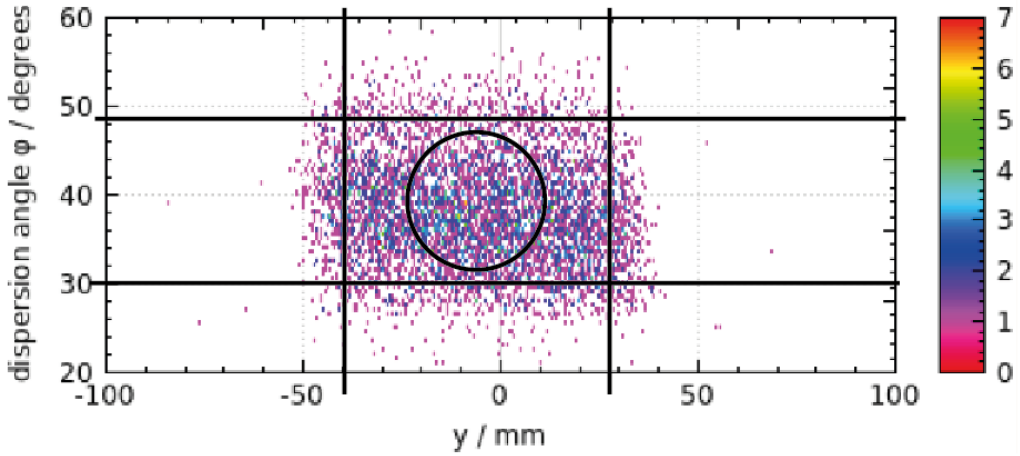

Figure 57: Representation of the possibility to perform software restrictions of the geometric acceptance for the QCLAM spectrometer inside the data acquisition software. The position y stands for the non-dispersive coordinate of the spectrometer.

Figure 58 shows the same spectrum of the empty target cell two times. On the left-hand side, the spectrum without restriction of the geometric acceptance of the spectrometer is shown. To the right of the elastic line of aluminum there are additional bumps. These peaks are there because electrons can scatter at the edges of the heat shields and lose additional energy. For verification, the same measurement was made at room temperature with partly removed heat

shields. The number of additional bumps corresponded exactly to the number of heat shield layers installed inside the scattering chamber. Since the electrons scattered at the edges of the heat shields reach the spectrometer at a different angle and from a different position than the electrons scattered exclusively at the target in the center of the scattering chamber, contributions of these electrons can be removed by limiting the geometric acceptance of the spectrometer. On the left in Figure 58 the same spectrum is shown, but the solid angle was restricted. As it can be seen, the number of events in the elastic line has been reduced, but the peaks next to the elastic line have completely disappeared. This is especially important because the elastic line of helium appears exactly at the position where the most left heat shield peak is located. A systematic variation of different combinations for restrictions of the y and φ-values was performed. Limiting the y-values between -30 mm and 20 mm, and the φ-values to 30° to 38° has resulted in the best compromise between a limited count rate and prevention of unwanted scattering events.

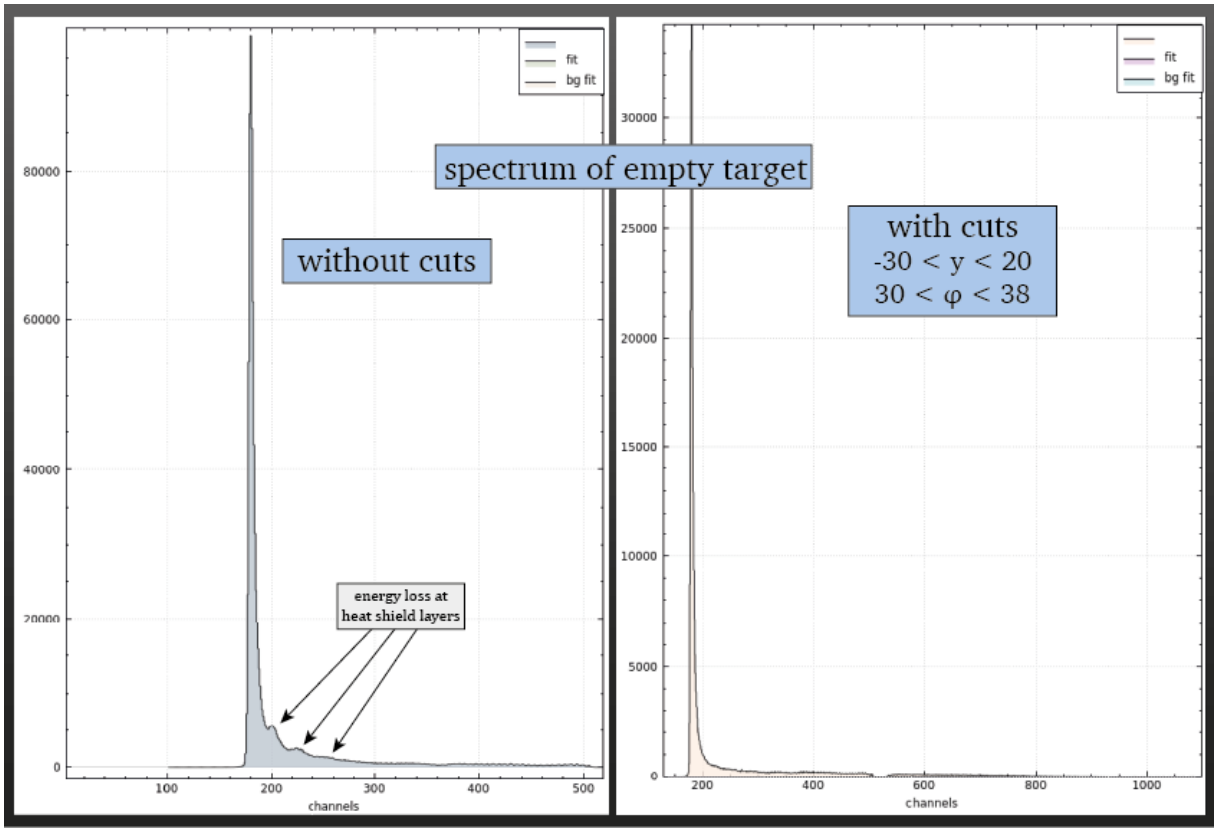

Figure 58: Spectrum of the empty target cell before (left) and after (right) the application of the software-sided restriction of the geometric acceptance of the spectrometer. By limiting the possible solid angle, scattering events at the heat shield layers of the helium target could be suppressed.

6.2.3. Energy calibration

To remove the influence of the different efficiencies of the single drift chamber wires, spectra in the excited region of aluminum at different magnetic field settings were taken and normalized. Then, it was averaged over all spectra. Possible small influences of structural behavior are eliminated in this way. Finally, efficiency values for each individual channel were generated. These determined values were then applied to the measured helium spectrum which was prepared according to chapter 6.2.1. and 6.2.2. The result is shown in Figure 59. During the measurement there were some channels in the middle of the spectrum that were completely

broken. These channels will, of course, not be able to display signals even after applying the efficiency calibration.

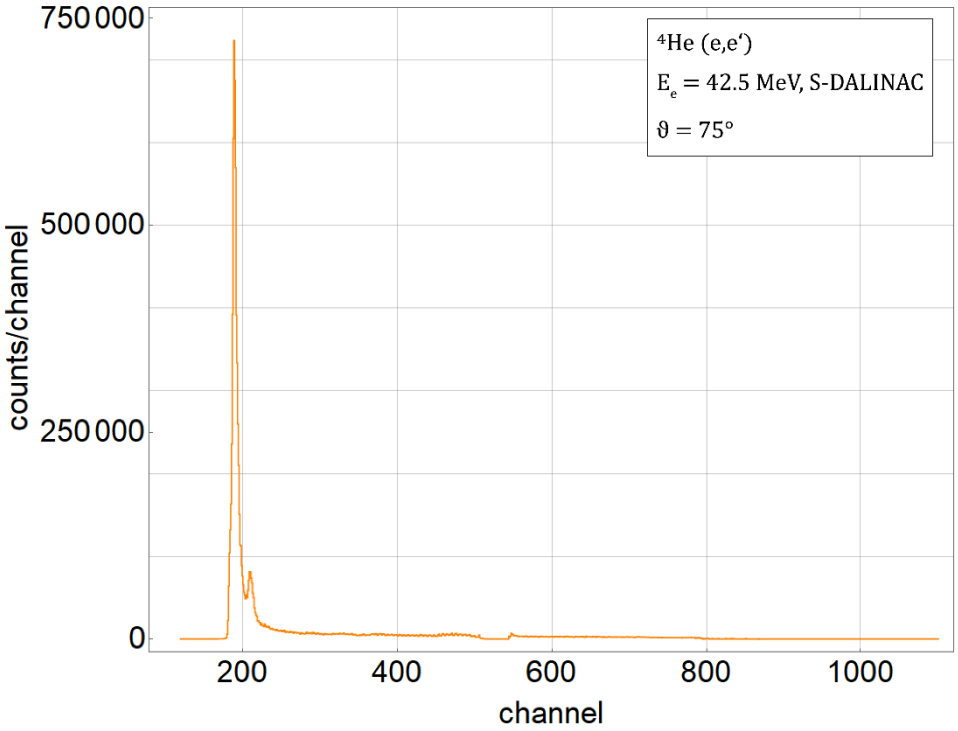

Figure 59: Spectrum of elastic lines of helium and aluminum with applied efficiency correction.

For the energy calibration of the spectra, the fact that electrons being scattered at atomic nuclei cause a recoil has been used. This means that they transfer energy to the atomic nucleus even if they scatter elastically. The advantage in this case is that the amount of energy loss depends only on the material of the nucleus off which the electrons are scattered. The number of nuclei present in the target is not relevant. This is important, because with the performed measurement the target thickness, and thus the number of scattering particles per area, should be determined. The recoil energy that the electrons transfer to the nucleus is calculated by

$$E' = \frac{E_i}{1 + \frac{2E_i}{Mc^2}\sin^2\frac{\theta}{2}} \tag{6.5}$$

where *E'* is the remaining energy of the electrons after the scattering process. E_i is the energy of the initial electron beam, M is the mass of the target nucleus and θ is the scattering angle. For aluminum $E'_{\mathrm{Al}} = 42.132$ MeV, for helium $E'_{\mathrm{He}} = 41.836$ MeV so the difference between them is $E'_{\mathrm{Al}} - E'_{\mathrm{He}} = 0.297$ MeV. To get the positions of the peaks in Figure 59 a piecewise defined function consisting of an ascending Gaussian, a descending Gaussian and a hyperbola is adapted to the peaks [47]

$$f(x) = \begin{cases} A \exp\left(-\frac{(x - x_0)^2}{2\,\sigma_1^2}\right) & | \; x < x_0 \\ A \exp\left(-\frac{(x - x_0)^2}{2\,\sigma_2^2}\right) & | \; x_0 < x < x_0 + \eta\,\sigma_2 \\ \frac{A_1}{(B + x - x_0)^\gamma} & | \; x > x_0 + \eta\,\sigma_2. \end{cases} \tag{6.6}$$

As a result, each measured channel has a width of 15 keV. For the energy calibration of the spectrum, it is not ideal that both states that were used for calibration are rather close to one another in the low energy range of the spectrum. The calibration is extrapolated into the range of higher excitation energy over a relatively large range, so that larger uncertainties in the range of high excitation energies must be assumed. For further evaluation of the data, however, only the elastic lines are used, and the assigned energy does not influence the results. Therefore, no problems arise in this case.

After applying all corrections and calibrations, the spectrum shown in Figure 60 was obtained.

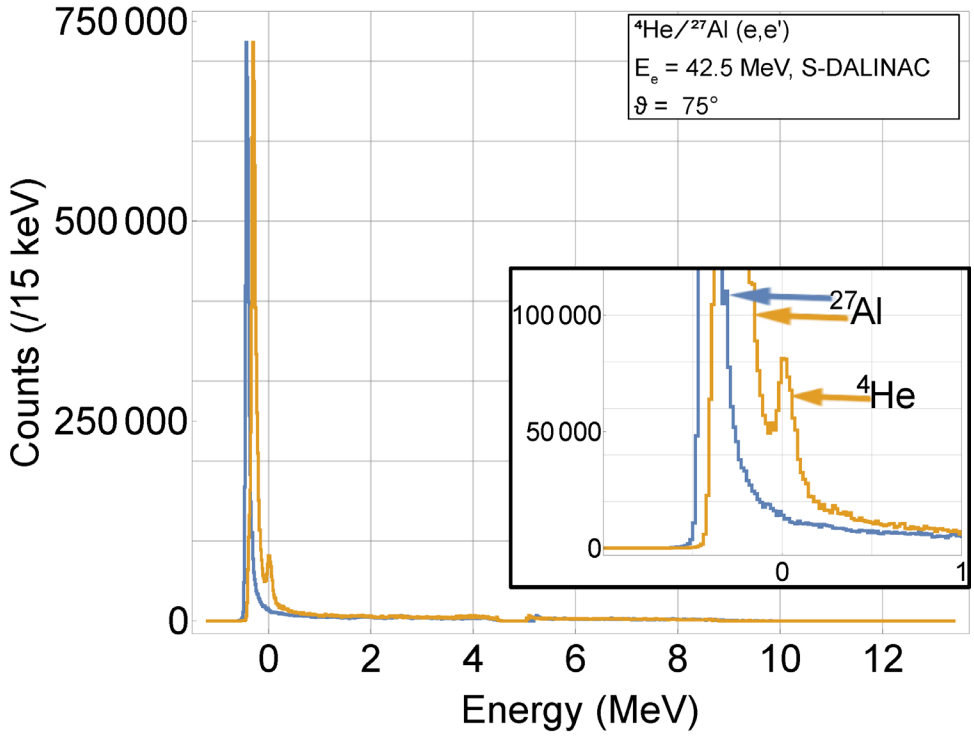

Figure 60: Measured spectrum in the range of elastic scattering. In blue: Background spectrum of the empty target cell. In yellow: Spectrum of the capsule filled with helium. The background spectrum has been normalized to the helium measurement. Taken from [19].

The inset provides an expanded view around the elastic scattering peak. The blue line represents the background spectrum of the empty target container, in order to determine the contribution from scattering off the aluminum windows. The yellow line shows the spectrum of the capsule filled with helium. The elastic line from aluminum was normalized to the helium measurement in the figure by comparison of the peak areas of the two aluminum lines in the two spectra. This allowed the subtraction of the scattering intensity originating from the aluminum window. The elastic line of aluminum in the helium spectrum is slightly shifted to lower momentum due to the additional energy loss of the electrons in the liquid helium.

6.3. Results

The cryostat proved to be very functional during the whole experiment. Especially the temperature stability was excellent with a temperature fluctuation below 0.1 K. The next step is to check whether superfluid helium as target material behaves as expected. It must be verified that there were indeed no bubbles and that the target density can be determined as expected. If this is the case, in future experiments an underestimation of the experimental cross sections due to an overestimation of the target thickness caused by bubble formation will be excluded. Therefore, the target thickness of the superfluid helium material is determined from the measured data and compared with the manufacturer's specifications for the geometric target extension. For this purpose, the peak areas of the aluminum line and the helium line from Figure 60 are compared. The ratio of the two areas must be the same as the ratio of the areal mass density of the aluminum windows and the helium material. The thickness of the aluminum windows can be measured to an accuracy of 0.01 mm.

It must be considered that the target was rotated by an angle θ_{target} with respect to the beam axis. Due to this geometric adaption, the electrons had to travel a longer distance $d_{\text{eff}} = d/\cos(\theta_{\text{target}})$ within the target than its geometrical thickness d.

The integrated areas A of the peaks are proportional to the corresponding scattering cross sections

$$A \propto Q_0 \cdot \frac{d\sigma}{d\Omega} \cdot n = Q_0 \cdot \frac{d\sigma}{d\Omega} \cdot \frac{\rho \cdot d_{\text{eff}}}{\mu}. \tag{6.7}$$

Q_0 is the integrated collected charge and n the number of scattering particles per area while μ denotes the mass of a single atom. The cross sections

$$\frac{d\sigma}{d\Omega} = \left(\frac{d\sigma}{d\Omega}\right)_{\text{Mott}} \cdot \frac{1}{\eta} \cdot |F(q)|^2 \tag{6.8}$$

for the elastic scattering of aluminum or helium can be calculated using the Mott scattering formula

$$\left(\frac{d\sigma}{d\Omega}\right)_{\text{Mott}} = \left(\frac{Z^2\alpha^2}{4E^2 \sin^4\left(\frac{\theta}{2}\right)}\right) \cdot \left(\cos^2\frac{\theta}{2}\right). \tag{6.9}$$

Due to the low mass number, the recoil

$$\eta = 1 + \frac{2E}{M \sin^2\left(\frac{\theta}{2}\right)} \tag{6.10}$$

must be considered. The elastic form factors $|F(q)|^2$ in the range of the given momentum transfer for this experiment are sufficiently close to 1 [48] for the desired precision and thus can be neglected.

The actual helium thickness $d_{\text{He,exp}}$ can be extracted from the measured spectrum shown in Figure 60 by comparing the ratio of the peak areas of the helium and the aluminum lines with the ratio of the corresponding Mott cross sections

$$\frac{A_{\mathrm{He}}}{A_{\mathrm{Al}}} = \frac{\left(\frac{d\sigma}{d\Omega}\right)_{\mathrm{He}}}{\left(\frac{d\sigma}{d\Omega}\right)_{\mathrm{Al}}} \cdot \frac{\mu_{\mathrm{Al}}}{\rho_{\mathrm{Al}} \cdot d_{\mathrm{Al}}} \cdot \frac{\rho_{\mathrm{He}}}{\mu_{\mathrm{He}}} \cdot d_{\mathrm{He,exp}}. \tag{6.11}$$

Here, the thickness of the two aluminum windows is $d_{\mathrm{Al}} = (0.400 \pm 0.015)$ mm. A_{He} and A_{Al} are extracted from the spectra. To be able to separate the area under the helium peak from the elastic radiative tail of the aluminum line, the spectrum of the empty target measurement was normalized to the aluminum line by area comparison and subtracted from the helium measurement. The remaining count rate belongs to the elastic line of helium.

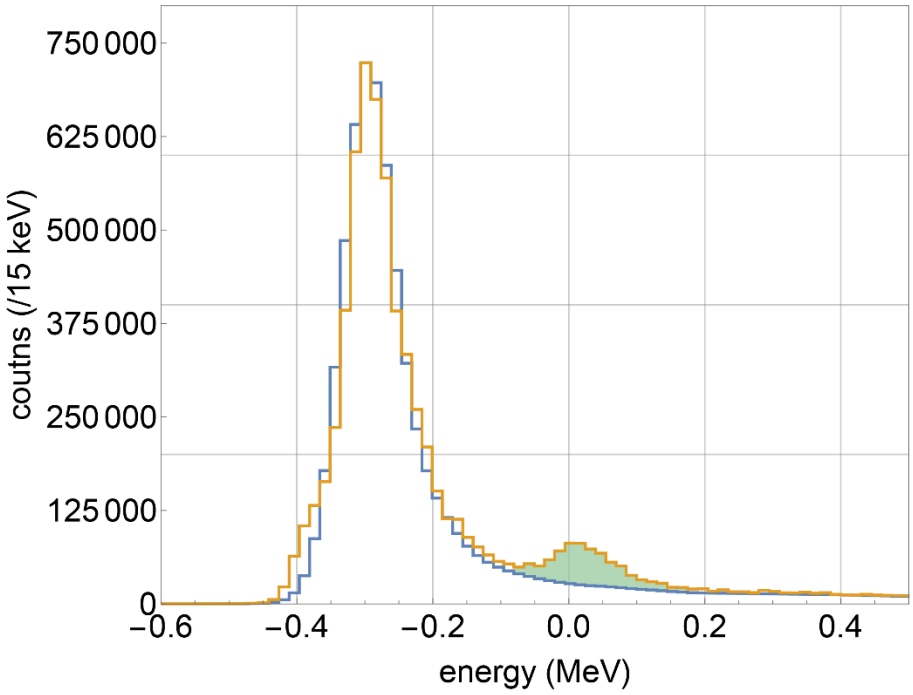

Figure 61: The empty target measurement was normalized to the spectrum of the target filled with helium by comparison of the areas of the aluminum lines. Then the two aluminum lines were pushed onto each other. After subtracting both spectra, the area below the helium line remains.

Table 6: Some specific characteristics of the experiments which are needed to fill equation (6.11). The given cross sections have been calculated according to (6.8).

Beam energy	E	42.5(5) MeV
Scattering angle	θ	75(2) °
Angle of target rotation	θ_{target}	37.5(10) °
Peak area helium	A_{He}	$5.02(3) \times 10^5$
Peak area aluminum	A_{Al}	$6.505(55) \times 10^6$
Cross section helium	$(d\sigma/d\Omega)_{\mathrm{He}}$	0.049(6) mb/sr
Cross section aluminum	$(d\sigma/d\Omega)_{\mathrm{Al}}$	2.2(3) mb/sr

Using the thickness of the aluminum windows, it is possible to calculate the ratio of the peak areas as a function of the target thickness d_{He} for the superfluid helium as it is shown in Figure 62. The orange horizontal line results from the measured peak areas. The uncertainty of the peak area ratio is dominated by the uncertainties of the model parameters optimized by the unfolding of the two elastic peaks, as it can be guessed from Figure 61. The experimental target thickness $d_{\mathrm{He,exp}}$ is derived from the intersection of the line representing the ratio of the peak areas with the black line, which comes from (6.11). The uncertainty is dominated by the unknown thickness of the indium sealing between the aluminum windows and the copper shell of the target cell.

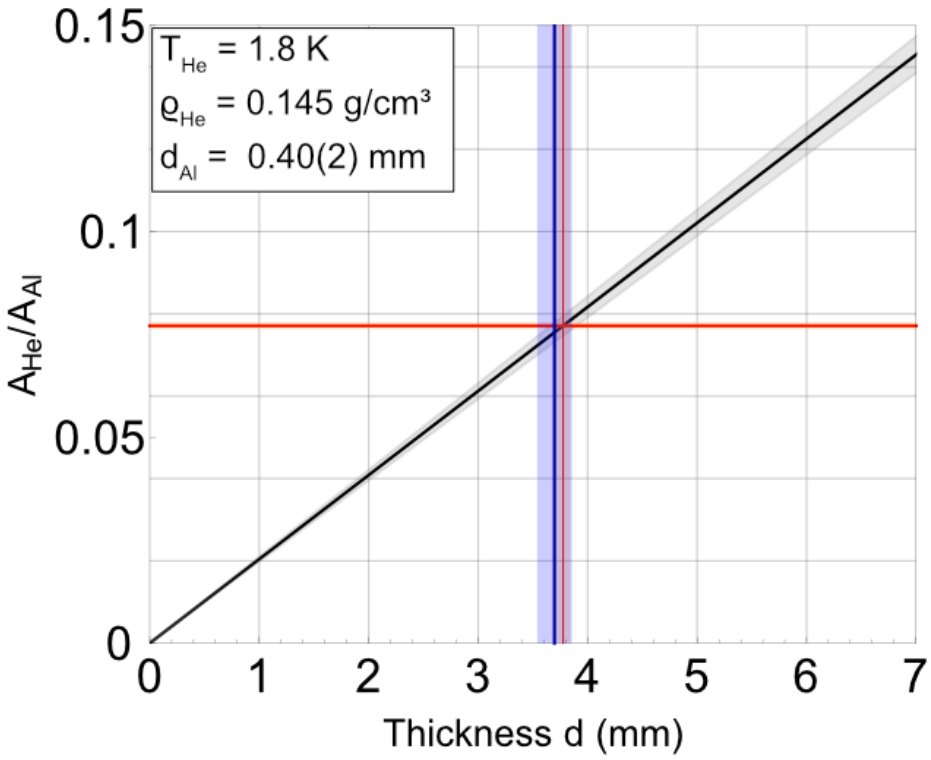

Figure 62: Determination of the experimental target thickness. The black solid line represents the expected ratio of peak areas of elastic electron scattering on helium vs. the aluminum windows as a function of the helium target thickness. The horizontal orange band represents the experimental ratio $A_{\mathrm{He}}/A_{\mathrm{Al}}$. The intersection point with the black line is used to determine the measured target thickness (vertical orange band). The blue band represents the expected target thickness based upon the manufacturer's specifications. Taken from [19].

As it can be seen, the experimentally determined thickness conforms with the expected thickness. The experimental result for the target thickness is 3.776 mm with an uncertainty budget as follows: 0.006^2 mm^2 variance from counting statistics and 0.044^2 mm^2 variance from all other measurands in conformity with the manufacturer's specification. The measurement confirmed an areal mass density of $\bar{m}_{\mathrm{He,exp}} = (54.9 \pm 1.0)$ mg/cm^2.

The usability of superfluid helium as target material and the functionality of the cryostat could be confirmed with the performed commissioning experiment. However, during the experiment there were problems to hit the target correctly with the electron beam. This had two known reasons: First, the alignment of the scattering chamber and the beam guidance relative to the spectrometer and the accelerator was inaccurate. This problem was addressed with the help of the Frankfurt geodesists. The second problem was the target cell's hit area, which was too small. For this reason, a new cell was developed.

7. Design of Improved Target cell

With the new target cell, it must be ensured that a sufficiently large effective area is available for the electron beam at any scattering angle. At the same time, the window surface must be as small as possible, since the windows should be as thin as possible but must withstand an overpressure of at least 1.2 bar. Due to the geometric extension of the target, a part of the target is cut off, so that the effectively available area is reduced as it is shown in Figure 63.

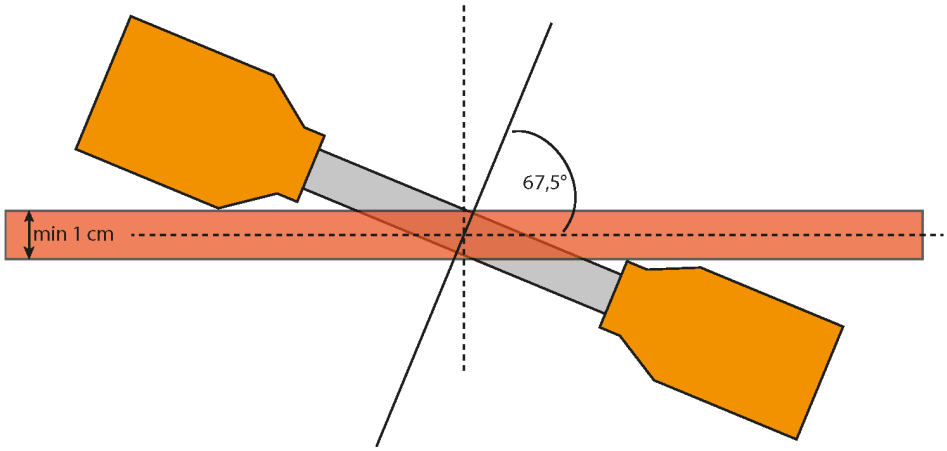

Figure 63: View of the target cell from above. The electron beam should always have at least 1 cm hit area in all directions. The most extreme value results for a scattering angle of 135°, which means an angle of 67.5° between the axis perpendicular to the target and the beam axis.

The scattering chamber has spectrometer flanges for the scattering angles θ at 55°, 75°, 95°, 115°, 135° and 155°. According to Figure 17, the angles between 55° and 135° should be measured in transmission geometry (Figure 64, left), the angle 155° in reflection geometry (Figure 64, right).

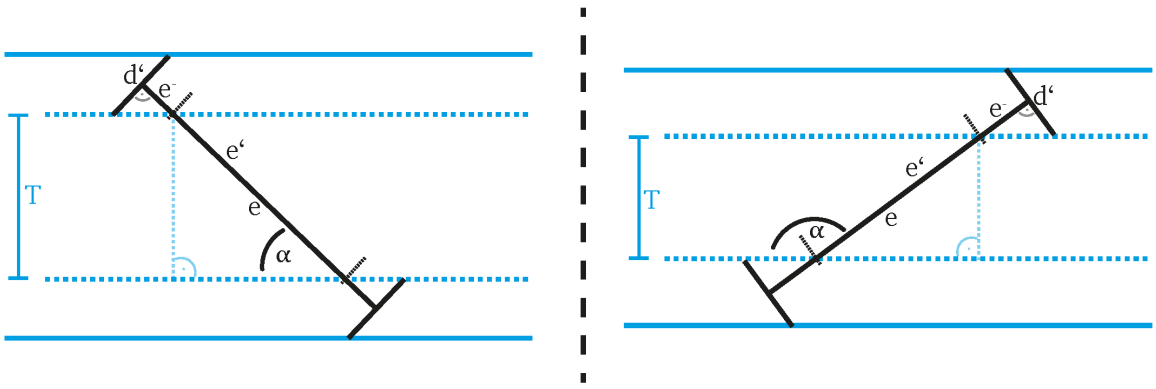

Figure 64: Necessary quantities for calculating the minimum window expansion *e* for different scattering angles. Left: Target alignment in transmission geometry for scattering angles between 55° and 135°. Right: Target alignment in reflection geometry for the scattering angle 155°.

For the target alignment in transmission geometry is $\alpha_{\mathrm{trans}} = 180° - \theta/2 - 90°$ which results in values between 22.5° and 62.5°. For the target alignment in reflection geometry it is $\alpha_{\mathrm{refl}} = 180° - \theta/2 = 102.5°$.

The minimal value for the effective width T of the target area should be 1 cm [49]. The minimal size of the window is $e = e' + 2 \cdot e^-$. For the transmission geometry, based on Figure 64, it is

$$e^- = \frac{d'}{2 \cdot \tan \alpha} \tag{7.1}$$

$$e' = \frac{T}{\sin \alpha} \tag{7.2}$$

$$e = \frac{T}{\sin \alpha} + \frac{d'}{\tan \alpha}. \tag{7.3}$$

For the reflection geometry it is

$$e^- = -\frac{d'}{2 \cdot \tan \alpha} \tag{7.4}$$

$$e' = \frac{T}{\sin \alpha} \tag{7.5}$$

$$e = \frac{T}{\sin \alpha} - \frac{d'}{\tan \alpha}. \tag{7.6}$$

If one assumes that the brace with which the aluminum windows are pressed against the target cell can be completely beveled so that they do not obstruct the electron beam as it is shown in Figure 65, then the thickness d' is only given by the extent of the helium cavity, the thickness of the aluminum windows and the indium seal between copper housing and aluminum plate. This makes a minimum size $d' = 3.9$ mm, if the uncertain thickness of the indium remains is rather large.

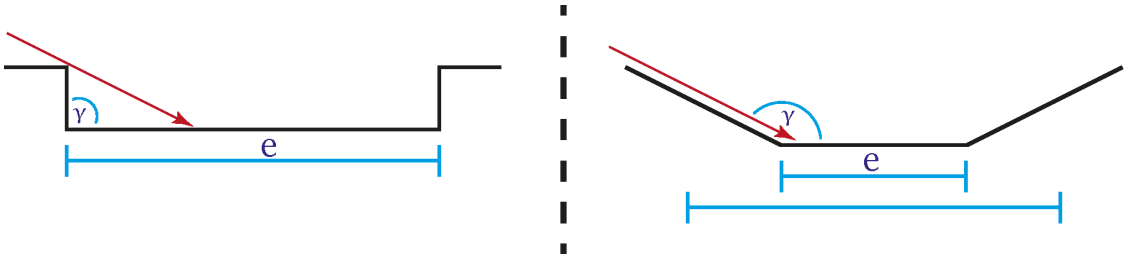

Figure 65: Illustration of the minimum target extension e for a right-angled bracket on the left side, and a fully beveled bracket on the right side. The bevel can significantly reduce the required window area. The minimum angle γ is 157.5° if the electron beam is not to be restricted by the bracket at any scattering angle.

Table 7 lists required values for the minimum target extension of the individual scattering angles. The most disadvantageous value is that for the scattering angle of 135° in transmission geometry. Therefore, a minimum target extension of 36 mm is used for further consideration. In the current target cell, the windows are circular with a diameter of 20 mm. In the direction perpendicular to the beam axis (up and down), however, the hit area does not depend on the rotation of the target capsule relative to the beam axis. This means that the window size in this direction could actually be reduced. Therefore, a cell with oval windows with a second axis of 12 mm is considered.

Table 7: Required values for the minimum target extension for the possible scattering angles. The most disadvantageous value results for the scattering angle of 135° in transmission geometry.

Scattering angle θ	Geometry	Target angle α	Min. extension e
55°	transmission	62.5°	13.3 mm
75°	transmission	52.5°	15.6 mm
95°	transmission	42.5°	19.1 mm
115°	transmission	32.5°	24.7 mm
135°	transmission	22.5°	35.5 mm
155°	reflection	102.5°	11.1 mm

The windows of the target cell should be as thin as possible so that the scattering rate on the aluminum contributes as little as possible to the overall scattering intensity. However, the windows must withstand a pressure of at least 1.2 bar, because during the cooling process, normal pressure prevails inside the cell, while the surrounding scattering chamber is kept under vacuum. Furthermore, it must always be considered that a malfunction of the reduction of pressure in the target cell could occur. The attached safety valves will all open at an overpressure of 1.2 bar. As these are specific cold valves, the valves also open when frozen, but then they cannot be closed anymore. To find the ideal ratio of target size to window thickness, various simulations were carried out using the Autodesk Fusion 360 software [50].

In a first step, a model of the current target geometry with round windows was created and simulations for three different overpressures (1.2 bar, 1.6 bar and 2.0 bar) were performed. The critical points of the cell are the aluminum windows. All parts of the cell that are irrelevant for the simulation, for example the supply piping, were simplified or not considered in order not to increase the simulation costs unnecessarily. The safety factor of the construction is considered. A safety factor smaller than 1 means that the construction will break in any case. Usually a safety factor of at least 3 is aimed for. A picture of the results can be found in Figure 66.

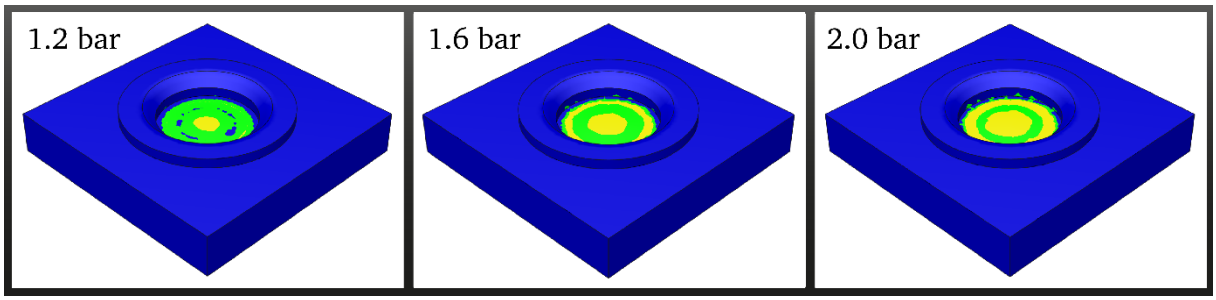

Figure 66: Simulation results for the current circular target cell for different overpressures as reference for the construction of the new window geometry. The smallest safety factor for 1.2 bar overpressure is 2.4 in the center of the aluminum windows. For 1.6 bar overpressure the minimum safety factor is 1.8, for 2.0 bar overpressure 1.4.

Blue areas are completely stable with a safety factor of at least 6, green areas have a safety factor between 3 and 6 and offer an ideal balance between material thickness and stability. Yellow surfaces mean a safety factor between 1 and 3. In principle, the construction should be

able to withstand the pressure, but the margin for material defects is undesirably small. Red surfaces mean a safety factor less than 1 and thus a certain breakage. In the current circular geometry, the smallest safety factor for 1.2 bar overpressure is 2.4 and thus smaller than the desired minimum value of 3, but not too far away. In order to avoid unnecessarily large background through the aluminum windows, a somewhat fragile construction must be accepted in this case. For an overpressure of 1.6 bar there is a safety factor of at least 1.8 and for an overpressure of 2 bar there is a safety factor of at least 1.4. These values should also not be undercut for the new cell.

Various designs were tested for the construction of the new cell. A design with oval windows and completely beveled bracket edges according to Figure 65 was rated best. The short axis of the oval windows is 12 mm and the long axis is 36 mm. The angle between the window surface and the bracket edge is 158°. This should allow the electron beam to propagate completely through the target at any scattering angle without interfering with the copper parts. The oval target geometry even turned out to be more stable than the circular geometry in the simulations, hence the window thickness could be reduced by 25 % to 0.15 mm each. Results are shown in Figure 67.

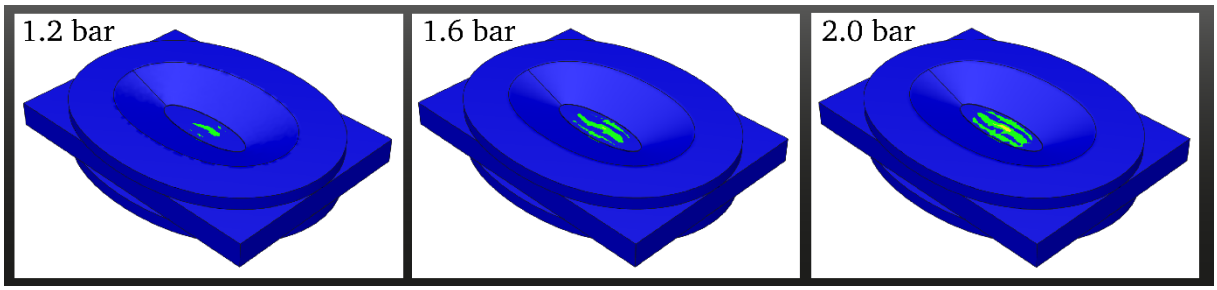

Figure 67: Simulation results for an oval target cell with completely beveled edge. The short axis is 12 mm long, the long axis 36 mm. The window thickness is 0.15 mm, each. For an overpressure of 1.2 bar the smallest safety factor is 3.0, for an overpressure of 1.6 bar it is 2.2 and for an overpressure of 2.0 bar it is minimal 1.8.

At an overpressure of 1.2 bar the minimum safety factor is 3.0. At an overpressure of 1.6 bar the safety factor is at least 2.2 and at an overpressure of 2.0 bar it is a minimum of 1.8. This means that this cell is slightly more stable than the current circular cell, even though the windows are larger but thinner. A further reduction of the aluminum thickness significantly reduces the safety factor and is therefore not ideal.

As a further change, the use of stainless-steel windows instead of aluminum windows was tested. Steel consists mainly of iron and carbon. The elastic scattering rate of electrons is related quadratically to the atomic number. The atomic number of aluminums is 13, that of iron 26.

$$\frac{Z_{\mathrm{Al}}^2}{Z_{\mathrm{Fe}}^2} = \frac{13^2}{26^2} = 0.25 \tag{7.7}$$

The areal mass density of a stainless-steel disc must not exceed one quarter of that of aluminum to be preferable. To obtain the maximum thickness of the windows, the density of stainless steel must be considered. The density of typical stainless steel is 8.0 g/cm^3, the density of aluminum is 2.7 g/cm^3.

$$\frac{2.7\ \mathrm{g/cm^3}}{8.0\ \mathrm{g/cm^3}} = 0.3375 \approx \frac{1}{3} \tag{7.8}$$

The thickness of the panes must therefore be further reduced by a factor of 3. The maximum thickness for stainless steel windows is 1/12 of the thickness of aluminum windows if the same background contribution is to be achieved. If the thickness of stainless-steel windows can be reduced even further without reducing the stability, then stainless-steel windows would be preferable, at least from this point of view.

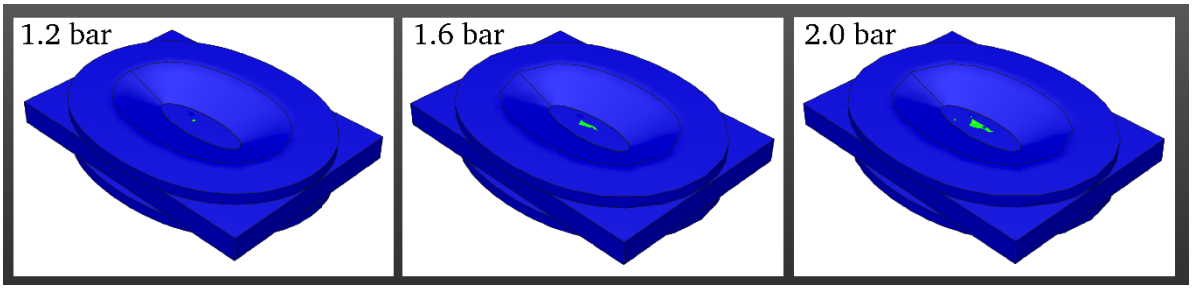

Figure 68: Simulation results for an oval target cell with stainless-steel windows. The window thickness is 1/16 of the aluminum thickness shown in Figure 67. For an overpressure of 1.2 bar the smallest safety factor is 3.3. For an overpressure of 1.6 bar it is 2.6 and for an overpressure of 2.0 bar it is minimal 2.0.

Figure 68 shows results for a simulation with stainless-steel windows. A thickness of 1/16 of the aluminum thickness of Figure 67 gives good results. The smallest safety factor for an overpressure of 1.2 bar is 3.3. For a 1.6 bar overpressure it is still 2.6 and for an overpressure of 2.0 bar it is 2.1. This reduces the elastic scattering rate at the windows but still increases stability.

8. Summary

The aim of this work was to develop a new target system for electron scattering experiments on superfluid helium at the QCLAM spectrometer. A 3-stage helium cryostat with scattering chamber and target cell was designed.

After manufacturing the cryostat was assembled and tested. A special challenge was the fragile construction of the cryostat, which is inevitable to reach the required cryogenic temperatures. The cryostat and all related components and measuring instruments must therefore be handled with special care. Following the tests at room temperature, tests had to be carried out at low temperatures. A cooling procedure was developed to reach these conditions. This was one of the most challenging parts of this work, as procedures of this kind are unique to each cryostat and therefore existing knowledge could only be used to a limited extent. After successful completion of the cooling process, tests at cold temperatures could be carried out at first without an electron beam. As soon as the cryostat had been brought to the required temperatures, further treatment was comparatively straight forward, and the entire cryostat was remarkably stable.

In a subsequent commissioning experiment the cryostat could prove its functionality under realistic experimental conditions. The cryostat maintained its convenient stability even when the electron beam fluctuated significantly. The evaluation of the elastic scattering data proves the functionality and the advantages of superfluid helium as target material. In the following beam time, the target system can be used to study the monopole transition form factor of the first excited 0^+ state, as well as the longitudinal response function. These measurements could make an important contribution to resolve questions in the formulation of the chiral EFT framework. Problems resulting from the fact that the effective helium density is difficult to estimate should no longer occur with the new target system and the use of superfluid helium as target material.

During the experiment there were two main problems with the alignment of the scattering chamber and the beam guiding elements as well as with the shape of the target cell windows. Both problems were addressed. The relative positions of the spectrometer and the accelerator were measured with the help of the geodesists and the beamline and the scattering chamber were realigned accordingly. In addition, a new target cell was designed where the focus was put on the minimization of the background through scattering of the electron beam off the casing material. Proof of the effectiveness of the problem treatment is still pending and must be tested during the next beam time.

The use of the cryostat system for elements other than helium is possible in principle, provided that the desired isotope can be made available in sufficient quantity in liquid form.

9. References

[1] R. Hofstadter, Rev. Mod. Phys. **28**, 214 (1956).
[2] N. Pietralla, Nuclear Physics News **28**, 4 (2018).
[3] C. A. Bertulani, *Nuclear physics in a nutshell* (Princeton University Press, Princeton N.J., 2007).
[4] R. B. Wiringa, V. G. J. Stoks, and and R. Schiavilla, Phys. Rev. C **51**, 38 (1995).
[5] R. Machleidt, Phys. Rev. C **63** (2001).
[6] H. Yukawa, Proc. Phys. Math. Soc. Japan **17**, 48 (1935).
[7] R. Machleidt, Adv. Nucl. Phys. **19**, 189 (1989).
[8] E. Epelbaum, H.-W. Hammer, and U.-G. Meißner, Rev. Mod. Phys. **81**, 1773 (2009).
[9] S. Bacca, N. Barnea, W. Leidemann, and G. Orlandini, Phys. Rev. C **80** (2009).
[10] T. Walcher, Physics Letters **31B**, 442 (1970).
[11] S. Bacca, N. Barnea, W. Leidemann, and G. Orlandini, Physical review letters **110**, 42503 (2013).
[12] A. Schwenk and N. Pietralla, Nuclei: From Fundamental Interactions to Structure and Stars. Planned Collaborative Research Centre 1245, 2015.
[13] R. Donnelly and C. Barenghi, Journal of Physical and Chemical Reference Data **27**, 1217 (1998).
[14] T. Walcher, Z. Physik **237**, 368 (1970).
[15] C. Enss and S. Hunklinger, *Low-Temperature Physics* (Springer, Berlin, Heidelberg, 2005).
[16] Beat Hahn, D. G. Ravenhall, and and Robert Hofstadter, Physical review **101**, 1131 (1956).
[17] H. Überall, *Electron Scattering from Complex Nuclei. Part A* (Academic Press, New York, 1971), Vol. 1.
[18] M. Hilcker, Masterarbeit, Technische Universität Darmstadt, 2016.
[19] M. Hilcker *et al.*, Nuclear Instruments and Methods in Physics Research Section A: Accelerators, Spectrometers, Detectors and Associated Equipment **957**, 163418 (2020).
[20] N. F. Mott, Proc. R. Soc. Lond. A **124**, 425 (1929).
[21] W. R. Leo, *Techniques for nuclear and particle physics experiments. A how to approach ; with 40 tables and numerous worked examples* (Springer, Berlin, Heidelberg, New York, London, Paris, Tokyo, Hong Kong, Barcelona, Budapest, 1994).
[22] G. F. Knoll, *Radiation detection and measurement* (Wiley, New York, NY, 2000).
[23] J. Wilks, *An introduction to liquid helium* (Clarendon Pr, Oxford, 1970).
[24] C. Enss and S. Hunklinger, *Tieftemperaturphysik. Mit 22 Tabellen* (Springer, Berlin, Heidelberg, New York, Barcelona, Hongkong, London, Mailand, Paris, Singapur, Tokio, 2000).
[25] F. Pobell, *Matter and methods at low temperatures. With 28 tables, and 81 problems* (Springer, Berlin, Heidelberg, New York, 2007).
[26] D. Belic *et al.*, Physical review letters **83**, 5242 (1999).
[27] M. Arnold, Dissertation, Technische Universität Darmstadt, 2016.
[28] D. Savran *et al.*, Nuclear Instruments and Methods in Physics Research Section A: Accelerators, Spectrometers, Detectors and Associated Equipment **613** (2010).
[29] M. Knirsch, Dissertation, Technische Hochschule Darmstadt, 1991.
[30] B. Reitz, Dissertation, Technische Universität Darmstadt, 2000.
[31] M. Singer, Dissertation, Technische Universität Darmstadt, 2019.
[32] K.-D. Hummel, Dissertation, Technische Hochschule Darmstadt, 1992.
[33] A. D'Alessio, Masterarbeit, Technische Universität Darmstadt, 2016.

[34] A. Schwenk and N. Pietralla, Collaborative Research Centre 1245: Nuclei - From Fundamental Interaction to Structure and Stars. 2nd Funding Period 2020 - 2023, 2019.
[35] D. Walther (Visit).
[36] M. W. Kuss, Diplomarbeit, Technische Hochschule Darmstadt, 1990.
[37] D. Groom, *Atomic Nuclear Properties*, 2014, http://pdg.lbl.gov/2015/AtomicNuclearProperties/, accessed May 13, 2019.
[38] Messer, *Helium. Physikalische Eigenschaften*, https://www.messer.at/documents/20556/1050339/Helium_phys.pdf/, accessed Mar 11, 2020.
[39] F. Gudden, G. Fricke, H.-G. Clerc, and P. Brix, Zeitschrift für Physik **181**, 453 (1964).
[40] A.Y. Buki, I. S. Timchenko, N. G. Shevchenko, and I. A. Nenko, Physics Letters B **641**, 156 (2006).
[41] A. Brauch, Bachelorarbeit, Technische Universität Darmstadt, 2018.
[42] M. Lösler *et al.*, Zeitschrift für Geodasie, Geoinformation und Landmanagement **140**, 346 (2015).
[43] J. Birkhan (Software).
[44] L. Jürgensen, Dissertation, Technische Universität Darmstadt, 2018.
[45] Wolfram Research Inc., Mathematica (Wolfram Research Inc., Champaign, 2019).
[46] H. Matsubara, Dissertation, Osaka University, 2010.
[47] S. Strauch, Diplomarbeit, Technische Universität Darmstadt, 1993.
[48] a) I. Sick, Progress in Particle and Nuclear Physics **47**, 245 (2001); b) T. Stovall, d. Vinciguerra, and M. Bernheim, Nuclear Physics A **91**, 513 (1967);
[49] L. Jürgensen (Oral communication).
[50] Autodesk Inc., Autodesk Fusion 360 (Autodesk Inc., San Rafael, 2020).

10. Appendix

10.1. Camera System

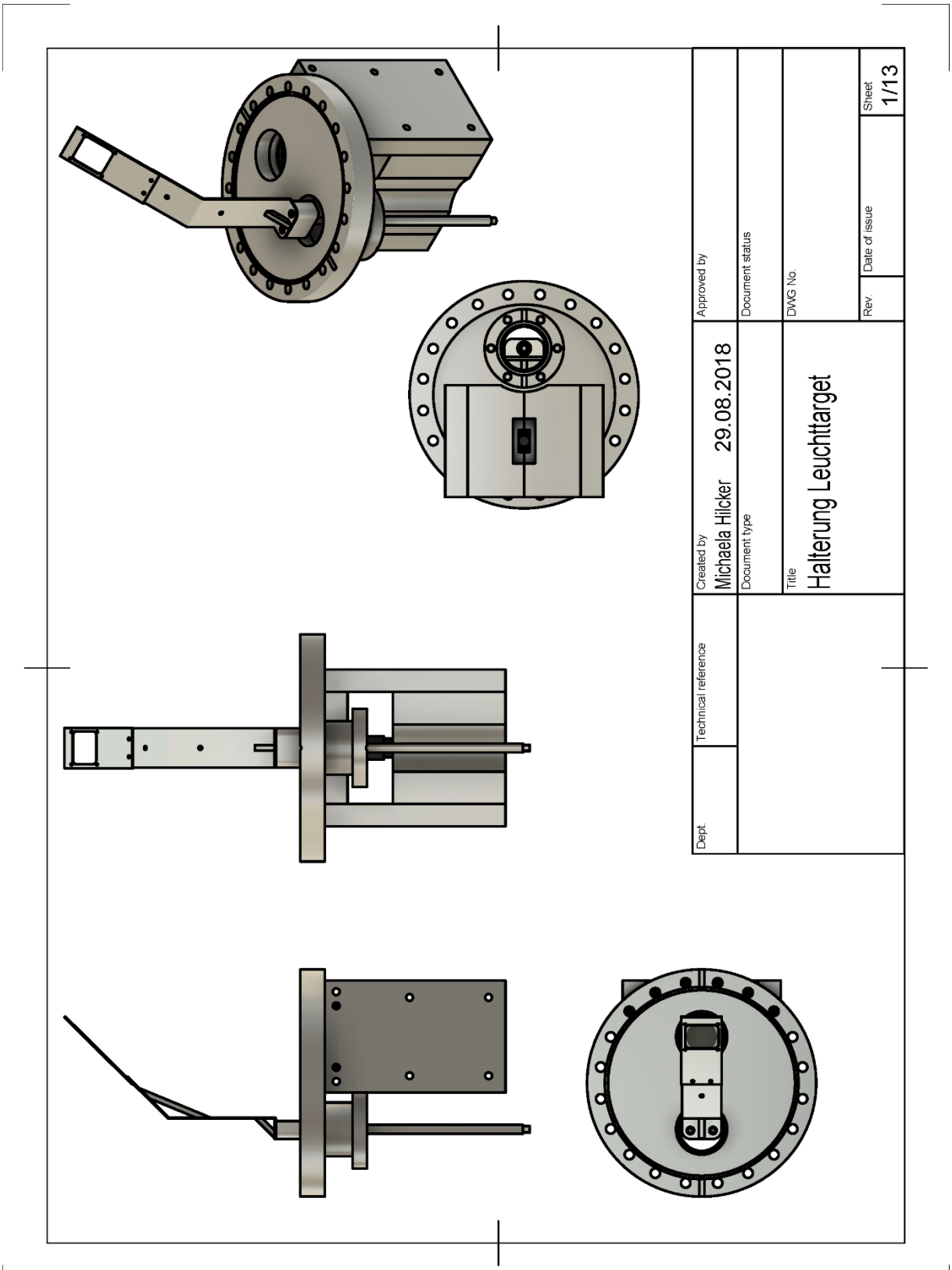

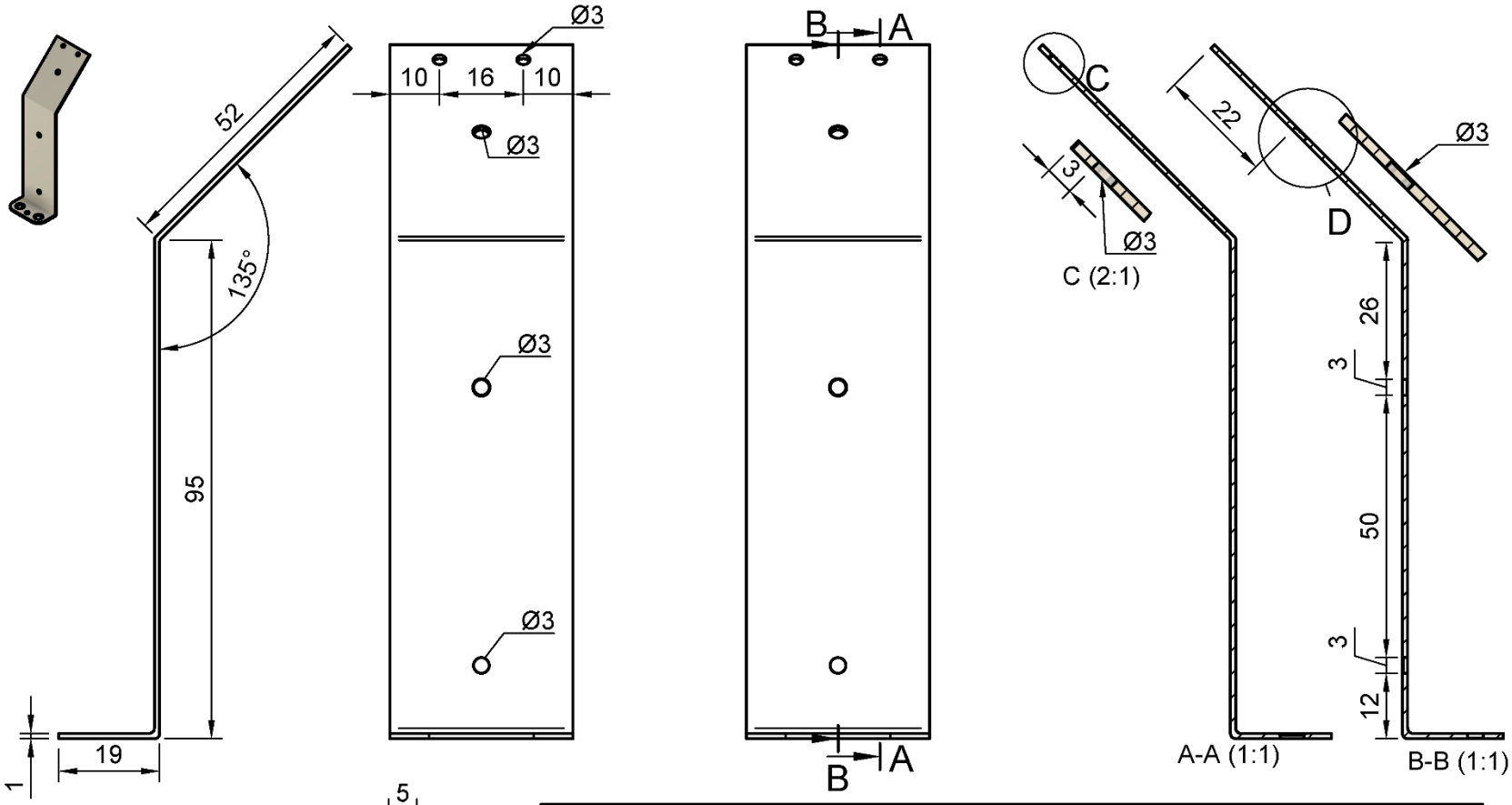

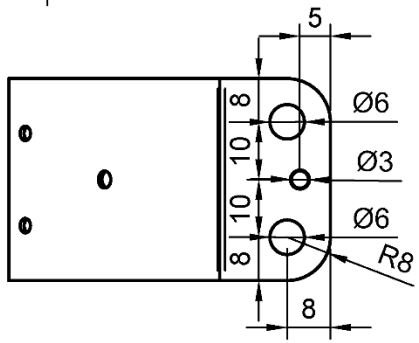

Dept.	Technical reference	Created by Michaela Hilcker 29.08.2018	Approved by	
		Document type	Document status	
		Title Halterung Leuchttarget	DWG No.	
			Rev.	Date of issue / Sheet 2/13

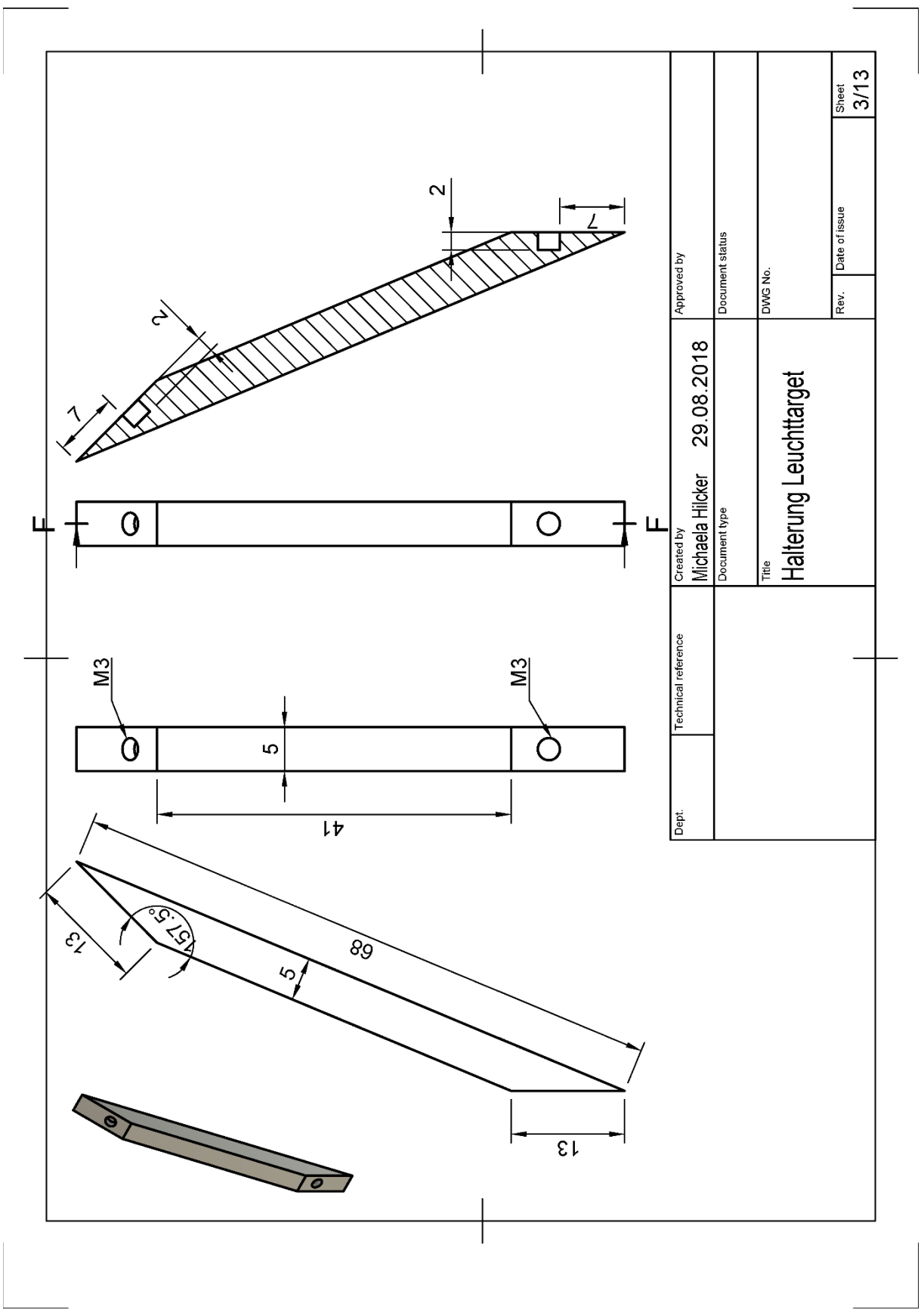
2
7
2
7
F
F
M3
M3
5
41
13
157.5°
68
5
13
Dept.
Technical reference
Created by
Michaela Hilcker
29.08.2018
Document type
Approved by
Document status
DWG No.
Title
Halterung Leuchttarget
Rev.
Date of issue
Sheet
3/13

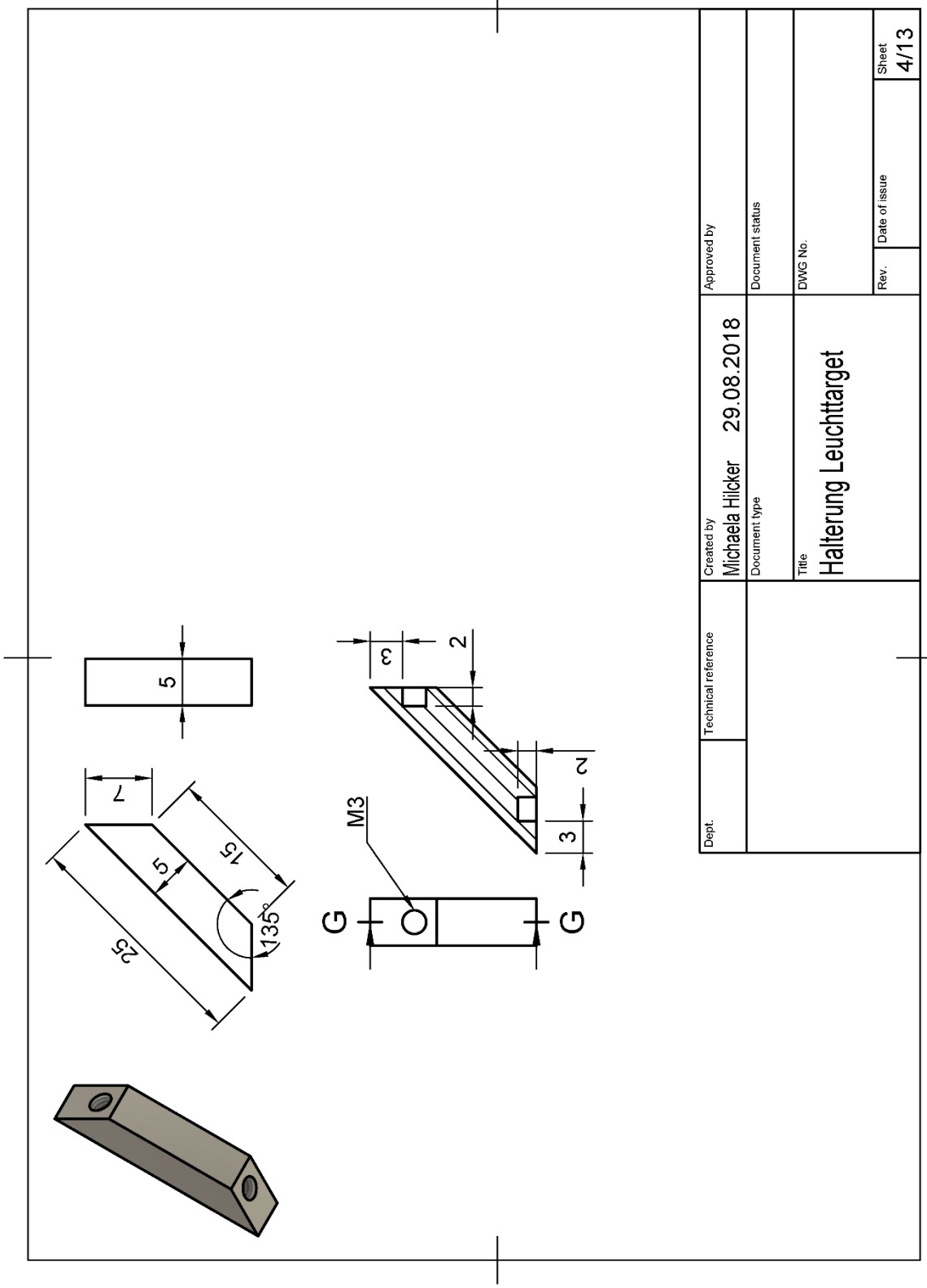
5
7
15
5
135°
25
M3
G
G
3
2
2
3
Dept.
Technical reference
Created by
Michaela Hilcker 29.08.2018
Document type
Approved by
Document status
Title
Halterung Leuchttarget
DWG No.
Rev.
Date of issue
Sheet
4/13

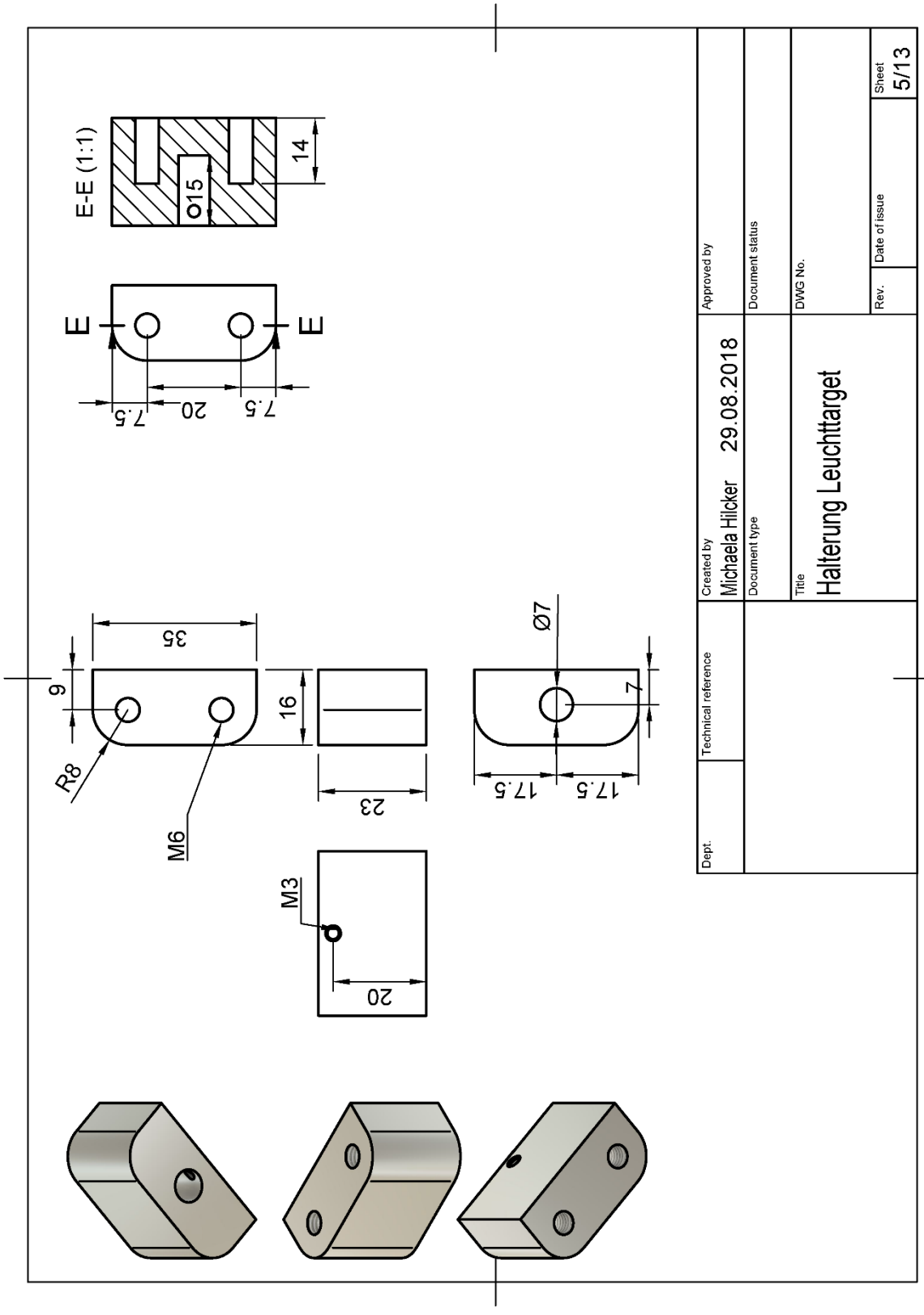
E-E (1:1)
14
Ø15
E
E
7.5
20
7.5
35
9
16
R8
M6
23
Ø7
7
17.5
17.5
M3
20
Dept.
Technical reference
Created by
Michaela Hilcker
29.08.2018
Approved by
Document type
Document status
Title
Halterung Leuchttarget
DWG No.
Rev.
Date of issue
Sheet
5/13

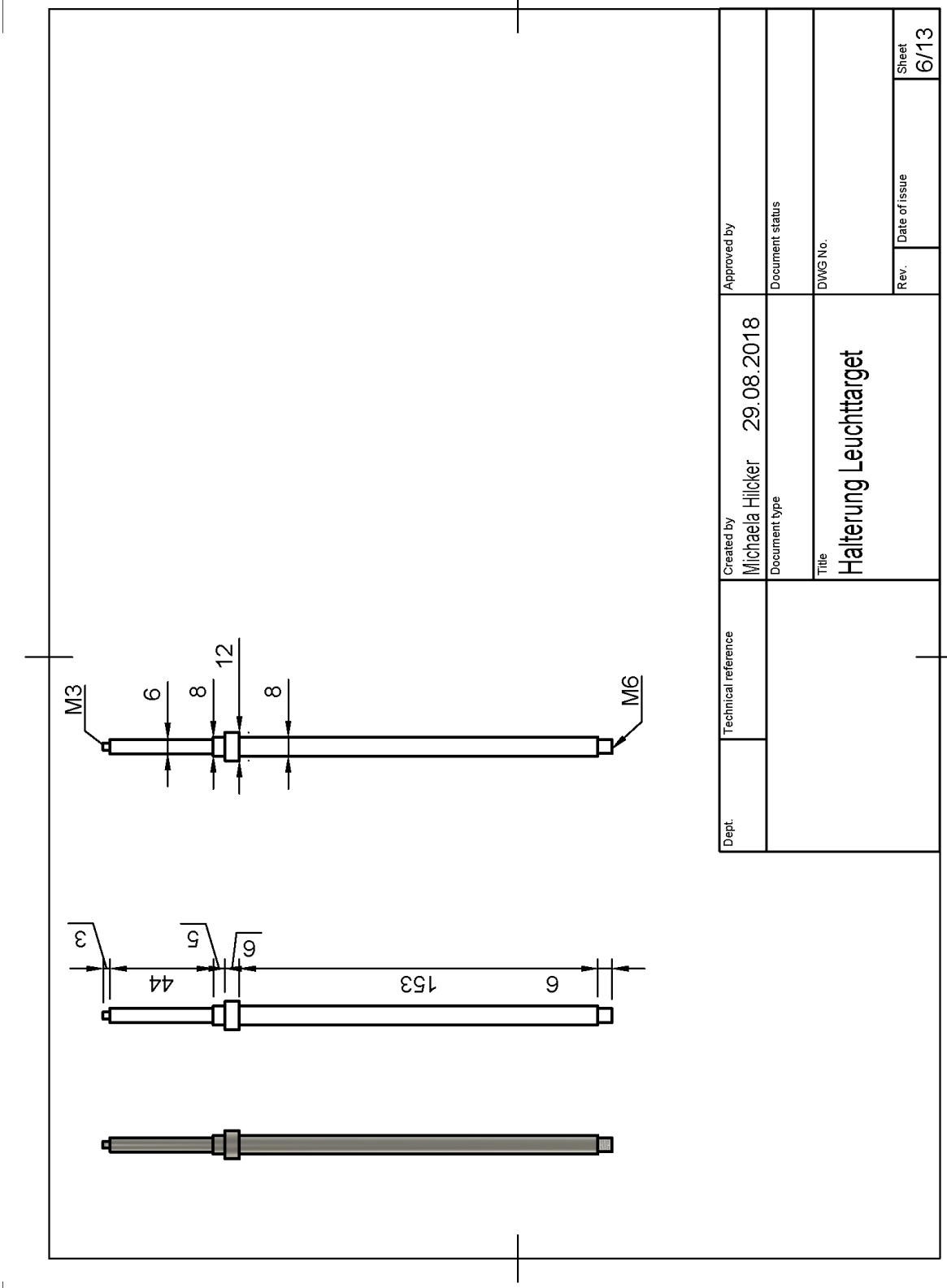
M3
6
8
12
8
M6
3
5
6
44
153
6
Dept.
Technical reference
Created by
Michaela Hilcker
29.08.2018
Document type
Approved by
Document status
Title
Halterung Leuchttarget
DWG No.
Rev.
Date of issue
Sheet
6/13

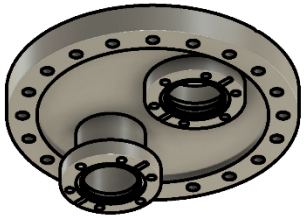

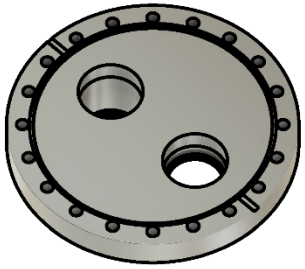

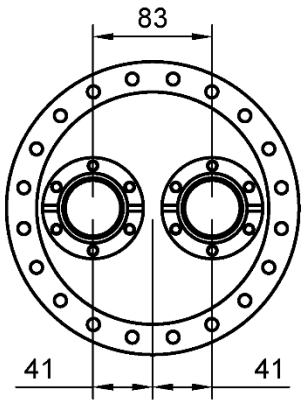

Dept.	Technical reference	Created by Michaela Hilcker 29.08.2018	Approved by	
		Document type	Document status	
		Title Halterung Leuchttarget	DWG No.	
			Rev. / Date of issue	Sheet 7/13

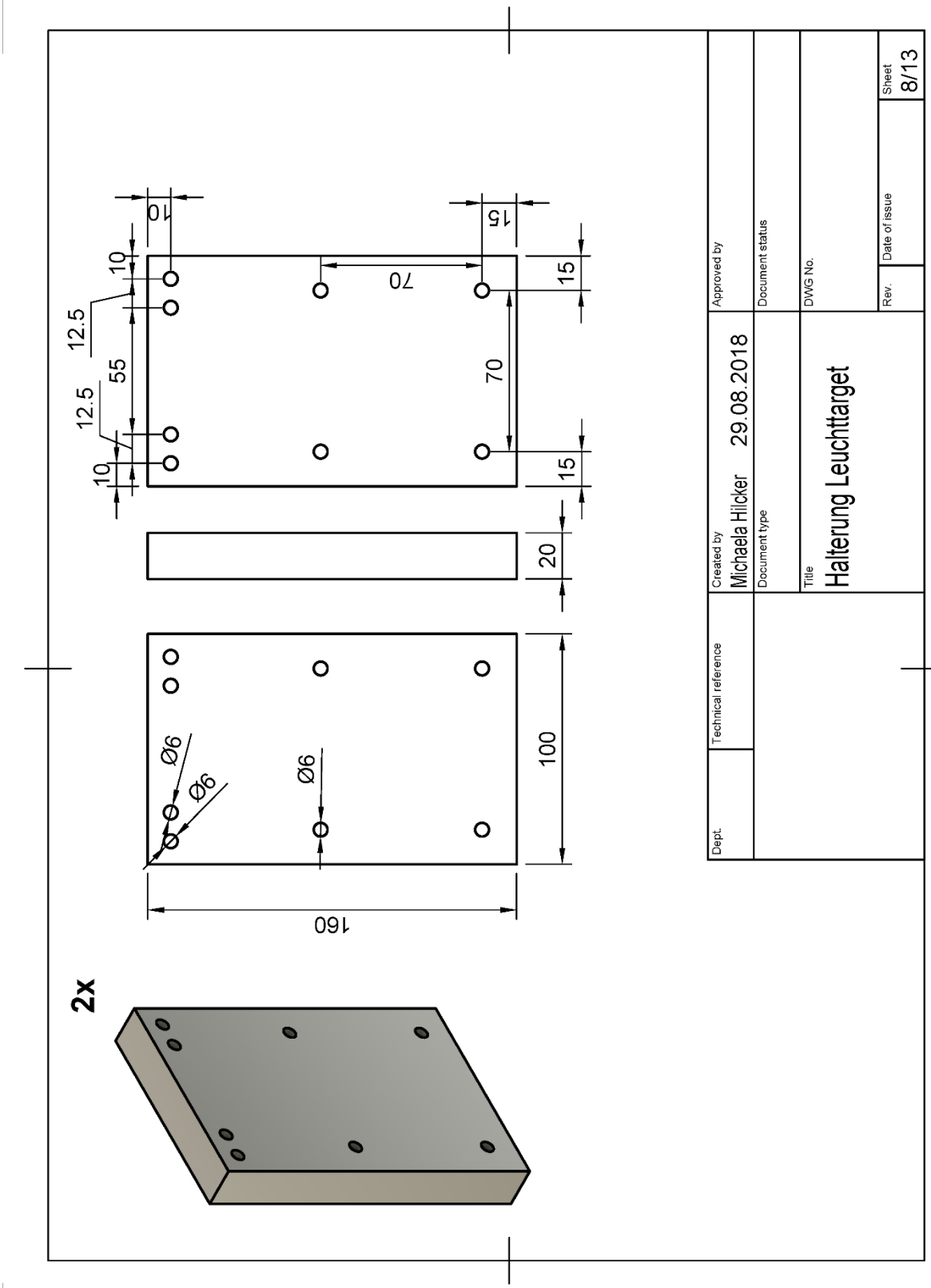
10
15
10
12.5
55
12.5
10
70
15
70
15
20
100
Ø6
Ø6
Ø6
160
2x
Dept.
Technical reference
Created by
Michaela Hilcker 29.08.2018
Document type
Approved by
Document status
Title
Halterung Leuchttarget
DWG No.
Rev.
Date of issue
Sheet
8/13

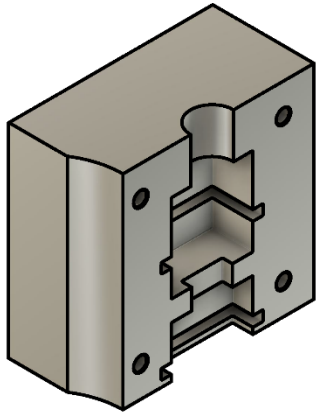

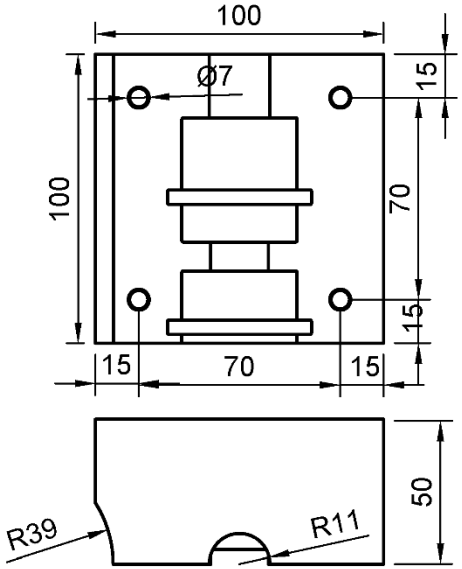

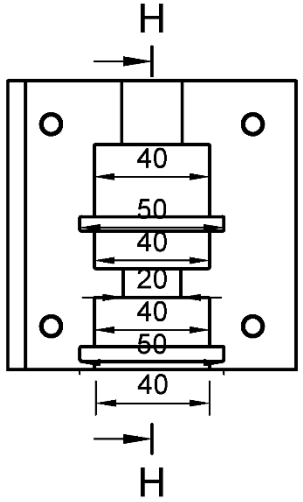

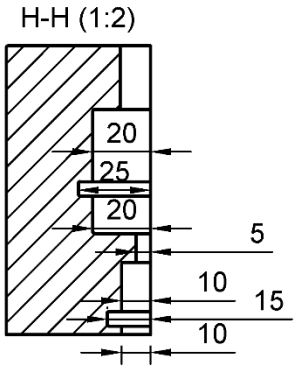

Dept.	Technical reference	Created by Michaela Hilcker 29.08.2018	Approved by
		Document type	Document status
		Title Halterung Leuchttarget	DWG No.
			Rev. / Date of issue / Sheet 9/13

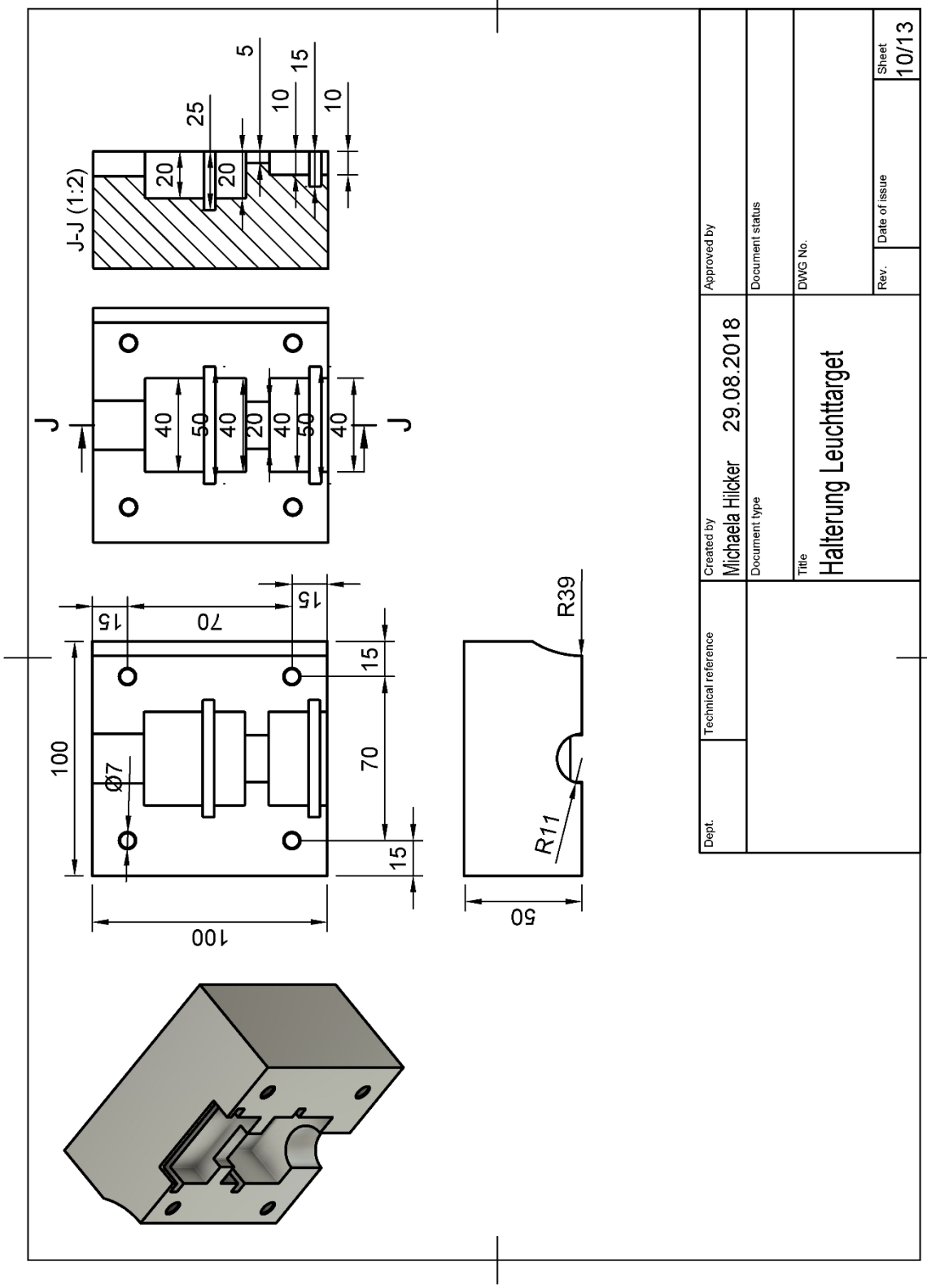
J-J (1:2)
25
5
10
15
10
20
20
J
J
40
50
40
20
40
50
40
15
70
15
100
Ø7
15
70
15
100
R39
R11
50
Dept.
Technical reference
Created by
Michaela Hilcker
29.08.2018
Document type
Approved by
Document status
Title
Halterung Leuchttarget
DWG No.
Rev.
Date of issue
Sheet
10/13

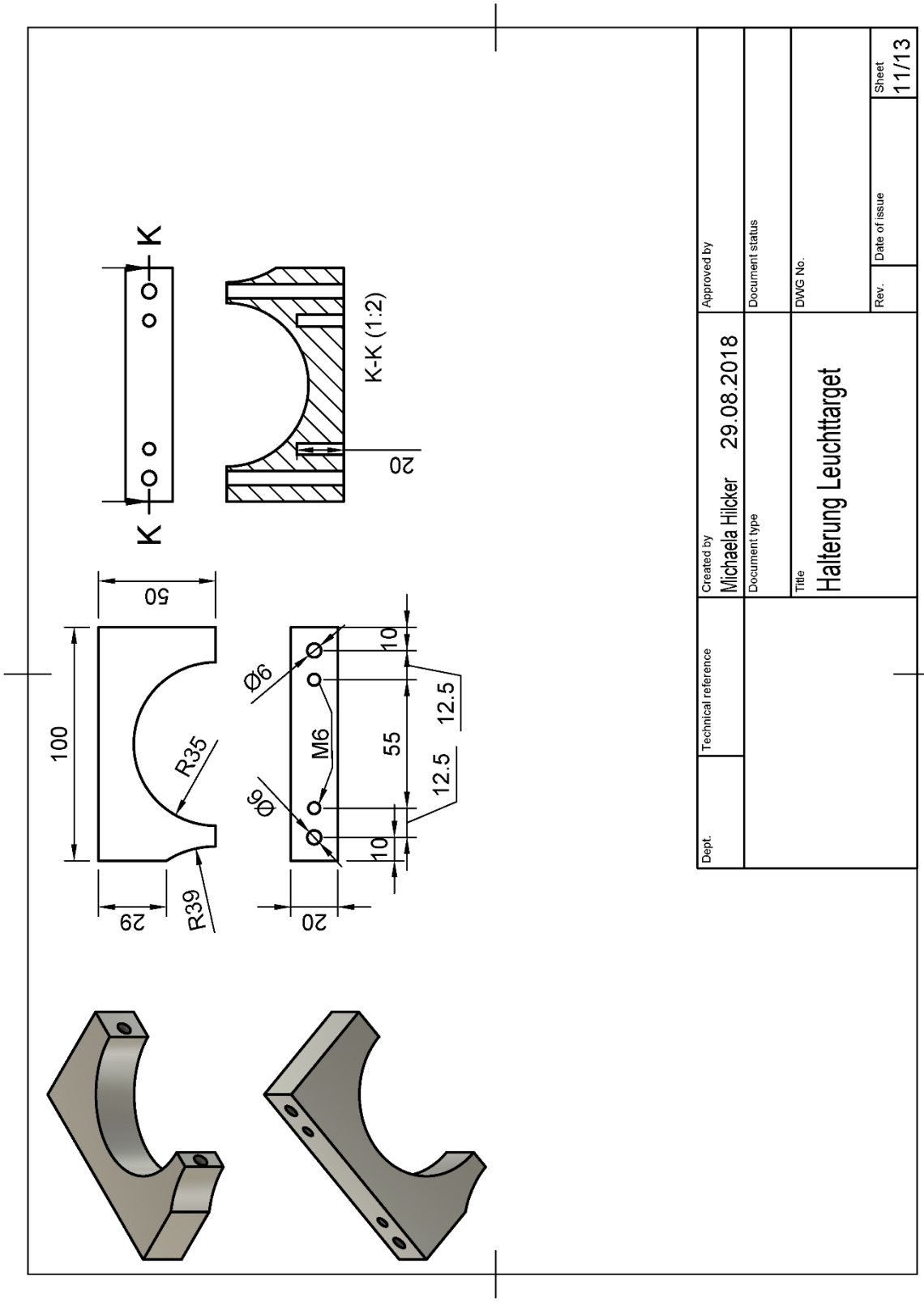
K
K
K-K (1:2)
20
50
100
R35
29
R39
Ø6
M6
Ø6
10
55
12.5
12.5
10
20
Dept.
Technical reference
Created by
Michaela Hilcker
29.08.2018
Approved by
Document type
Document status
Title
Halterung Leuchttarget
DWG No.
Rev.
Date of issue
Sheet
11/13

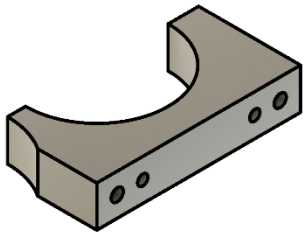

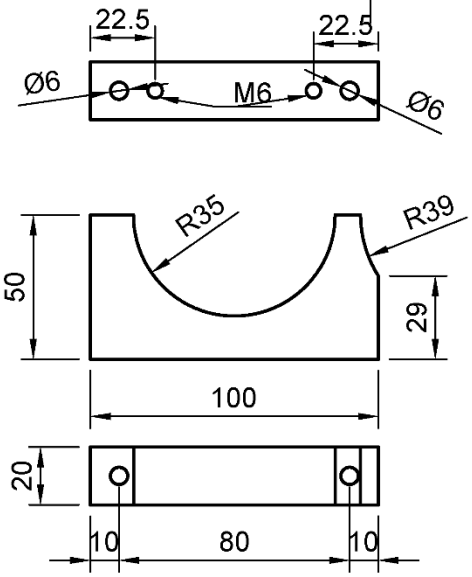

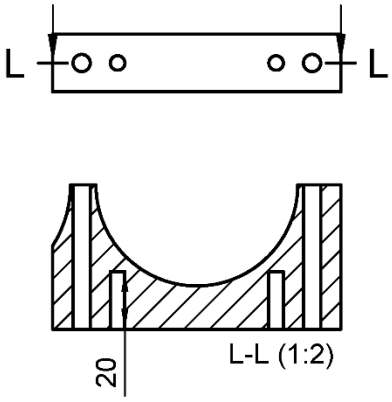

Dept.	Technical reference	Created by Michaela Hilcker 29.08.2018	Approved by
		Document type	Document status
		Title: Halterung Leuchttarget	DWG No.
			Rev. / Date of issue / Sheet 12/13

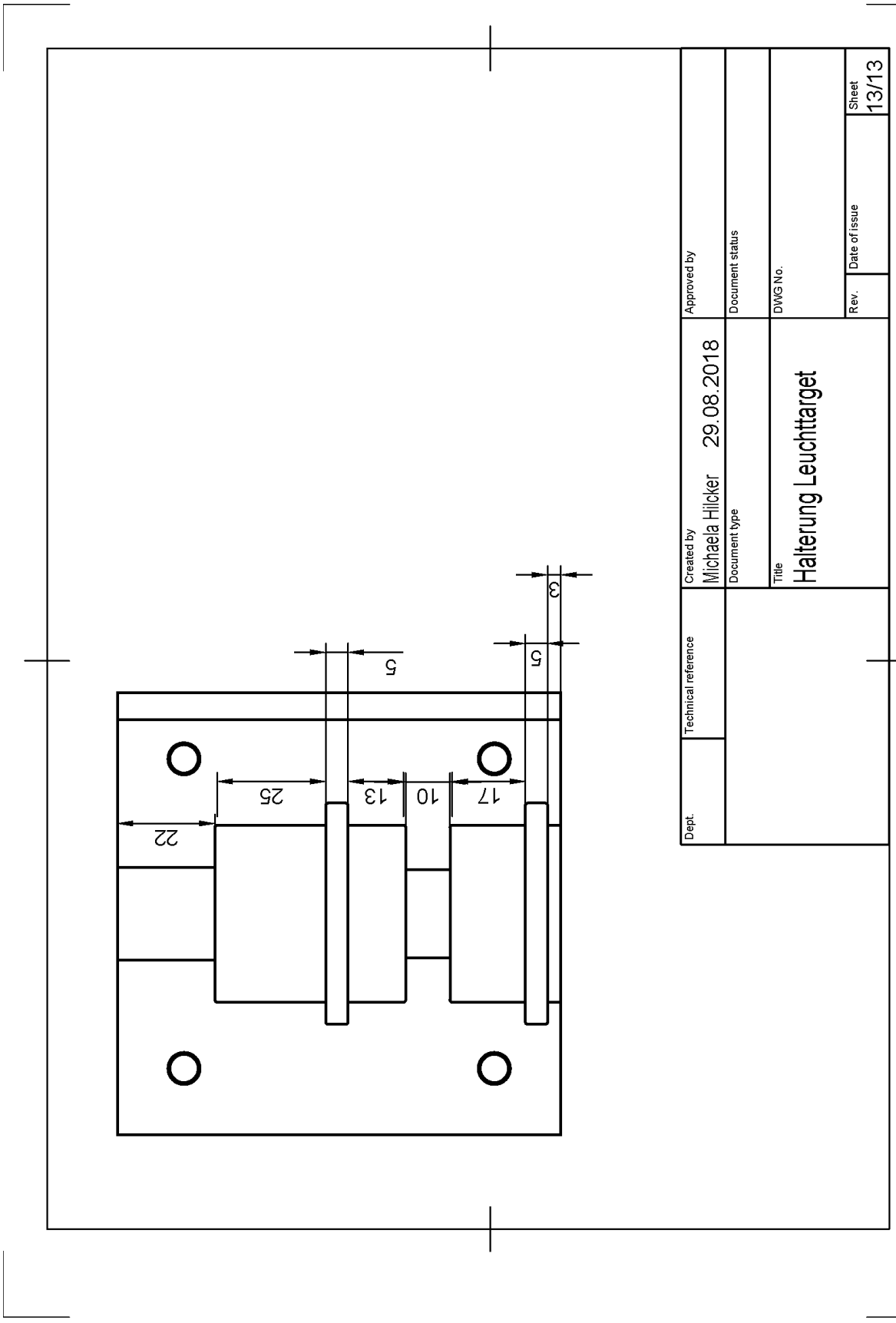
Dept.
Technical reference
Created by
Michaela Hilcker
29.08.2018
Approved by
Document type
Document status
Title
Halterung Leuchttarget
DWG No.
Rev.
Date of issue
Sheet
13/13
3
5
5
22
25
13
10
17

10.2. Scattering chamber

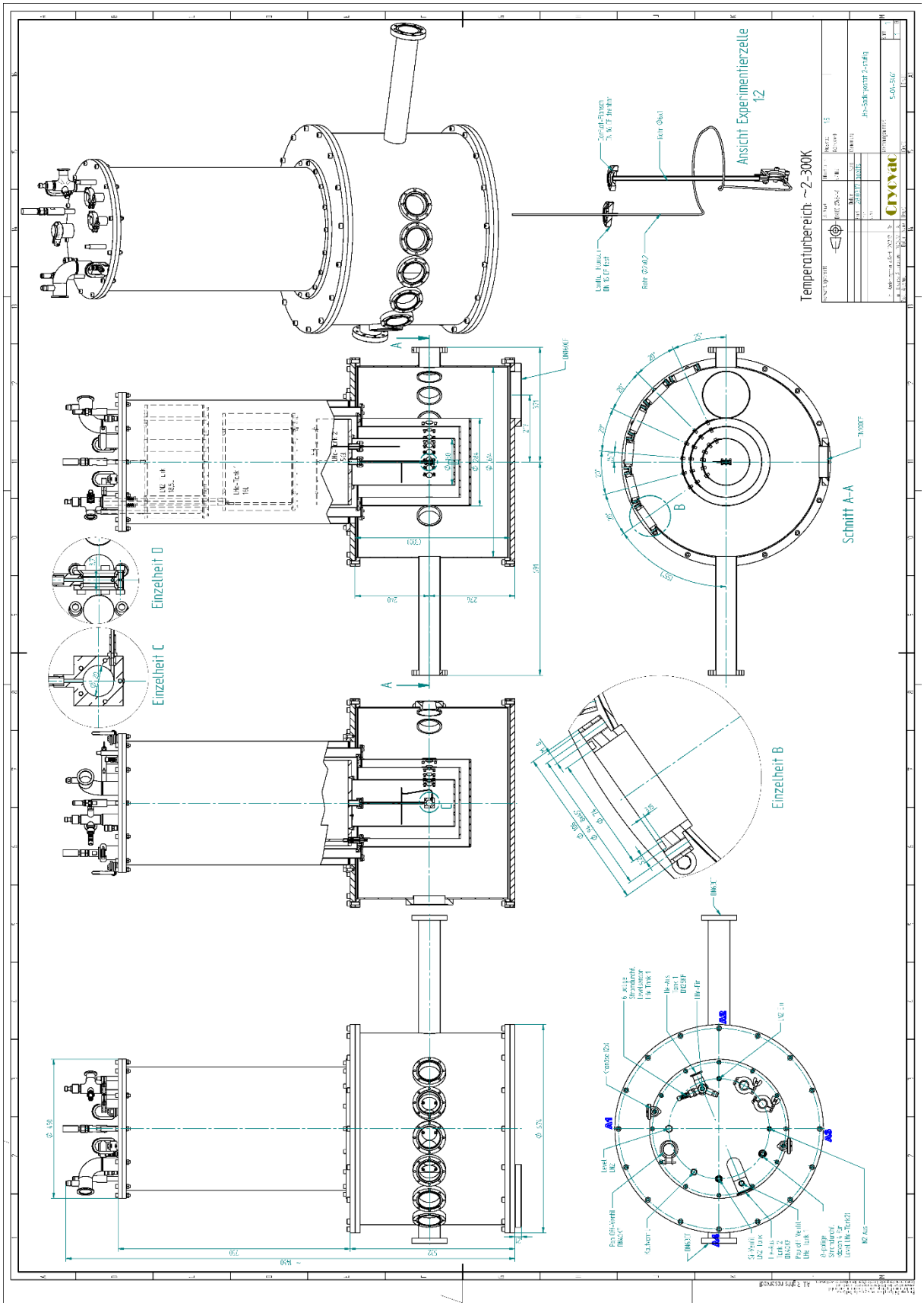

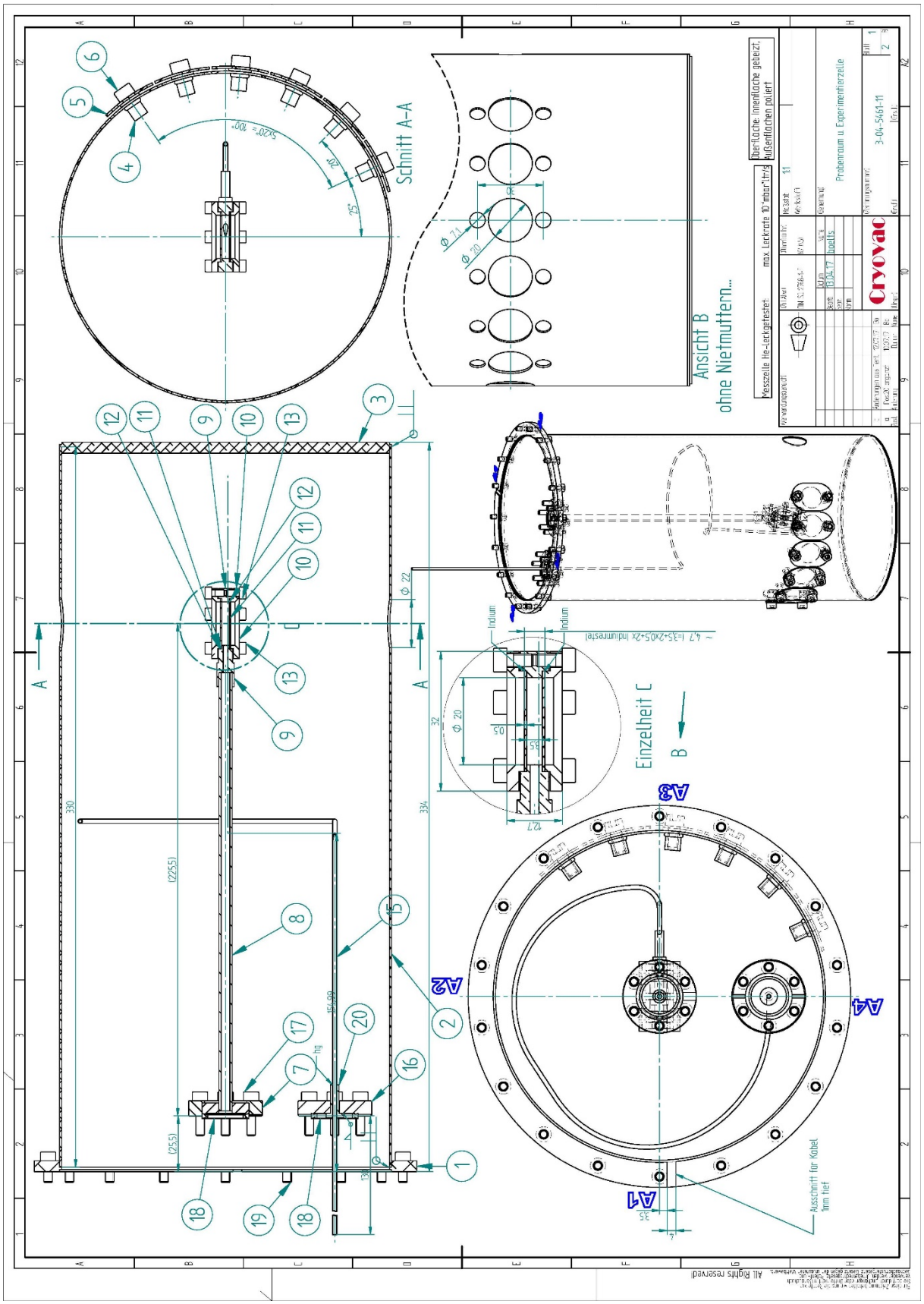
Schnitt A-A
Ansicht B
ohne Nietmuttern...
Einzelheit C
Indium
Ausschnitt für Kabel
Cryovac
Probenraum u. Experimentierzelle
3-04-5461-11